Università degli Studi di Firenze

DIPARTIMENTO DI INGEGNERIA INDUSTRIALE

CICLO XXXIV

Synthesis of silver nanowires and fabrication of substrates for Surface Enhanced Raman Spectroscopy for detection of biomolecules

---

Tesi di Dottorato di Amicucci Chiara

Tutor: Prof. Andrea Caneschi

Co-Tutor: Dr. Paolo Matteini

Contents

Chapter 3: Optimization of large-scale polyol synthesis of AgNWs

Chapter 4: Plasmon resonance of noble metal nanostructures and SERS

Chapter 5: Fabrication of AgNWs-based SERS substrates

Chapter 6: SERS detection of flavonoids in plant extracts

Chapter 7: Development of a wearable SERS chip for detection of lactic acid and urea in sweat

Abstract

Most surface-enhanced Raman spectroscopy (SERS)-active metal nanoparticles, are prone to uncontrollable and random aggregation in solution phase, yielding unstable and unreproducible SERS signals. For this reason, many efforts have been spent in engineering 2D or 3D substrates of assembled nanoparticles, their miniaturization, and improvement in their sensitivity. Compared with other metal nanostructures, AgNWs exhibit great potential in the fabrication of effective SERS substrates, due to a number of characteristics including, among others, their high aspect ratio, high crystallinity and large surface area, which hold the promise of reproducible and intense SERS signals. The above properties make AgNWs a good candidate to produce reliable substrates able to move SERS toward application in several sectors.

During my PhD work I examined the possibility to exploit the potential of AgNWs in the development of effective SERS substrates. This thesis ranges from an optimization of the synthesis of AgNWs to their engineering in the fabrication of an ideal SERS substrate, aimed at promoting this technique for its routine use in real applications.

In the first two Chapters a general introduction of AgNWs is reported including main aspects on morphology and their main applications (Chapter 1) as well as the most relevant synthesis strategies proposed so far (Chapter 2). In Chapter 3 the experimental work I carried out to optimize the synthesis of AgNWs through a polyol method and the definition of a reproducible synthesis protocol is reported. In Chapter 4 the basic principles of SERS are discussed, especially with regard to the plasmonic resonances related to these noble metal nanoparticles. Chapter 5 deals with additional experimental work aimed at the development of effective SERS substrates based on AgNWs by cost-effective, simple and reproducible strategies. Finally in the last Chapters two applications based on SERS involving the use of the SERS substrates previously developed are discussed. In Chapter 6 a multi-spotted AgNWs substrate was used for the drop-on and fast SERS identification of flavonoids in chamomile, which is of interest as valuable alternative to traditional analytical methods. In Chapter 7 the AgNWs substrate was integrated into a skin-wearable SERS chip to monitor for the presence of specific metabolites in sweat Finally, the main results of the work carried out in this PhD thesis are summarized and the prospects for future work based on these results are commented on.

Chapter 1: Silver Nanowires, an overview

1. Introduction

A nanowire is a nanostructure with a diameter of the order of nanometre (10^{-9} metres) and with a length-to-width ratio (aspect ratio, AR) greater than 1000 or more. Alternatively, nanowires can be defined as structures that have a thickness or diameter constrained to tens of nanometres or less and an unconstrained length. As such they are often referred to as one-dimensional (1-D) materials. Many different types of nanowires exist, including superconducting (e.g. YBCO), metallic (e.g. Ni, Pt, Au, Ag), semiconducting (e.g. , InP, GaN) and insulating (e.g. SiO_2,). The topic of this thesis deals with metallic nanowires, and specifically those made of silver (AgNWs). These types of nanowires show peculiar properties that are not seen in bulk materials. This is because electrons in metallic nanowires are confined laterally and thus occupy energy levels that are different from the traditional continuum of energy levels or bands found in bulk materials. Over the last decade AgNWs have been widely studied for their peculiar properties, making them an advanced material for several applications in the life sciences, electronics and energy areas.[1-14] Their interest has rapidly grown in the scientific literature reaching about half a million publications in 2019 (Figure 1).

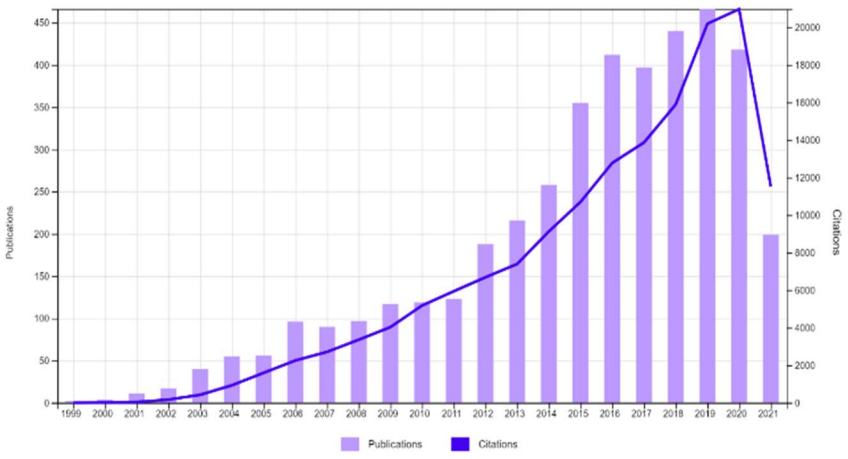

Figure 1. AgNWs publications and citations per years from https://www.webofscience.com/

The potential of AgNWs has been exploited in the fabrication of novel materials useful in catalysis, microelectronic devices, thin film solar cells and biosensors, due to their excellent electrical and thermal conductivity, low surface resistance, high transparency, tunable optical properties and good biocompatibility. In optical applications such as in surface-enhanced Raman spectroscopy (SERS), which represents a main topic of this thesis, the plasmonic behaviour of AgNWs play a fundamental

role. Plasmonic nanoparticles are characterized by a coherent oscillation of conduction electrons as a response to the stress of an external electromagnetic radiation. In Chapter 4 we will go into more detail on plasmonic properties and SERS.

In the following sections, instead, we will provide a brief overview on the main structural features and applications of AgNWs.

2. AgNWs morphology

The traditional definition of AgNWs is based on their characteristic size and shape. Concerning the size, the diameter of a AgNW is usually in a range of 10–200 nm, and the length is typically in a range of 5–100 μm. Typical AR values of AgNW are greater than 10, while analogue nanowires with smaller aspect ratios are defined as silver nanorods. AgNWs exhibit different cross-sectional geometries, depending on whether they are composed of a single crystal or based on a multiply twinned crystal.[15]. In general, they are monocrystalline, i.e. with the same crystal lattice extending over the entire length of the structure, and containing five twin planes running parallel to its long axis. The internal twin structure is a manifestation of the type of seed involved in the growth, as well as of the growth pathway. At very small sizes, there is enough thermal energy for a nucleus to fluctuate among different shapes and crystal structures. [16] The fluctuation will cease once the nucleus has grown to reach a certain size, generating a minuscule structure commonly referred to as a seed. Within a certain size range, twinned structures can be energetically more favourable than the monocrystalline counterpart due to the requirement to minimize the total free energy. As a result, seeds with different numbers of twin planes, including monocrystalline (no twin plane), singly twinned (one twin plane), and multiply twinned (typically, five twin planes), can all be formed in the early stages of a colloidal synthesis of noble metal nanoparticles. The exact populations of these different types of seeds are determined by the experimental conditions, and, in particular, by the initial reaction rate involved in the nucleation step. [17]

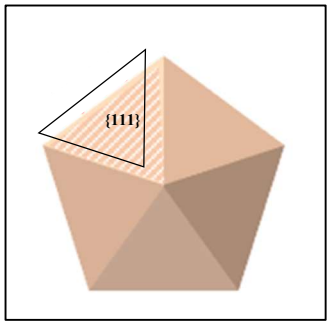

Figure 2. Scheme of decahedral Ag seeds

Pentatwinned AgNWs are supposed to evolve from decahedral seeds whose surface is covered by 10 {111} facets and five twin boundaries (Figure 2). During growth, it is hypothesized that Ag atoms are preferentially deposited onto the twin boundaries, followed by their diffusion to the {111} facets. As a consequence, penta-twinned NWs contain five twin planes running parallel to the long axis, while their side surface is covered by five {100} facets and their ends are capped by a pentagonal

pyramid consisting of five {111} planes and five twin boundaries. [18-25] The mechanism of growth of AgNWs will be discussed in more detail in Chapter 2.

3. AgNWs: applications

3.1 Catalysis

Silver has been widely investigated as a cathode catalyst owing to its stable and high electrocatalytic activity in different applications such as anion exchange membrane fuel cells (AEMFCs), hydroxide exchange membrane flue cells (HEMFCs), in organic compound epoxidation and conversion of CO_2 in CO. Zeng et al. demonstrated that unsupported AgNWs exhibit remarkable electrocatalytic activity toward oxygen reduction reaction in a three-electrode cell. More significantly, the performance of AgNWs as cathode catalyst is comparable to that of state-of-the-art AEMFCs with carbon-supported Ag catalysts, offering a promising alternative to carbon-supported electrocatalysts in fuel cells and metal–air batteries, in view of eliminating carbon supporting materials.[26] Alia and colleagues instead demonstrated that AgNWs with small diameters are the pathway for development of oxygen reduction catalysts for HEMFCs.[27] They also anticipated that the nanowire extended surface could reduce catalyst degradation during sequential cycling, improving durability. Chimentao et al. studied the cesium-promoted catalytic activity of AgNWs in the styrene epoxidation reaction.[28] Finally María de Jesús Gálvez-Vázqueza and colleagues tested a AgNW catalyst for the selective CO_2 reduction in a gas diffusion electrode half-cell setup, enabling high mass transport conditions.[29]

3.2 Microelectronic devices

The excellent electrical conductivity of AgNWs has been mainly exploited in three applications of microelectronics: transparent conductive films, conductive silver adhesives and nano-welding technology.

3.2.1 Transparent conductive films

Transparent conductive films (TCFs) with high conductivity and high transparency are essential for a wide variety of electronic devices. [30-33] Relevant examples of optoelectronic devices used in daily life and that contain TCFs are: light-emitting diodes, solar cells, semiconductors, liquid crystal displays and photodiodes. Indium tin oxide (ITO) [34-37] is mostly used as TCF because of its superior electrical and optical properties. However, ITO displays some drawbacks such as high brittleness and poor adhesion to substrate materials, which fails to meet some fundamental requirements of flexible and bendable electronic devices. AgNWs are considered to be one of the most valuable alternatives to traditional ITO transparent electrode materials in flexible and bendable light-emitting diode (LED) displays due to their excellent electro-optical properties, high mechanical flexibility and easy fabrication. A AgNWs transparent conductive film is typically obtained by random assembly of AgNWs in a network arrangement. [33, 37-44] In 2014, Langley et al. [45] analysed the physical properties and potential integration of a AgNWs network in solar cells by testing different film deposition techniques, indicating that the properties of the network are independent of the fabrication method.

The latter work demonstrated that AgNWs networks currently provide suitable electro-optical properties to be incorporated into solar cells. Further advantages of using AgNWs in TCFs include low deposition temperatures and variable haze of the resulting electrode.

3.2.2 Conductive adhesives

Conductive adhesives have been identified as an alternative of Pb-free leaded solders. However, compared to metal solders, their conductivity is still low. Recently, Chen et al. [46] found that the addition of AgNWs to a conductive adhesive can increase its resistivity. However, using large-size silver powder as the main filling material and adding a certain amount of AgNWs results in an overall improvement in conductivity, by reducing the volume resistivity of the conductive adhesive. In addition, thanks to their 1D morphology, AgNWs can act as fibers reinforcement within a matrix to increase also its mechanical resistance. [47, 48]

3.2.3 Nanowelding technology

The nanowelding technology is employed in nanodevice fabrication. Many scientists performed research aimed at joining nanowires to form nano-function devices, and based on exploiting both heat input of fusion welding and cold welding without heat. [49,50] In 2014, Giusti et al. [51] demonstrated that thermal annealing is an effective method to reduce electrical resistance of transparent electrodes made of randomly oriented AgNWs. The results showed that the optical transmission still maintained high levels (above 85%) while the electrical resistance decreased by several orders of magnitude.

3.3 Solar Cells

Solar Cells (SCs) convert sunlight into electricity *via* the photovoltaic effect. Today, a wide variety of solar cells have been developed, which are divided into first, second, and third generation SCs (Figure 3). [52]

The first-generation SCs, made of crystalline silicon, are considered as traditional solar cells exhibiting considerable efficiencies, and are significantly demanded in the market. However, the high production cost of crystalline silicon materials is limiting their wider use and alternatives are under consideration in large-scale applications. [53] A second generation of solar cells based on other inorganic materials, such as cadmium telluride (CdTe)/cadmium indium gallium diselenide (CIGS), have been developed. However, their practical applications are restricted by the toxicity and scarcity of these materials, along with their high production costs.[54] As an alternative, organic solar cells (OSCs), dye-sensitized solar cells (DSSCs), and perovskite solar cells (PSCs) have been proposed, which are considered as third-generation SCs. Among third generation SCs, OSCs received significant attention due to their flexibility, low cost, and ease of fabrication,[55] which, combined with their high efficiency, are significantly contributing to the commercialization of flexible organic solar cells (FOSCs). In order to fabricate highly flexible, cost-effective, and highly efficient FOSCs, AgNWs provide a highly advantageous option due to their excellent transparency and conductivity, increased light-scattering properties, plasmonic effects, high flexibility, and high transmittance in the near infrared (NIR) region. [56]

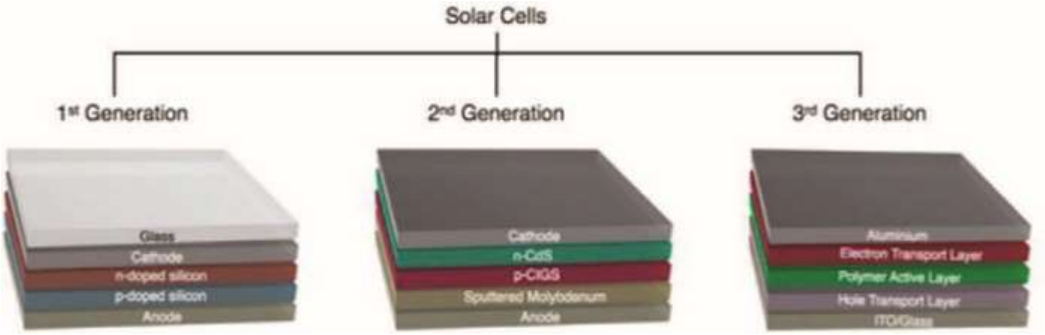

*Figure 3. Classification of the three generations of solar cells.**[52]***

3.4 Biosensors

AgNWs are being proposed for the fabrication of both electrochemical and optoelectronic biosensors in healthcare [57], by taking advantage of their excellent electrical and surface plasmon resonance properties, respectively. [58] Furthermore, they have also been used as sensing material in nonenzymatic electrochemical sensors[59-62] and have been reported some examples of AgNWs enzymatic biosensor applications for glucose[63-65] and cholesterol[66] . Concerning agri-food applications, Coral et al. proposed AgNWs as electron transfer mediators in an electrochemical biosensor, which showed excellent anti-interference characteristics toward the phenol content in wines including vanillin, pyrogallol, quercetin and catechin. These results make AgNWs-based biosensors promising for the sensitive, stable and rapid voltammetric detection of phenols in real applications.[67] Additionally, Zhang et al. developed an innovative system to detect organophosphorus pesticides using an acetylcholinesterase biosensor based on AgNWs.[68]

3.5 Surface-enhanced Raman spectroscopy

SERS applications have spread to many fields, including in the setup of effective optical plasmonic sensors. [69-76] For example, SERS has been successfully exploited in the detection of biological species [77-79], chemical warfare agents, toxic industrial chemicals [80-82], pesticides [83-86], and food additives [87] and in the fields of art preservation [88,89] and forensic science [90,91]. Most SERS-active metal nanoparticles, are prone to uncontrollable and random aggregation in solution phase, yielding unstable and unreproducible SERS signals. For this reason many efforts have been spent in engineering 2D or 3D substrates of assembled nanoparticles, their miniaturization, and improvement in their sensitivity. Compared with other metal nanostructures, AgNWs exhibit great potential in the fabrication of solid SERS substrates, [92] due to a number of characteristics including, among others, their high AR, high crystallinity and large surface area, which hold the promise of reproducible and intense SERS signals. [93] Further advantages of using AgNWs as building block in the preparation of reliable SERS-based substrates include scalability in their fabrication process as well as low costs, large accessibility, eco-compatibility and biocompatibility of the reagents used in their synthesis. The whole properties mentioned make AgNWs a good candidate to produce reliable SERS substrates, able to move SERS toward application in several sectors.[24] In accordance with the above, this thesis is devoted to AgNWs from their synthesis to engineering and fabrication of an ideal SERS substrate, aimed at promoting SERS for its routine use in real-life applications.

Bibliography

[1] White, S. I.; Mutiso, R. M.; Vora, P. M.; Jahnke, D.; Hsu, S.; Kikkawa, J. M.; Li, J.; Fischer, J. E.; Winey, K. I. Electrical Percolation Behavior in Silver Nanowire-Polystyrene Composites: Simulation and Experiment. Adv. Funct. Mater. 2010, 20, 2709−2716.

[2] Alkilany, A. M.; Lohse, S. E.; Murphy, C. J. The Gold Standard: Gold Nanoparticle Libraries to Understand the Nano−Bio Interface. Acc. Chem. Res. 2013, 46, 650−661.

[3] Huang, X.; Neretina, S.; El-Sayed, M. A. Gold Nanorods: From Synthesis and Properties to Biological and Biomedical Applications. Adv. Mater. 2009, 21, 4880−4910.

[4] Ni, W.; Kou, X.; Yang, Z.; Wang, J. Tailoring Longitudinal Surface Plasmon Wavelengths, Scattering and Absorption Cross Sections of Gold Nanorods. ACS Nano 2008, 2, 677−686.

[5] Burgin, J.; Florea, I.; Majimel, J.; Dobri, A.; Ersen, O.; Treguer-́ Delapierre, M. 3D Morphology of Au and Au@Ag Nanobipyramids. Nanoscale 2012, 4, 1299−1303.

[6] Chang, H.-H.; Murphy, C. J. Mini Gold Nanorods with Tunable Plasmonic Peaks beyond 1000 nm. Chem. Mater. 2018, 30, 1427−1435.

[7] Mahmoud, M. A.; El-Sayed, M. A. Different Plasmon Sensing Behavior of Silver and Gold Nanorods. J. Phys. Chem. Lett. 2013, 4, 1541−1545.

[8] Mayer, K. M.; Hafner, J. H. Localized Surface Plasmon Resonance Sensors. Chem. Rev. 2011, 111, 3828−3857.

[9] Mutiso, R. M.; Sherrott, M. C.; Rathmell, A. R.; Wiley, B. J.; Winey, K. I. Integrating Simulations and Experiments to Predict Sheet Resistance and Optical Transmittance in Nanowire Films for Transparent Conductors. ACS Nano 2013, 7, 7654−7663.

[10] Ye, S.; Rathmell, A. R.; Chen, Z.; Stewart, I. E.; Wiley, B. J. Metal Nanowire Networks: The Next Generation of Transparent Conductors. Adv. Mater. 2014, 26, 6670−6687.

[11]Guo, C. F.; Ren, Z. Flexible Transparent Conductors Based on Metal Nanowire Networks. Mater. Today 2015, 18, 143−154.

[12] Mutiso, R. M.; Sherrott, M. C.; Rathmell, A. R.; Wiley, B. J.; Winey, K. I. Integrating Simulations and Experiments to Predict Sheet Resistance and Optical Transmittance in Nanowire Films for Transparent Conductors. ACS Nano 2013, 7, 7654−7663.

[13] Mertens, S.; Moore, C. Continuum Percolation Thresholds in Two Dimensions. Phys. Rev. E 2012, 86, 61109.

[14] Mutiso, R. M.; Sherrott, M. C.; Li, J.; Winey, K. I. Simulations and Generalized Model of the Effect of Filler Size Dispersity on Electrical Percolation in Rod Networks. Phys. Rev. B: Condens. Matter Mater. Phys. 2012, 86, 214306.

[15] H. Hofmeister, Zeitschrift für Kristallographie – Cryst. Mater. 224 (2009) 528– 538.

[16] Wiley, B.; Herricks, T.; Sun, Y.; Xia, Y. Polyol Synthesis of Silver Nanoparticles: Use of Chloride and Oxygen to Promote the Formation of Single-Crystal, Truncated Cubes and Tetrahedrons. Nano Lett. 2004, 4, 1733−1739.

[17] Yang, T.-H.; Gilroy, K. D.; Xia, Y. Reduction Rate as a Quantitative Knob for Achieving Deterministic Synthesis of Colloidal Metal Nanocrystals. Chem. Sci. 2017, 8, 6730−6749.

[18] Ma, Y.; Gao, W.; Shan, H.; Chen, W.; Shang, W.; Tao, P.; Song, C.; Addiego, C.; Deng, T.; Pan, X.; et al. Platinum-Based Nanowires as Active Catalysts toward Oxygen Reduction Reaction: In Situ Observation of Surface-Diffusion-Assisted, Solid-State Oriented Attachment. Adv. Mater. 2017, 29, 1703460.

[19] Liang, H.; Zhao, H.; Rossouw, D.; Wang, W.; Xu, H.; Botton, G. A.; Ma, D. Silver Nanorice Structures: Oriented AttachmentDominated Growth, High Environmental Sensitivity, and Real-Space Visualization of Multipolar Resonances. Chem. Mater. 2012, 24, 2339−2346.
[20] Zhu, C.; Peng, H.-C.; Zeng, J.; Liu, J.; Gu, Z.; Xia, Y. Facile Synthesis of Gold Wavy Nanowires and Investigation of Their Growth Mechanism. J. Am. Chem. Soc. 2012, 134, 20234−20237.
[21] Yu, X.; Wang, D.; Peng, Q.; Li, Y. Pt-M (M = Cu, Co, Ni, Fe) Nanocrystals: From Small Nanoparticles to Wormlike Nanowires by Oriented Attachment. Chem. - Eur. J. 2013, 19, 233−239.
[22] Aabdin, Z.; Lu, J.; Zhu, X.; Anand, U.; Loh, N. D.; Su, H.; Mirsaidov, U. Bonding Pathways of Gold Nanocrystals in Solution. Nano Lett. 2014, 14, 6639−6643.
[23] Wang, Y.; Choi, S.-I.; Zhao, X.; Xie, S.; Peng, H.-C.; Chi, M.; Huang, C. Z.; Xia, Y. Polyol Synthesis of Ultrathin Pd Nanowires via Attachment-Based Growth and Their Enhanced Activity towards Formic Acid Oxidation. Adv. Funct. Mater. 2014, 24, 131−139.
[24] Welch, D. A.; Woehl, T. J.; Park, C.; Faller, R.; Evans, J. E.; Browning, N. D. Understanding the Role of Solvation Forces on the Preferential Attachment of Nanoparticles in Liquid. ACS Nano 2016, 10, 181−187.
[25] Yu, Y.; Cui, F.; Sun, J.; Yang, P. Atomic Structure of Ultrathin Gold Nanowires. Nano Lett. 2016, 16, 3078−3084. (66) Takahata, R.; Yamazoe, S.; Koyasu, K.; Tsukuda, T. Structural Model of Ultrathin Gold Nanorods Based on High-Resolution Transmission Electron Microscopy: Twinned 1D Oligomers of Cuboctahedrons. J. Phys. Chem. C 2017, 121, 10942−10947
[26]L. Zeng, T. S. Zhao* and L. An A high-performance supportless silver nanowire catalyst for anion exchange membrane fuel cells. J. Mater. Chem. A, 2015, 3, 1410
[27] Alia, S. M. (2011). Extended Two Dimensional Nanotube and Nanowire Surfaces as Fuel Cell Catalysts. UC Riverside. ProQuest ID: Alia_ucr_0032D_10686. Merritt ID: ark:/13030/m5sq93bw.
[28]R.J. Chiment ao et al. Styrene epoxidation over cesium promoted silver nanowires catalysts. Journal of Molecular Catalysis A: Chemical 258 (2006) 346–354
[29] Gálvez-Vázquez, M. ; Alinejad, S. ; Hu, Huifang ; Hou, Yuhui ; Moreno-García, Pavel[1] ; Zana, Alessandro [1] CHIMIA International Journal for Chemistry, Volume 73, Number 11, November 2019, pp. 922-927(6)
[30] Qu F, Zhang T, Gu HW, Qiu QQ, Ding FZ, Peng XY, Wang HY. Electrical and optical properties of ZnO: Al films with different hydrogen contents in sputtering gas. Rare Met. 2015;34(3):173.
[31] Wu ZC, Chen ZH, Du X, Logan JM, Sippel J, Nikolou M, Kamaras K, Reynolds JR. Transparent, conductive carbon nanotube films. Science. 2004;305(5688):1273.
[32] Watcharotone S, Dikin DA, Stankovich S, Piner R, Jung I, Dommett GHB, Evmenenko G, Wu SE. Graphene-silica composite thin films as transparent conductors. Nano Lett. 2007;7(7):1888.
[33] Hecht DS, Hu L, Irvin G. Emerging transparent electrodes based on thin films of carbon nanotubes, graphene,
[34] Granqvist CG, Hultaker A. Transparent and conducting ITO films: new developments and applications. Thin Solid Films. 2002;411(1):1.

[35] Harvey SP, Mason TO, Gassenbauer Y, Schafranek R, Klein A. Surface versus bulk electronic/defect structures of transparent conducting oxides: I. Indium oxide and ITO. J Phys D Appl Phys. 2006;39(18):3959.
[36] Ren B, Liu X, Wang M, Xu Y. Preparation and characteristics of indium tin oxide (ITO) thin films at low temperature by r.f. magnetron sputtering. Rare Met. 2006;25(S):137.
[37]Han T-H, Lee Y, Choi M-R, Woo S-H, Bae S-H, Hong BH, Ahn JH, Lee TW. Extremely efficient flexible organic light-emitting diodes with modified graphene anode. Nat Photonics. 2012; 6(2):105.
[38] Wu J, Agrawal M, Becerril HA, Bao Z, Liu Z, Chen Y, Peumans P. Organic light-emitting diodes on solution-processed graphene transparent electrodes. ACS Nano. 2010;4(1):43.
[39] Liu J, Wu G, Li S, Yu M, Yi J, Wu L. Comparative study on chemical stripping of titanium oxide films formed on titanium alloy. Rare Met Mater Eng. 2012;41(8):1331.
[40] Zeng XY, Zhang QK, Yu RM, Lu CZ. A new transparent conductor: silver nanowire film buried at the surface of a transparent polymer. Adv Mater. 2010;22(40):4484.
[41] Yu Z, Zhang Q, Li L, Chen Q, Niu X, Liu J, Pei Q. Highly flexible silver nanowire electrodes for shape-memory polymer light-emitting diodes. Adv Mater. 2011;23(5):664.
[42] Li J, Liang J, Jian X, Hu W, Li J, Pei Q. A flexible and transparent thin film heater based on a silver nanowire/heat-resistant polymer composite. Macromol Mater Eng. 2014;299(11):1403.
[43] Choi HO, Kim DW, Kim SJ, Yang SB, Jung HT. Role of 1D metallic nanowires in polydomain graphene for highly transparent conducting films. Adv Mater. 2014;26(26):4575.
[44] Ye SR, Rathmell AR, Chen ZF, Stewart IE, Wiley BJ. Metal nanowire networks: the next generation of transparent conductors. Adv Mater. 2014;26(39):6670
[45] Y, Huang JY, Wang C, Sun S, Lou J. Cold welding of ultrathin gold nanowires. Nat Nanotechnol. 2010;5(3):218.
[46] Chen CX, Yan LJ, Kong ESW, Zhang YF. Ultrasonic nanowelding of carbon nanotubes to metal electrodes. Nanotechnology. 2006;17(9):2192.
[47] Luo SY, Wang N, Xu WC, Lv Y. Preparation and rheological behaviour of lead free silver conducting paste. Mater Chem Phys. 2008;111(1):20.

[48] Zhang X, Lei Y, Zhang Z, Qiu T. Preparation and conductivity of ultrafine silver conductive paste. Chin J Vac Sci Technol. 2014;34(11):1257.
[49] Lu Y, Huang JY, Wang C, Sun S, Lou J. Cold welding of ultrathin gold nanowires. Nat Nanotechnol. 2010;5(3):218.
[50] Zhao B, Chen C, Yadian B, Liu P, Lu Z, Xu D, Zhang Y. Effects of welding head on the carbon nanotube field emission in ultrasonic nanowelding. Thin Solid Films. 2009;517(6):2012.
[51] Giusti G, Langley DP, Lagrange M, Collins R, Jimenez C, Brechet Y. Thermal annealing effects on silver nanowire networks. Int J Nanotechnol. 2014;11(9–11):785.
[52] Xiang, X.-Z., Gong, W.-Y., Kuang, M.-S., & Wang, L. (2016). Progress in application and preparation of silver nanowires. Rare Metals, 35(4), 289–298.
Chem. Rec. 2019, 19, 661.
[53] C. Battaglia, A. Cuevas, S. De Wolf, High-efficiency crystalline silicon solar cells: status and perspectives. Energy Environ. Sci. 2016, 9, 1552.

[54] I. Repins, M. A. Contreras, B. Egaas, C. DeHart, J. Scharf, C. L. Perkins, B. To, R. Noufi, 19.9%-Efficient ZnO/CdS/CuInGaSe2 Solar Cell with 81.2% Fill Factor. Prog. Photovoltaics 2008, 16, 235.
[55] M. E. Ragoussi, T. Torres, New generation solar cells: concepts, trends and perspectives. Chem. Commun. 2015, 51, 3957.
[56] M. Azani, A. Hassanpour, T. Torres, Benefits, Problems, and Solutions of Silver Nanowire Transparent Conductive Electrodes in Indium Tin Oxide (ITO)-Free Flexible Solar Cells. Adv. Energy Mater. 2020, 2002536.
[57] C. Salvo-Comino, F. Martin-Pedrosa, C. Garcia-Cabezon, M.L. Rodriguez-Mendez, Silver Nanowires as Electron Transfer Mediators in Electrochemical Catechol Biosensors. Sensors 2021, 21, 3, 899
[58] S.Chu, K. Nakkeeran, A.M. Abobaker, S.S. Aphale, S. Sivabalan, P.R. Babu, K. Senthilnathan, A Surface Plasmon Resonance Bio-Sensor Based on Dual Core D-Shaped Photonic Crystal Fibre Embedded With Silver Nanowires for Multisensing. IEEE Sens. J, 2021, 21, 1, 76-84.
[59] Yogeswaran U., Chen S.-M. A Review on the Electrochemical Sensors and Biosensors Composed of Nanowires as Sensing Material. *Sensors.* 2008;**8**:290–313. doi: 10.3390/s8010290.
[60] Cherevko S., Chung C.-H. Gold Nanowire Array Electrode for Non-Enzymatic Voltammetric and Amperometric Glucose Detection. *Sens. Actuators B Chem.* 2009;**142**:216–223.]
[61] Xu L., Hou Y., Zhang M., Cheng T., Li Y.-H., Yao C., Wu Q. Electrochemical Sensor Based on A Silver Nanowires Modified Electrode for the Determination of Cholesterol. *Anal. Methods.* 2015;**7**:5649–5653.
[62] Zhang C., Govindaraju S., Giribabu K., Huh Y.-S., Yun K. AgNWs-PANI Nanocomposite Based Electrochemical Sensor for Detection of 4-Nitrophenol. *Sens. Actuators B Chem.* 2017;**252**:616–623.
[63] Wang L., Gao X., Jin L., Wu Q., Chen Z., Lin X.-F. Amperometric Glucose Biosensor Based on Silver Nanowires and Glucose Oxidase. *Sens. Actuators B Chem.* 2013;**176**:9–14.
[64] Krishnan S.K., Chakaravarthy S., Hernandez-Rangel A., Prokhorov E., Luna-Bárcenas G., Esparza R., Meyyappan M. Chitosan Supported Silver Nanowires as A Platform for Direct Electrochemistry and Highly Sensitive Electrochemical Glucose Biosensing. *RSC Adv.* 2016;**6**:20102–20108.
[65] Yang X., Bai J., Wang Y., Jiang X., He X. Hydrogen Peroxide and Glucose Biosensor Based on Silver Nanowires Synthesized by Polyol Process. *Analyst.* 2012;**137**:4362–4367.
[66] Xu L., Hou Y., Zhang M., Yang X., Jenkins G., Huang W., Yao C., Wu Q. A Novel Electrochemical Biosensor for Detection of Cholesterol. *Russ. J. Electrochem.* 2016;**52**:239–244.
[67] Coral Salvo-Comino, Fernando Martin-Pedrosa, Cristina Garcia-Cabezon, Maria Luz Rodriguez-Mendez Silver Nanowires as Electron Transfer Mediators in Electrochemical Catechol Biosensors Sensors (Basel) 2021 Feb; 21(3): 899.

[68] Jianhua Zhang,a Bo Wang,a Yiru Li,a Wenhao Shu,a Huaying Hua and Lianqiao Yang An acetylcholinesterase biosensor with high stability and sensitivity based on silver nanowire–graphene–TiO2 for the detection of organophosphate pesticides†
RSC Adv., 2019,9, 25248-25256
[69] B. Sharma, R.R. Frontiera, A.-I. Henry, E. Ringe, R.P. Van Duyne, SERS: Materials, applications, and the future. Mater. Today 15, 16–25 (2012).
[70] K.C. Bantz, A.F. Meyer, N.J. Wittenberg, H. Im, O. Kurtulu¸s, S.H. Lee, N.C. Lindquist, O. S-H, C.L. Haynes, Recent progress in SERS biosensing. Phys. Chem. Chem. Phys. 13, 11551 (2011).
[71] R. Petry, M. Schmitt, J. Popp, Raman spectroscopy-a prospective tool in the life sciences. Chem. Phys. Chem. 4, 14–30 (2003).
[72] X.-M. Qian, S.M. Nie, Single-molecule and single-nanoparticle SERS: From fundamental mechanisms to biomedical applications. Chem. Soc. Rev. 37, 912 (2008).
[73] X. Qian, X.-H. Peng, D.O. Ansari, Q. Yin-Goen, G.Z. Chen, D.M. Shin, L. Yang, A.N. Young, M.D. Wang, S. Nie, In vivo tumor targeting and spectroscopic detection with surface-enhanced Raman nanoparticle tags. Nat. Biotechnol. 26, 83–90 (2008).
[74] S. Schlücker, Surface-enhanced Raman spectroscopy: Concepts and chemical applications. Angew. Chem. Int. Ed. 53, 4756–4795 (2014).
[75] F. Romanato, R. Pilot, M. Massari, T. Ongarello, G. Pirruccio, P. Zilio, G. Ruffato, M. Carli, D. Sammito, V. Giorgis, D. Garoli, R. Signorini, P. Schiavuta, R. Bozio, Design, fabrication and characterization of plasmonic gratings for SERS. Microelectron. Eng. 88, 2717–2720 (2011).
[76] I. Ros, T. Placido, V. Amendola, C. Marinzi, N. Manfredi, R. Comparelli, M. Striccoli, A. Agostiano, A. Abbotto, D. Pedron, R. Pilot, R. Bozio, SERS properties of gold Nanorods at resonance with molecular, transverse, and longitudinal plasmon excitations. Plasmonics, 1–13 (2014).
[77] R.A. Tripp, R.A. Dluhy, Y. Zhao, Novel nanostructures for SERS biosensing. Nano Today 3, 31–37 (2008).
[78] S.D. Hudson, G. Chumanov, Bioanalytical applications of SERS (surfaceenhanced Raman spectroscopy). Anal. Bioanal. Chem. 394, 679–686 (2009).
[79] L. Litti, V. Amendola, G. Toffoli, M. Meneghetti, Detection of low-quantity anticancer drugs by surface-enhanced Raman scattering. Anal. Bioanal. Chem. 408, 1–9 (2016).
[80] D.A. Stuart, K.B. Biggs, R.P. Van Duyne, Surface-enhanced Raman spectroscopy of halfmustard agent. Analyst 131, 568 (2006
[81] J.M. Sylvia, J.A. Janni, J.D. Klein, K.M. Spencer, Surface-enhanced Raman detection of 2,4-dinitrotoluene impurity vapor as a marker to locate landmines. Anal. Chem. 72, 5834–5840 (2000).
[82] R.S. Golightly, W.E. Doering, M.J. Natan, Surface-enhanced Raman spectroscopy and homeland security: A perfect match? ACS Nano 3, 2859–2869 (2009).
[83] J. Kubackova, G. Fabriciova, P. Miskovsky, D. Jancura, S. Sanchez-Cortes, Sensitive surfaceenhanced Raman spectroscopy (SERS) detection of organochlorine pesticides by alkyl dithiol-functionalized metal nanoparticles-induced plasmonic hot spots. Anal. Chem. 87, 663–669 (2015).

[84] S. Sánchez-Cortés, C. Domingo, J.V. García-Ramos, J.A. Aznárez, Surface-enhanced vibrational study (SEIR and SERS) of Dithiocarbamate pesticides on gold films. Langmuir 17, 1157–1162 (2001).
[85] D. Lee, S. Lee, G.H. Seong, J. Choo, E.K. Lee, D.-G. Gweon, S. Lee, Quantitative analysis of methyl parathion pesticides in a polydimethylsiloxane microfluidic channel using confocal surface-enhanced Raman spectroscopy. Appl. Spectrosc. 60, 373–377 (2006).
[86] X. Li, G. Chen, L. Yang, Z. Jin, J. Liu, Multifunctional Au-coated TiO2 nanotube arrays as recyclable SERS substrates for multifold organic pollutants detection. Adv. Funct. Mater. 20, 2815–2824 (2010).
[87] J. Zheng, L. He, Surface-enhanced Raman spectroscopy for the chemical analysis of food. Compr. Rev. Food Sci. Food Saf. 13, 317–328 (2014).
[88] K. Chen, M. Leona, T. Vo-Dinh, Surface-enhanced Raman scattering for identification of organic pigments and dyes in works of art and cultural heritage material. Sens. Rev. 27, 109–120 (2007).
[89] F. Casadio, M. Leona, J.R. Lombardi, R.P. Van Duyne, Identification of organic colorants in fibers, paints, and glazes by surface enhanced Raman spectroscopy. Acc. Chem. Res. 43, 782–791 (2010).
[90] Y. Yang, Z.-Y. Li, K. Yamaguchi, M. Tanemura, Z. Huang, D. Jiang, Y. Chen, F. Zhou, M. Nogami, Controlled fabrication of silver nanoneedles array for SERS and their application in rapid detection of narcotics. Nanoscale 4, 2663–2669 (2012).
[91] B. Sägmüller, B. Schwarze, G. Brehm, S. Schneider, Application of SERS spectroscopy to the identification of (3,4-methylenedioxy) amphetamine in forensic samples utilizing matrix stabilized silver halides. Analyst 126, 2066–2071 (2001).
[92] T. Ichimura, N. Hayazawa, M. Hashimoto, Y. Inouye, S. Kawata, Local enhancement of coherent anti-Stokes Raman scattering by isolated gold nanoparticles. J. Raman Spectrosc. 34, 651–654 (2003).
[93] J.R. Lombardi, R.L. Birke, A unified view of surface-enhanced Raman scattering. Acc. Chem. Res. 42, 734–742 (2009).

Chapter 2: Synthesis of AgNWs

1. Introduction

During the past thirty years researchers have proposed many fabrication methods to prepare AgNWs that are mainly derived from the strategy employed to prepare quantum wires. Electrochemical methods were employed in pioneering works, but the AgNWs synthesized in this way were not uniform and obtained in low yields. As an evolution of first trials, hard template and soft template methods have been developed in the past twenty years, their classification being based on the nature of the template. The polyol method is a prominent example of soft template approach, and this strategy has been widely used by most researchers. In this section, we will first briefly introduce the hard template and soft template methods, and then describe the development of the polyol method. In essence, the hard template method is more controllable, but the purification process is time-consuming and complex. In contrast, the purification process in soft processes is very convenient, but the morphology and the monodispersity of the products are difficult to control.

2. Hard template methods

The advantage of hard template methods is that the AgNWs prepared through this approach can be synthesized in a well-controlled manner. Nanoporous membranes [1] and carbon nanotubes [2] are typical examples of hard templates that are used to synthesize AgNWs.

Using a nanoporous membrane as a template, the AgNWs can be grown within the pores of the membrane. AgNWs diameter can be varied by choosing membranes with pores of different sizes. This method was first explored by the Martin's group [1], through the use of porous membranes to prepare conductive polymers, metals, semiconductors and nanostructures with extraordinarily small diameters. Thereafter, porous alumina, nanochannel glasses, mesoporous silica and porous polycarbonate were extensively used to prepare metal nanostructures. By using these hard templates, different metal nanostructures can be generated within the pores by either electrochemical or chemical reduction of their ionic counterpart. The advantage of hard templates is that the as-fabricated AgNWs can be highly ordered and show well-defined morphologies. However, complex procedures are required for the subsequent removal of templates and relevant purification processes may damage nanowires, especially those with high aspect ratios.

Carbon nanotubes provide an ideal host matrix for AgNWs, as was first demonstrated by Ajayan et al. [2] They filled carbon nanotubes with molten lead and thus utilized these materials as templates for the fabrication of nanowires. Subsequently, Ugarte and co-workers [3] developed a new approach to fill carbon nanotubes with $AgNO_3$, which is subsequently converted to metallic silver by irradiation with an electron beam produced by an electron microscope, finally generating AgNWs, according to the reaction: $2AgNO_3 \rightarrow 2Ag + 2\,NO_2 + \,O_2$.

DNA has been recognized as an useful building material in nanotechnologies, due to its ability to participate in supramolecular interactions and its unique structure. Braun et al. [4] were the first to prepare AgNWs by using DNA as a template. A key feature in this protocol is the attractive

interactions between DNA template and silver cations, the latter being subsequently reduced in the presence of the template with a reducing agent [4] or *via* photoreduction [5,6] to yield the desired AgNWs. As is the case of other hard template methods, the subsequent removal of these templates is challenging, and the yield of AgNWs is very low. In general, hard template methods are not scalable, which limits their industrial applicability.

3. Soft template methods

In order to overcome the shortcomings of hard template methods, researchers have focused their efforts on strategies that rely on soft templates, such as various kinds of surfactants, micelles, and different polymers. A key feature of many of these soft templates is that they can dissolve in solution. Since most soft template methods are conducted in solution phase, these strategies may have excellent potential for application in industry. Surfactants were initially chosen as preferred soft templates for the synthesis of AgNWs. For example, cetyltrimethylammonium bromide (CTAB) has been extensively studied in the last decade, and it was first used as capping agent in the synthesis of many inorganic nanorods and nanowires. Nonetheless, this strategy can be employed for the fabrication of AgNWs, as has been demonstrated by Murphy et al. [7] which used rod-shaped micelles of CTAB as templates. Surfactants, micelles or polymers are adsorbed onto the growing metal crystals and kinetically control the growth rate through their adsorption and desorption from the crystal surface. The capping agent along with the nanospherical side-products can be then isolated from the targeted AgNWs by centrifugation. Different polymers that are soluble in solution have also been used as capping agents, serving as soft templates. For example, polyvinyl alcohol [8,9], polyethylene oxide [10], and hydrophilic blockcopolymers [11] have been used as soft templates for the synthesis of AgNWs. However, the products synthesized by these methods are frequently affected by low yields, irregular morphologies, polycrystallinity, and low aspect ratios, which may limit their application on an industrial scale. Among soft template methods, the polyol method is currently considered the most successful and will be discussed in detail in the following sections.

4. Mechanism of AgNWs growth by the polyol method

The characteristic growth mechanism of AgNW formed *via* the polyol method is depicted in Figure 1 and can be summarized as follows. Elemental silver atoms are obtained from the reduction of $AgNO_3$, then, once the concentration of silver atoms has reached a supersaturation value, they start to undergo nucleation of silver seeds and eventually grow into nanoparticles. Both twinned and single-crystal seeds of silver are formed through homogeneous nucleation. The twinned seeds are the most abundant morphology because of their relatively low surface energies [25]. In order to avoid uncontrolled aggregation of twinned seeds (in view of a regular growth of AgNWs), they are typically stabilized according to three strategies. Firstly, the use of polyvinylpyrrolidone (PVP) in the reaction can serve to cap and stabilize seeds by physical adsorption on their surfaces. Secondly, the addition of chloride ions in the form of added halide salt to the reaction mixture can provide electrostatic stabilization for the seeds. Thirdly, a controlled reduction rate can also prevent the seeds from undergoing aggregation. As the seeds are refluxed, larger nanoparticles are formed at the expense of smaller ones *via* a process known as Ostwald ripening [26]. The majority of larger silver particles can be directed (by the capping agent) to grow into nanorods. These nanorods can continuously grow into nanowires by the assistance of PVP. In general, the approach used in the addition of the reagents, i.e.

by a syringe pump or one-pot, can affect AgNWs growth. The one-pot synthesis of AgNWs involves three stages of reaction [27]: initially AgCl nanocubes are formed as heterogeneous nuclei at 100°C, which then evolve into multiply twinned particles, finally leading to the formation of AgNWs. On the other hand, according to the syringe pump approach (Figure 1), initially formed Ag nuclei (composed of few Ag atoms) evolve in multiply twinned particles, then forming AgNWs. In general, regardless of the approach used (one-pot or syringe pump), a deeper understanding of the growth mechanism of AgNWs is still required to truly achieve high control levels over their final shape and, accordingly, of their optical properties.

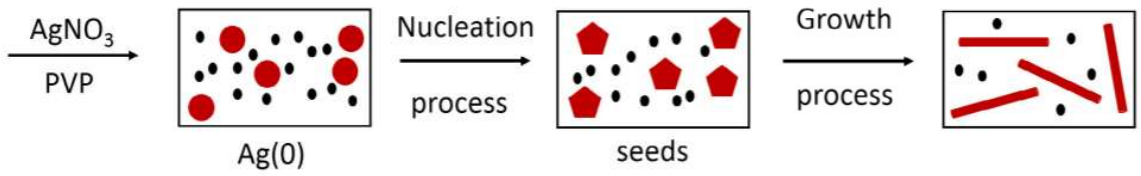

Figure 1 Schematic depiction of the growth mechanism of AgNWs via the polyol method and according to the syringe pump approach

4.1. Nucleation, the role of multi twinned particles

Multiply twinned particles (MTPs) have been shown to represent the initial seeds of nanowires in the polyol method by many researchers. Xia and coworkers demonstrated that MTPs have a decahedral shape prior to the appearance of silver nanorods in the reaction mixture [28]. In particular, the twin boundaries of the MTP outwardly extend in a fivefold symmetry, consisting of ten {111} facets. The twin boundary has the highest energy on the surface of MTPs, which causes silver atoms to be drawn to these boundaries during the Ostwald ripening process. Therefore, the silver atoms selectively undergo crystallization at the twin boundaries, causing the MTP to become elongated along a single axis to yield one-dimensional nanostructures such as nanorods and nanowires. As a consequence, in addition to the {111} facets at their ends as originally present on the MTPs, these elongated one-dimensional structures also bear five {100} facets along their sides. Xia and coworkers [28] also verified that the twin planes cannot become distorted during the growth process, providing a certain degree of confinement of the structure.

4.2. AgNWs growth, the role of PVP

As mentioned in the previous section, nanorods or nanowires that are grown from MTPs bear {111} facets at their ends and {100} facets on their sides. Although the MTPs from which the nanowires would eventually grow bear {111} facets, {100} are then formed during the course of the reaction. In fact results from Xia et al. [28] revealed that the interactions between PVP and the {100} facets are much stronger than those with {111} facets. As a consequence of the selective binding by PVP to the {100} facets, these facets become covered by PVP, thus preventing silver atoms from undergoing nucleation at these sites. Therefore, the remaining sites available for crystal growth are at the {111} facets, in such a way that any additional growth continues from the ends in a one-dimensional geometry. These two factors explain the reason why the twin particles can grow into nanowires under the assistance of PVP. The mechanism of AgNW growth that was proposed by Xia et al. [28] is shown in Figure 2.

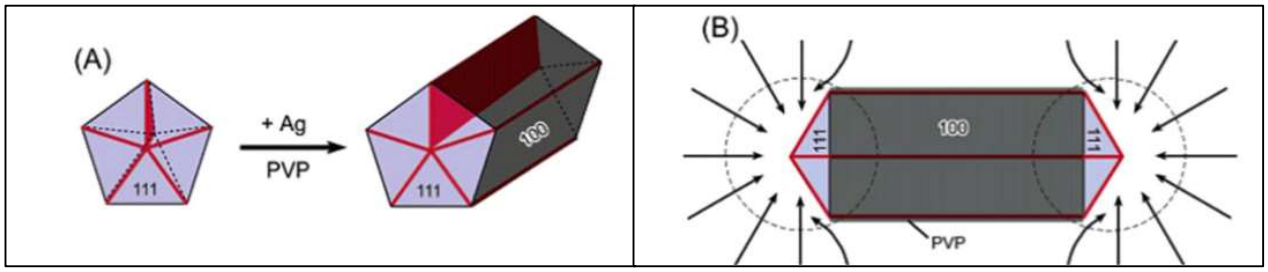

Figure 2. Sketch of the mechanism of AgNWs formation according to Xia et al. [28]

5. Polyol method: synthetic strategies

The polyol method has been the most successful route to produce AgNWs of high quality on a large scale. There are several different synthetic strategies for producing AgNWs by the polyol method but all of them are similar in terms of type of employed reagents. The polyol fulfils a dual role, as both a solvent and reducing agent, while $AgNO_3$ provides the silver ions, The typical polyol AgNWs synthesis starts by heating the reactants mixture leading to the reduction of the metal salt by the polyol. During this reaction PVP is used both as a capping agent and to prevent the aggregation of silver nanoparticles. The Xia's group [12] was the first to apply the polyol process [13] to synthesize AgNWs, employing ethylene glycol as polyol working as reducing agent and solvent [14]. The degree of polymerization of PVP and the molar ratio between the repeat units of PVP and $AgNO_3$ are important factors influencing the synthesis of uniform AgNWs. A disadvantage of this process is that the injection rate of $AgNO_3$ and PVP needs to be very accurately controlled, and thus it may be difficult to carry out it on a large scale. The presence of chloride anions (initially added to the reaction mixture) facilitate AgNWs growth for two reasons: 1) they stabilize silver seed particles by electrostatic interactions; 2) they prevent the accumulation of undesirable and high concentrations of free Ag(I) ions and seeds by forming poorly soluble AgCl salts, thus regulating the reagent concentrations. Although researchers have modified various details of this procedure, two fundamental factors were found to be essential for the production of AgNWs in high yields. First, specific actions must be carried out to prevent the reaction pool from becoming rapidly supersaturated by Ag seeds [15]. Second, other cautions are needed to prevent oxidative etching from occurring on the silver surfaces. In general, by tuning reagent concentrations, temperature and reaction time, it is possible to generate AgNWs of various sizes. In the following we will discuss in detail the factors that influence size, shape and monodispersity of AgNWs .

5.1 Reaction temperature and time

Several researchers have demonstrated that the reducing power increases with temperature, and this effect is due to the temperature-dependent oxidation of ethylene glycol to glycolaldehyde, i.e. the actual reducing agent. Therefore, the temperature of the reaction is a crucial factor influencing the sizes of AgNWs. Traditionally, most polyol reactions performed during the early years of AgNWs synthesis were conducted at 160 °C, and the reaction time was usually 1 h.[12] Too low reaction temperature values do not provide sufficient energy to activate the specific facets required for the anisotropic growth of nanowires, whereas, when the reaction is conducted at too high temperature values the final product mainly consists of very short AgNWs. Based on the principle that the reducing power of ethylene glycol increases with temperature, Wiley et al. [16] conducted a series of

experiments at various temperatures above 160 °C, finding that by performing the reaction at lower temperatures yields longer AgNWs, albeit with larger diameters. Concerning the diameter of AgNWs, several findings on the influence of temperature have leaded to the conclusion that temperature is not the only parameter that influences the diameter of the final product, while multiple factors may be at work in this case.

5.2 PVP/$AgNO_3$ molar ratio

PVP is currently the most convenient polymer available for use as a capping agent in the synthesis of AgNWs. The effectiveness of PVP has been attributed to its nitrogen and oxygen atoms, which can allow this polymer to become adsorbed onto the surfaces of Ag seeds. It plays an important role in determining the morphology of AgNWs that is influenced by both the degree of polymerization and the molar ratio between PVP and $AgNO_3$. For example, the use of PVP molecules with longer chain yields AgNWs with higher aspect ratios. Ye and coworkers [17] conducted a series of control experiments using mixtures of PVP with various chain lengths. The authors found that the use of a mixture of long chain PVP with short PVP molecules provides an efficient strategy for reducing the diameters of AgNWs. On the other hand, tuning the molar ratio of PVP to $AgNO_3$ can influence the morphology of AgNWs in a different way. Just to give an example a work of Coskun el al. is here briefly discussed .[29] In Figure 3, we can see the SEM images of the nanowires synthesized by using PVP/$AgNO_3$ molar ratios of 3:1, 4.5:1, 6:1, 7.5:1, 9:1, and 11:1 (a-f in the Figure, respectively).

When the PVP/$AgNO_3$ molar ratio is 3:1 or 4.5:1, the passivation of {100} faces of multitwinned particles is insufficient and Ag nanostructure growth occurs on both {111} and {100} facets. Under these conditions, AgNWs synthesized at low PVP/$AgNO_3$ molar ratios may show large diameters. Moreover, the multitwin particles that could not grow into nanowires agglomerate and form large amounts of micrometer-sized Ag particles. As the PVP/$AgNO_3$ molar ratio increases, the diameter of the nanowires decreases gradually. On the other hand, on increasing the PVP/$AgNO_3$ molar ratio, the formation of micrometer-sized Ag particles is observed, as shown in Figures 3e-f. This can be attributed to excess PVP molecules covering all surfaces of Ag nanoparticles, including the ones that must be left active. The excess of PVP molecules is also responsible for blocking the anisotropic growth of Ag nanowires. Optimum PVP/$AgNO_3$ molar ratio is then determined as 7.5:1, as inferred from Figure 3d. Under these conditions, only {100} faces of multitwinned particles are passivated, and a longitudinal growth along the [110] direction becomes favourable.

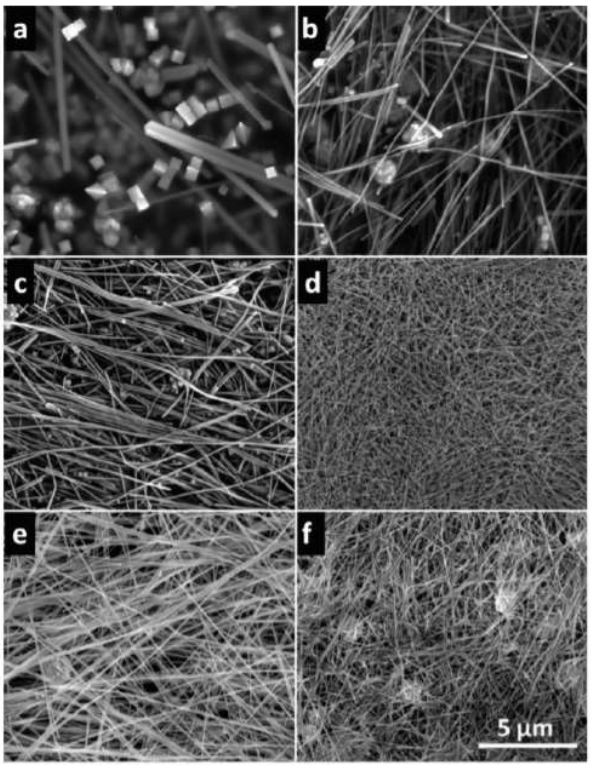

Figure 3. SEM images of AgNWs synthesized at different PVP/$AgNO_3$ molar ratios of (a) 3:1, (b) 4.5:1, (c) 6:1, (d) 7.5:1, (e) 9:1, and (f) 11:1. ***[29]***

The concentration of $AgNO_3$ is another important parameter determining the morphology of AgNWs. Zhan et al. [18] investigated the effect of the concentration of $AgNO_3$ on the morphology of the final AgNWs. Similarly, Huang et al. [19] examined the effect of altering the concentration of $AgNO_3$ on the aspect ratios of the resulting AgNWs. The author kept the amount of PVP constant; thus, when the concentration of $AgNO_3$ was increased, the PVP/$AgNO_3$ ratio decreased. Based on the above considerations, we can see that the concentration of $AgNO_3$ is closely related to the concentration of PVP. Overall, there are two approaches to study the influence of the concentration of $AgNO_3$, one is to keep the amount of PVP constant, while the other is to keep constant the PVP/$AgNO_3$ molar ratio. The former approach has been widely followed, while the latter has received less attention so far.

5.3 Role of chloride ions

The presence of chloride ions is another important factor that can determine the final morphology adopted by silver nanostructures. The absence of chloride ions can lead to irregular particles in the final product, while the presence of trace amounts of chloride anions has a dramatic effect on the morphologies of both nuclei and products. Xia et al. [23,24] were the first to observe this phenomenon, and explained that the chloride ions can coordinate to silver nuclei, thereby stabilizing them against aggregation, facilitating nanoparticle growth. Furthermore, an abundance of chloride ions is useful to reduce the concentration of free silver cations in solution by forming AgCl. Consequently, the chloride anions fulfil a similar role as would otherwise be achieved by the use of a syringe pump for controlled reagent delivery by regulating the amount of free silver cations present during the early stages of Ag seeds formation. The formation of AgCl thus prevents the accumulation of an excess of silver cations and seeds, and ensures a gradual release of silver cations during the subsequent stages of nanostructure growth. Coskun el al. examined different concentration values of chloride in the reaction in an extensive range, using NaCl salt as chloride precursor.[29] SEM images of the Ag structures synthesized via the polyol process with NaCl amounts of 0, 8.5, 12, 17.1, 25.6, and 85.5 μM are shown in Figure 4 (a-f in the Figure, respectively). Figure 4a shows a SEM image of Ag nanoparticles synthesized without the addition of NaCl. The absence of Cl^- ions in the solution results in the formation of only Ag nanoparticles without nanowires. This result may arise from fast reduction of Ag^+ ions to Ag^0 atoms since Ag is only present in ionic form in the reaction. On the other hand, addition of NaCl leads to the presence of Ag as AgCl, slowing down the reduction of Ag^+. These slow reaction conditions enable Ag nanoparticles to grow as multitwin particles, which would then grow in the form of nanowires (as shown in Figures 4c,d). On the other hand, further increase in NaCl amounts triggers the formation of micrometer-sized Ag particles, as shown in Figures 4d,e which is attributed to the saturation of Cl^- in the growth solution. Hence, the reaction rate slows down, leading to the formation of AgCl particles without any nanowires.

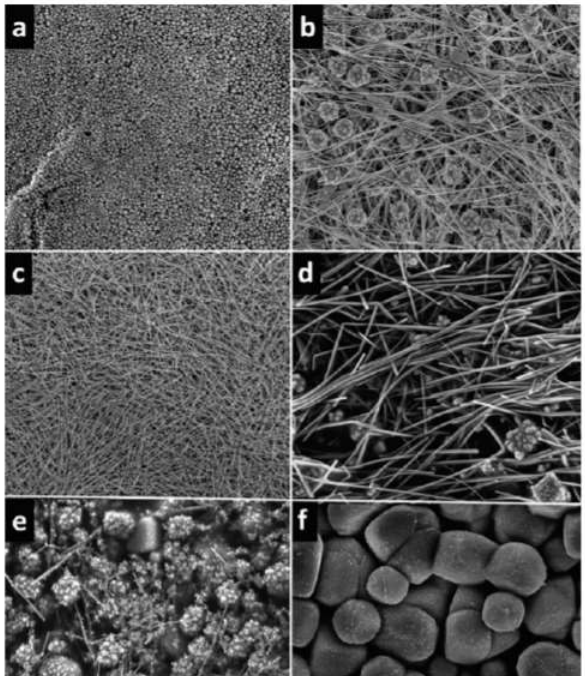

Figure 4 SEM images of the polyol process products produced with different NaCl amounts of (a) 0, (b) 8.5, (c) 12, (d) 17.1, (e) 25.6, and (f) 85.5 μM. ***[29]***

5.4 Reactants flow rate control

The method used in the addition of the reagents is a further important factor that determines the final morphology of the products. According to a one-pot synthesis scheme, the reactants are added and mixed together at room temperature before the reaction reaches an elevated temperature. In this case the addition of chloride ions is necessary, otherwise silver atoms will aggregate, generating amorphous particles as final products. The method is easily scalable, but suffers from a lower morphological control of the final product.

A different possibility is to inject some main reagents of the synthesis during the reaction at a controlled rate (in some cases just $AgNO_3$, in other cases both $AgNO_3$ and PVP). Generally, the addition of these reagents is conducted by a syringe pump once the temperature reached a certain level. The advantage of this method is that the morphology of the final product can be controlled by the speed employed. Nonetheless it is worth mentioning that the use of syringe pump may represent a limit in view of the large-scale production of AgNWs.

6. Conclusions

Part of the work of this thesis (see Chapter 3) was devoted to optimize the polyol synthesis of AgNWs according to the protocol proposed by Xia as mentioned above. We introduced suitable modifications, which were aimed at obtaining a high yield of AgNWs (i.e. a low number of by-products nanoparticles) with high monodispersity.

Bibliography

[1] C.R. Martin, Nanomaterials: A Membrane-Based Synthetic Approach. Science 266 (1994) 1961.

[2] P.M. Ajayan, S. lijima, Capillarity-induced filling of carbon nanotubes Nature 361 (1993) 333–334.

[3] D. Ugarte, A. Châtelain, W.A. de Heer, Nanocapillarity and Chemistry in Carbon Nanotubes. Science 274 (1996) 1897

[4] E. Braun, Y. Eichen, U. Sivan, G. Ben-Yoseph, DNA-templated assembly and electrode attachment of a conducting silver wire. Nature 391 (1998) 775–778

[5] L. Berti, A. Alessandrini, P. Facci, DNA-Templated Photoinduced Silver Deposition.J. Am. Chem. Soc. 127 (2005) 11216–11217.

[6] J. Lu, L. Yang, A. Xie, Y. Shen, DNA-templated photo-induced silver nanowires: Fabrication and use in detection of relative humidity Biophys. Chem. 145 (2009) 91–97.

[7] N.R. Jana, L. Gearheart, C.J. Murphy, Wet chemical synthesis of silver nanorods and nanowires of controllable aspect ratioElectronic supplementary information (ESI) available: UV–VIS spectra of silver nanorods. Chem. Commun. (2001) 617–618.

[8] Y. Zhou, S.H. Yu, C.Y. Wang, X.G. Li, Y.R. Zhu, Z.Y. A novel ultraviolet irradiation photoreduction technique for the preparation of single-crystal Ag nanorods and Ag dendrites. Chen, Adv. Mater. 11 (1999) 850–852.

[9] S. Bhattacharrya, S.K. Saha, D. Chakravorty, Nanowire formation in a polymeric film. Appl. Phys. Lett. 76 (2000) 3896.

[10] J.-J. Zhu, X.-H. Liao, X.-N. Zhao, H.-Y. Preparation of silver nanorods by electrochemical methods. Chen, Mater. Lett. 49 (2001) 91–95.

[11] D. Zhang, L. Qi, J. Ma, H. Cheng, Formation of Silver Nanowires in Aqueous Solutions of a Double-Hydrophilic Block Copolymer. Chem. Mater. 13 (2001) 2753–2755

[12] Y. Sun, B. Gates, B. Mayers, Y. Xia, Crystalline Silver Nanowires by Soft Solution Processing. Nano Lett. 2 (2002) 165–168.

[13] G. Viau, F. Fiévet-Vincent, F. Fiévet, Nucleation and growth of bimetallic CoNi and FeNi monodisperse particles prepared in polyols. Solid State Ionics 84 (1996) 259–270.

[14] L. Gou, M. Chipara, J.M. Zaleski, Nucleation and growth of bimetallic CoNi and FeNi monodisperse particles prepared in polyols. Chem. Mater. 19 (2007) 1755–1760.

[15] B. Wiley, Y. Sun, Y. Xia, Synthesis of Silver Nanostructures with Controlled Shapes and Properties. Acc. Chem. Res. 40 (2007) 1067–1076

[16] S.M. Bergin, Y.-H. Chen, A.R. Rathmell, P. Charbonneau, Z.-Y. Li, B.J. Wiley, The effect of nanowire length and diameter on the properties of transparent, conducting nanowire films. Nanoscale 4 (2012) 1996–2004

[17] Y. Ran, W. He, K. Wang, S. Ji, C. Ye, A one-step route to Ag nanowires with a diameter below 40 nm and an aspect ratio above 1000. Chem. Commun. 50 (2014) 14877–14880.

[18] J. Ma, M. Zhan, Rapid production of silver nanowires based on high concentration of AgNO3 precursor and use of FeCl3 as reaction promoter. RSC Adv. 4 (1071) (2014) 21060–21062.

[19] J.-Y. Lin, Y.-L. Hsueh, J.-J. Huang, J.-R. Wu, Effect of silver nitrate concentration of silver nanowires synthesized using a polyol method and their application as transparent conductive films. Thin Solid Films 584 (2015) 243–247.

[20] B. Wiley, Y. Sun, B. Mayers, Y. Xia, Shape-Controlled Synthesis of Metal Nanostructures: The Case of Silver. Chem. Eur. J. 11 (2005) 454–463

[21] B. Wiley, Y. Sun, J. Chen, H. Cang, Z.-Y. Li, X. Li, Y. Xia, Shape-Controlled Synthesis of Silver and Gold Nanostructures. MRS Bull. 30 (2005) 356–361.

[22] J. Chen, B.J. Wiley, Y. Xia, One-Dimensional Nanostructures of Metals: Large-Scale Synthesis and Some Potential Applications. Langmuir 23 (2007) 4120–4129

[23] B. Wiley, T. Herricks, Y. Sun, Y. Xia, Polyol synthesis of silver nanoparticles: Use of chloride and oxygen to promote the formation of single-crystal, truncated cubes and tetrahedrons. Nano Lett. 4 (2004) 1733–1739.

[24] B. Wiley, Y. Sun, Y. Xia, Polyol Synthesis of Silver Nanostructures: Control of Product Morphology with Fe(II) or Fe(III) Species. Langmuir 21 (2005) 8077–8080

[25] P.M. Ajayan, L.D. Marks, Quasimelting and phases of small particles. Phys. Rev. Lett. 60 (1988) 585–587

[26] A.R. Roosen, W.C. Carter, Simulations of microstructural evolution: anisotropic growth and coarsening. Physica A 261 (1998) 232–247.

[27] H. Ding, Y. Zhang, G. Yang, S. Zhang, L. Yu, P. Zhang, Growth and form of gold nanorods prepared by seed-mediated, surfactant-directed synthesis. RSC Adv. 6 (2016) 8096– 8102.

[28] Y.G. Sun, B. Mayers, T. Herricks, Y.N. Xia, Polyol Synthesis of Uniform Silver Nanowires: A Plausible Growth Mechanism and the Supporting Evidence. Nano Lett. 3 (2003) 955–960

[29] S. Coskun, B. Aksoy, and H. E. Unalan, Polyol Synthesis of Silver Nanowires: An Extensive Parametric Study.Cryst. Growth Des. 2011, 11, 4963–4969

Chapter 3: Optimization of large-scale polyol synthesis of AgNWs

1. Introduction

Silver nanowires are typically prepared by the so-called polyol synthesis in which silver nitrate ($AgNO_3$) is dissolved in ethylene glycol in the presence of polyvinylpyrrolidone (PVP) as stabilizing agent and a chloride (Cl^-) ions.[1–5] This synthetic procedure allows tuning AgNWs thickness and AR and is considered rather simple and cost-effective. The final product, however, is always a mixture of nanowires and nanoparticles of different size and shape. These by-products are detrimental for AgNWs-based applications and the as-prepared AgNWs are therefore usually subjected to several cycles of purification, which increases their cost and production time.[1,6–8] To minimize by-products, it is important to clarify the mechanism of nanowire formation. So far, this task has been extremely challenging, as the nucleation and growth of AgNWs is influenced by a wide range of factors, including reaction temperature and time,[8] injection rate of $AgNO_3$, [4,8] concentration of halide. In this chapter I'll discuss the optimization of a reaction protocol found in literature[9] which has been modified in order to have a controlled large-scale production of AgNWs. The optimization concerned physical parameters of the reaction (reaction temperature and time, injection rate and seeding time) while the stoichiometry wasn't varied. Before going into more detail, it is worth mentioning the importance of two chemical aspects to consider when dealing with AgNWs synthesis and that were previously scarcely taken into account in determining a successful reaction: the purity of silver chloride (AgCl) and the use of anhydrous ethylene glycol (EG), as discussed below.

Our set-up of reaction (Figure 1) consists in a thermostatic bath in which a flask (250mL) containing EG (80mL) is placed. EG is heated until a temperature ≥160°C and, once a stable temperature is reached, AgCl is added to the flask. EG starts to reduce silver and in turn seeds are formed. After few minutes the solutions of $AgNO_3$ and PVP dissolved in EG are injected by using a syringe pump to finely control injection rate (Figure 2). After pouring the reaction into acetone, AgNWs start to precipitate (Figure 3) and, after 12h, the supernatant is removed. Finally, we disperse the precipitate in isopropanol.

As mentioned before, EG can influence the reaction mechanism: it is an organic compound with $(CH_2OH)_2$ formula, it is an odourless, colourless, sweet-tasting, viscous liquid. It is commonly used as solvent thanks to its rather high boiling point (197.3°C), it is soluble in most of the organic solvents and shows a very high affinity with water. In the synthesis of AgNWs it is not only used as a solvent but also acts as a reducing agent. In a typical polyol synthesis, AgNWs are obtained by reducing $AgNO_3$ with EG according to the reactions:

$$CH_2OH\text{-}CH_2OH \leftrightarrows CH_3CHO + H_2O \qquad (1)$$

$$2Ag^+ + 2CH_3CHO \leftrightarrows 2Ag^0 + CH_3COCOCH_3 + 2H^+ \qquad (2)$$

As we can see EG isn't the real reducing agent because at high temperature it is in equilibrium with glycolaldehyde, which reduces Ag^+ generating metallic silver and 2,3 butanedione. Just considering the chemistry of this reaction, three points prove critical and important to take into consideration. The first concerns temperature that should be set at a value ≥160°C to guarantee a full conversion of EG

to glycolaldehyde. The second deals with the presence of water; in fact, according to (1), H_2O water is another product of EG conversion in such a way that its high concentration in the environment moves the equilibrium toward the reagent, in turn decreasing the formation of glycolaldehyde. The third point concerns the last product (2,3 butanedione), which, at the reaction temperature (~160°C) is found in gaseous state. In this case the equilibrium is influenced by conducting the reaction in a close or open system. Specifically, upon removing the gaseous product we succeed in moving the equilibrium toward the product, the latter expedient representing the driving force of the whole reaction. Accordingly, we decided to use anhydrous EG to promote the formation of glycolaldehyde and a light air flux to remove 2,3 butanedione vapours.

As mentioned above, another important aspect is the purity of AgCl, which is used in the first step as silver precursor to form the silver seeds that will grow into wires during the reaction. It consists of a white crystalline solid, it is well known for its low solubility in water and light sensitivity. Upon illumination or heating, silver chloride converts to Ag^0 (and chlorine), which is signalled by grey to a black or purplish coloration of the reaction solution. Therefore, it is crucial to take into consideration the photosensitivity of this compound: for this reason, all operations should be done without exposing the compound to light. Anyway, even with all the necessary precautions, the reagent can be considered altered after a short period of storage. To overcome this limit, it is recommended to use freshly prepared AgCl.

Figure 1 Reaction set-up for large scale polyol method synthesis of AgNWs

Figure 2 AgNWs reaction mix before purification

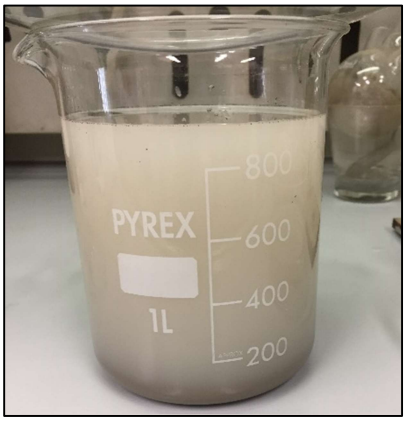

Figure 3 Purification of AgNWs with acetone

2. Optimization of the reaction

In order to design a profitable optimization of AgNW synthesis, a number of steps were considered:

1. SELECTION OF THE INITIAL PARAMETERS AND RESPONSE
2. SELECTION OF THE EXPERIMENTAL DOMAIN
3. SCREENING EXPERIMENTS
4. DISCARD UNIMPORTANT FACTORS
5. SELECTION OF THE STRATEGY
    a. SEQUENTIAL DESIGN (sequential univariate experiment)
    b. SIMULTANEOUS DESIGN (simultaneous multivariate combined experiment)

The selection of the initial factors was done in accordance with the literature and the reaction mechanism. In this step it is important to consider all the variables that can influence the product quality. At the same time, it is also important to assess the quality of the product by a measurable output. For what concerns the synthesis, the parameters considered were: temperature, seeding time, rate of reagent injection and reaction time after injection. As measurable response, the UV-visible extinction of the isopropanol suspension was selected.

The experimental domain consists of the range of values within which each factor can be varied. In our case temperature (T) was varied from 160°C to 185°C; seeding time (ST) from 3 min to 10 min; injection rate (IR) from 0.1 mL/min to 2 mL/min and reaction time after injection (RT) from 0 to 60 min.

After that, 8 screening experiments (SEs) were identified as specified below:

Table 1 Parameters of screening experiments

	T	**ST**	**IR**	**RT**
SE1	**160°C**	5 min	1 mL/min	30 min
SE2	**185°C**	5 min	1 mL/min	30 min
SE3	160°C	**3 min**	1 mL/min	30 min
SE4	160°C	**10 min**	1 mL/min	30 min
SE5	160°C	5 min	**0.1 mL/min**	30 min
SE6	160°C	5 min	**2 mL/min**	30 min
SE7	160°C	5 min	1 mL/min	**0 min**
SE8	160°C	5 min	1 mL/min	**60 min**

The results showed that by varying the temperature, different length distributions of AgNWs and optical profiles are obtained, and by varying the injection rate, AgNWs length keeps constant while their optical properties change. On the other hand, by increasing the reaction time after the injection, we didn't observe any change in the quality of the product: as a consequence, we discarded the last factor, which was set at 0 min, and examined the variation produced by the others in the experimental

domain. Provided that the remaining factors are just three and assuming that they are independent, we choose to perform a further set of experiments according to a sequential design. That is, for each factor, four values were selected and, for each experiment (E), we varied 1 parameter at time keeping constant the remaining others as done in the screening experiments.

Table 2 Parameters of the second set of experiments parameters

	T	ST	IR
E1 (SE1)	**160°C**	5 min	1 mL/min
E2	**170°C**	5 min	1 mL/min
E3	**180°C**	5 min	1 mL/min
E4 (SE2)	**185°C**	5 min	1 mL/min
E5 (SE3)	160°C	**3 min**	1 mL/min
E6	160°C	**8 min**	1 mL/min
E7 (SE4)	160°C	**10 min**	1 mL/min
E8 (SE5)	160°C	5 min	**0.1 mL/min**
E9	160°C	5 min	**0.5 mL/min**
E10 (SE6)	160°C	5 min	**2 mL/min**

The results of these experiments are summarized in the section below.

3. Results and discussion

UV-visible spectroscopy was used to analyse the synthesized AgNWs in accordance with the different experiments, in order to gain information on their shape. Figure 4 shows a typical UV-vis spectrum of the AgNWs in ethanol solution as found in literature.[10] The spectrum exhibits a band centered at 388 nm with a shoulder at 354 nm. Both of these features can be ascribed to main plasmonic modes of AgNWs with a pentagonal cross-section, basically in accordance with simulated data by Kottmann et al.[11]

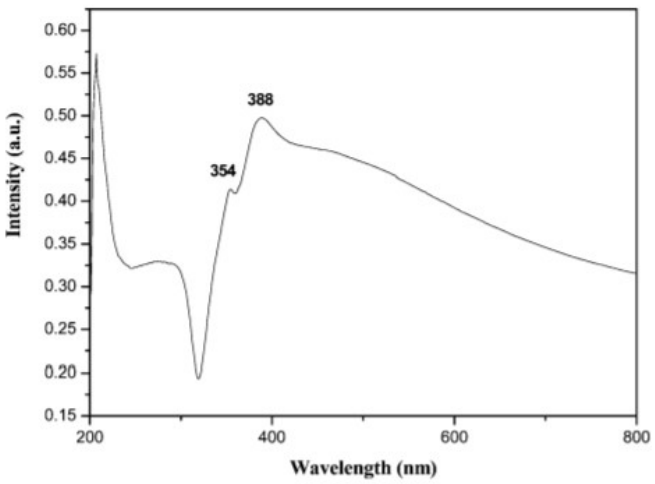

*Figure 4. Exemplary UV-vis extinction spectrum of AgNWs.**[10]***

Apart from UV-vis analysis, SEM images were collected to characterize the morphology of the obtained products and finally the best combination of experimental parameters was determined.

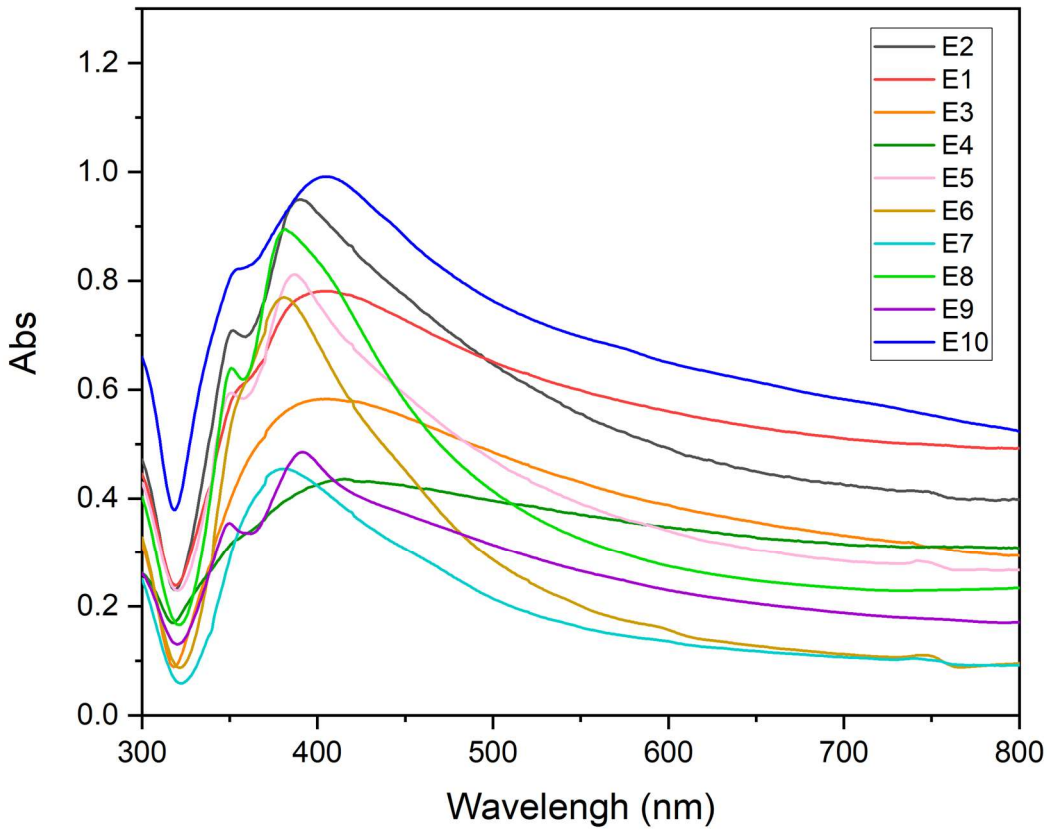

Figure 5. UV-Vis spectra of the experiments E1-10. (E1: temp 160°C, seeding time 5 min, injection rate 1 mL/min; E2: temp 170°C, seeding time 5 min, injection rate 1 mL/min; E3: temp 180°C, seeding time 5 min, injection rate 1 mL/min; E4: temp 185°C, seeding time 5 min, injection rate 1 mL/min; E5: temp 160°C, seeding time 3 min, injection rate 1 mL/min; E6: temp 160°C, seeding time 8 min, injection rate 1 mL/min; E7: temp 160°C, seeding time 10 min, injection rate 1 mL/min; E8: temp 160°C, seeding time 5 min, injection rate 0.1 mL/min; E9: temp 160°C, seeding time 3 min, injection rate 0.5 mL/min; E10: temp 160°C, seeding time 3 min, injection rate 2 mL/min.

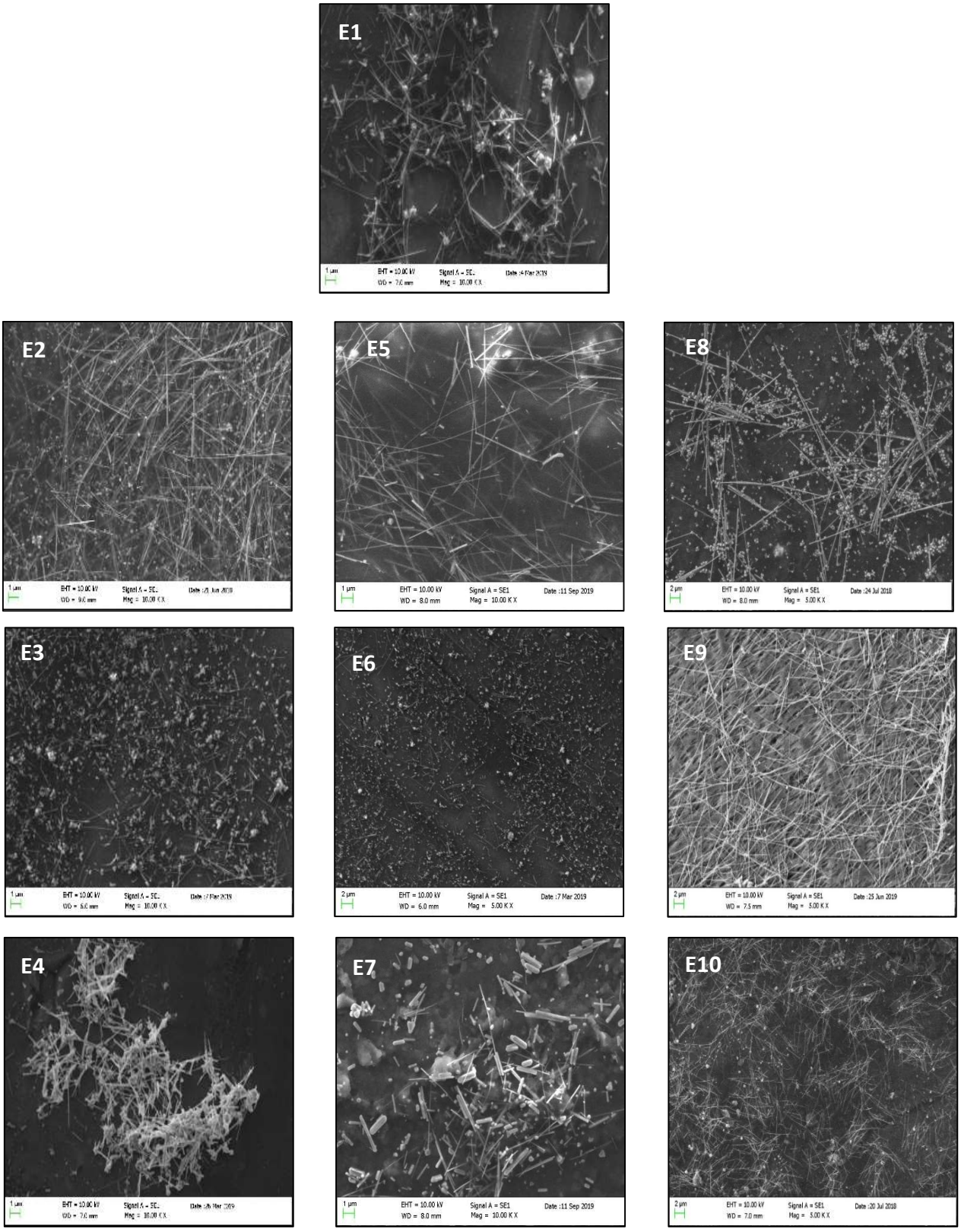

Figure 6. SEM analysis of the experiments E1-10. (E1: temp 160°C, seeding time 5 min, injection rate 1 mL/min; E2: temp 170°C, seeding time 5 min, injection rate 1 mL/min; E3: temp 180°C, seeding time 5 min, injection rate 1 mL/min; E4: temp 185°C, seeding time 5 min, injection rate 1 mL/min; E5: temp 160°C, seeding time 3 min, injection rate 1 mL/min; E6: temp 160°C, seeding time 8 min, injection rate 1 mL/min; E7: temp 160°C, seeding time 10 min, injection rate 1 mL/min; E8: temp 160°C, seeding time 5 min, injection rate 0.1 mL/min; E9: temp 160°C, seeding time 3 min, injection rate 0.5 mL/min; E10: temp 160°C, seeding time 3 min, injection rate 2 mL/min.)

OPTIMIZED REACTION

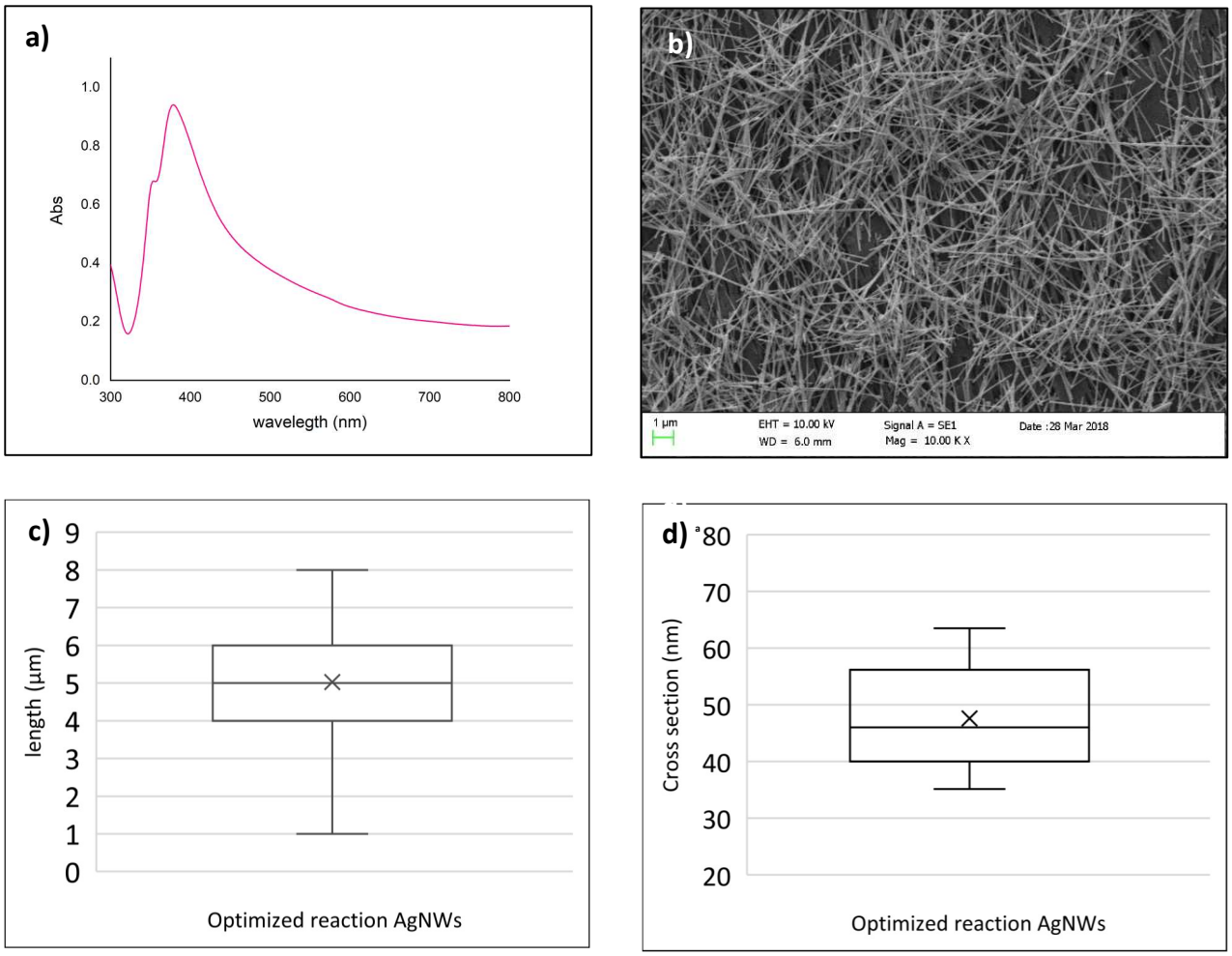

Figure 7. a) UV-Vis spectrum of the optimized synthesis according to the optimal parameters identified in experiments E1-10; b) SEM image of AgNWs synthesized according to the optimized synthesis; c) diagram of length distribution; d) diagram of cross section diameter distribution. Lengths and diameters evaluations were derived from SEM images (as the one reported in panel (b)) by considering a total of n=100 nanowires.

On the basis of optical and morphological data reported above, the following optimal conditions for the reaction were identified: temperature 170°C, seeding time 3 min; rate of injection 0.5 mL/min (reaction time after injection 0 min). Specifically, the optimal conditions were selected according to the presence of the characteristic plasmonic modes of AgNWs within the UV-vis spectrum, and of a a reduced amount of by-products along with a high AgNWs monodispersity as derived from SEM analysis and also confirmed by the absence of substantial absorbance contributions in the red-near infrared region of the UV-vis spectrum. Finally, we carried out the synthesis at the optimal conditions above identified and characterized the product by UV-vis and SEM analyses (Figure 7). The optimized protocol provides uniform AgNWs with 5±1 µm length and 48±10 nm diameter.

4. Experimental section

4.1 Materials

EG anhydrous (Carlo Erba); PVP, (MW 4000; Sigma-Aldrich); $AgNO_3$, AgCl (Cabro S.p.A); isopropanol and ethanol (IPA 99,5%, EA ≥99,8%; Sigma-Aldrich).

4.2 Optimized Synthesis

Briefly, 80 mL of EG was heated and thermally stabilized at 170 °C in a flask. Once the temperature has stabilized, 112.5 mg of AgCl was added to the flask. Meanwhile, 495 mg of $AgNO_3$ and 3 g of PVP were dissolved in 10 mL of EG each. The PVP and $AgNO_3$ solutions were poured into two 10 mL syringes, which were placed in a syringe pump. Three minutes after the addition of AgCl, the slow injection of the two reagents was started with an injection rate of 0.5 mL/min. The reaction proceeded until the injection was finished. Afterward, the flask was cooled in an ice bath. The suspension was poured in 600 mL of acetone to leave AgNWs to spontaneously settle down overnight. Supernatant was removed and AgNWs were re-dispersed in isopropyl alcohol.

4.3 Characterization

AgNWs were characterized by SEM (Zeiss, EVO MA 10, Jena, Germany) and UV-Vis spectroscopy (PerkinElmer Lambda 35 UV/Vis, Norwalk, CT). UV-visible extinction spectra were taken at room temperature on using a quartz cuvette with a 1-cm optical path. All the solutions were 30-fold diluted with isopropylic alcohol before spectra collection. The concentration of the as-obtained AgNWs suspension was finally determined as 1 mg/L by gravimetric determination.

Bibliography

[1] Zhang, P.; Wyman, I.; Hu, J.; Lin, S.; Zhong, Z.; Tu, Y.; Huang, Z.; Wei, Y. Silver Nanowires: Synthesis Technologies, Growth Mechanism and Multifunctional Applications. Mater. Sci. Eng., B 2017, 223, 1−23.

[2] Korte, K. E.; Skrabalak, S. E.; Xia, Y. Rapid Synthesis of Silver Nanowires through a CuCl- or CuCl2-Mediated Polyol Process. J. Mater. Chem. 2008, 18 (4), 437−441.

[3] Liu, Y.; Chen, Y.; Shi, R.; Cao, L.; Wang, Z.; Sun, T.; Lin, J.; Liu, J.; Huang, W. High-Yield and Rapid Synthesis of Ultrathin Silver Nanowires for Low-Haze Transparent Conductors. RSC Adv. 2017, 7 (9), 4891−4895.

[4] Da Silva, R. R.; Yang, M.; Choi, S. Il; Chi, M.; Luo, M.; Zhang, C.; Li, Z. Y.; Camargo, P. H. C.; Ribeiro, S. J. L.; Xia, Y. Facile Synthesis of Sub-20 Nm Silver Nanowires through a BromideMediated Polyol Method. ACS Nano 2016, 10 (8), 7892−7900.

[5] Gebeyehu, M. B.; Chala, T. F.; Chang, S. Y.; Wu, C. M.; Lee, J. Y. Synthesis and Highly Effective Purification of Silver Nanowires to Enhance Transmittance at Low Sheet Resistance with Simple Polyol and Scalable Selective Precipitation Method. RSC Adv. 2017, 7 (26), 16139−16148.

[6] Mayousse, C.; Celle, C.; Moreau, E.; Mainguet, J. F.; Carella, A.; Simonato, J. P. Improvements in Purification of Silver Nanowires by Decantation and Fabrication of Flexible Transparent Electrodes. Application to Capacitive Touch Sensors. Nanotechnology 2013, 24 (21), 215501.

[7] Li, B.; Ye, S.; Stewart, I. E.; Alvarez, S.; Wiley, B. J. Synthesis and Purification of Silver Nanowires to Make Conducting Films with a Transmittance of 99%. Nano Lett. 2015, 15 (10), 6722−6726.

[8] Coskun, S.; Aksoy, B.; Unalan, H. E. Polyol Synthesis of Silver Nanowires: An Extensive Parametric Study. Cryst. Growth Des. 2011, 11 (11), 4963−4969.

[9] L. Hu, H.S. Kim, J.Y. Lee, P. Peumans, Y. Cui, Scalable Coating and Properties of Transparent, Flexible, Silver Nanowire Electrodes. ACS Nano, 2010, 25, 2955.

[10] Y. Gao et al. Evidence for the Monolayer Assembly of Poly(vinylpyrrolidone) on the Surfaces of Silver Nanowires. J. Phys Chem B, (108) 2004 12877

[11] Kottmann, J. P.; Martin, O. J. F.; Smith, D. R.; Schultz, S. Plasmon resonances of silver nanowires with a nonregular cross section. Phys. ReV. B 2001, 64, 235402.

Chapter 4: Plasmon resonance of noble metal nanostructures and SERS

1. Introduction

Noble metals like gold, silver copper and aluminium have peculiar optical properties related to the presence of free conduction electrons. Free electrons move in a background of approximatively fixed positive ions. This free-electron motion generates a plasma called free-electron plasma or simply plasmon.[1] The optical properties of metals are strongly characterized by the optical response of the free-electron plasma, especially in the visible region of the spectrum. An electron oscillation induces a polarization that macroscopically can be described by the dielectric function, considered as the response of the material to an incident electromagnetic (EM) field. A general model for the optical response of free-electron plasma requires considering the correlation between the electrons and the periodic structure of the ions, the presence of impurities or, the phonons, that are collective ions vibrations in lattice described through a quantum mechanical approach.

In this context, the Drude model is a simply way to describe the dielectric function $e(\omega)$ of metal under the perturbation of an external electromagnetic (EM) field with frequency ω. It assumes that the microscopic behaviour of electrons in a solid may be treated classically and behaves much like a pinball machine, with a sea of constantly jittering electrons bouncing and re-bouncing off heavier and relatively immobile positive ions. The interaction between the EM field and the electronic state is then described as a classic damped harmonic oscillator, in which the dissipation coefficient γ takes into account the interaction of the electronic cloud with the field.

The dielectric function $\varepsilon(\omega)$ is related to the plasma frequency ω_p by the following equation (1):

$$\varepsilon(\omega) = \varepsilon_\infty \left(1 - \frac{\omega_p^2}{\omega^2 + i\gamma\omega}\right) \qquad \lambda_p = 2\pi c/\omega_p \qquad (1)$$

In which ε_∞ is the background dielectric function (considered as a constant, $\varepsilon_\infty \geq 1$), λ_p is the wavelength corresponding to ω_p, and c is the light speed constant.

The expression (1) can be split in real and imaginary parts:

$$Re(\varepsilon(\omega)) = \varepsilon_\infty \left(1 - \frac{\omega_p^2}{\omega^2 + \gamma^2}\right) \qquad (2)$$

$$Im(\varepsilon(\omega)) = \left(\frac{\varepsilon_\infty \omega_p^2 \gamma}{\omega(\omega^2 + \gamma^2)}\right) \qquad (3)$$

The two relations can be described as the polarizability and the energy dissipation terms, respectively. Considering that γ is small in comparison with ω, the plasma frequency under the Drude model, can be obtained from the condition $Re\left(\varepsilon(\omega_p)\right) \approx 0$. Therefore, for wavelengths longer than λ_p, that mean $\omega < \omega_p$, we have $Re\left(\varepsilon(\omega_p)\right) < 0$. At the same time, the absorption, characterized by

$Im\left(\varepsilon(\omega_p)\right)$ is also small in this region if ω is not too small. Together these two conditions $Re\left(\varepsilon(\omega_p)\right) < 0$ and small $Im\left(\varepsilon(\omega_p)\right)$, make possible the plasmon resonances.

2. Plasmon resonance

To understand how the real and imaginary parts of the dielectric function predicted by the Drude model are correlated to the plasmon resonance, we can consider the problem of a small metallic sphere interacting with an electromagnetic field. If the radius *a* of the sphere is much smaller than the incident wavelength λ (i.e. a/ λ < 0.1, condition verified for particle of nanometric size and incident light in the visible range), the magnitude of the electric field appears static around the nanoparticles [2,3] and the problem can be solved within the Maxwell's equation using a quasi-static approximation, considering the sphere immerse in a medium of relative dielectric constant ε_M.

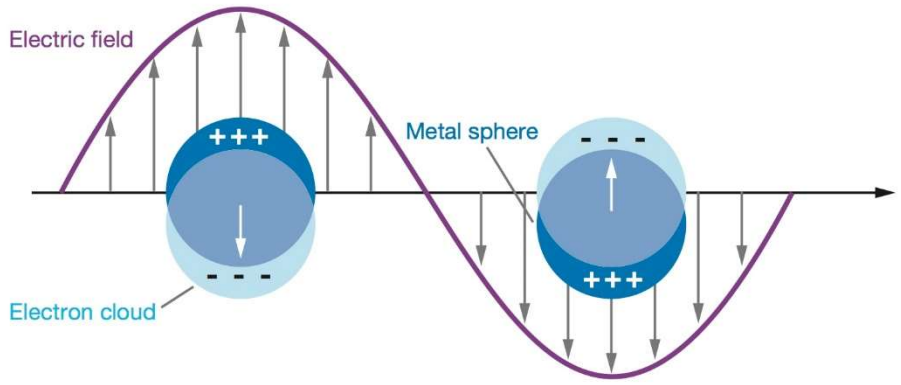

Figure 1: Schematic diagrams illustrating a localized surface plasmon

The electric field E_{In} inside the sphere can then written as a function of the incident field E_0 through the relation: [4]

$$E_{In} = \frac{3\varepsilon_M}{\varepsilon(\omega)+2\varepsilon_M} E_0 \qquad (4)$$

The condition in which the denominator is close to zero ($\varepsilon(\omega) \approx -2\varepsilon_M$) for metals coincide to have small absorption ($Im(\varepsilon(\omega)) \approx 0$ *and* $Re(\varepsilon(\omega)) \approx -2\varepsilon_M$). For the wavelengths that meet these conditions the optical response (the absorption and the scattering) is then very large and the frequency is called resonance frequency. For these frequencies, also, takes place the local surface plasmon resonance (LSPR) responsible of SERS effect. Then, the LSPR can be rigorously defined as a coherent oscillation of the surface conduction electrons excited by electromagnetic radiation that are established when the frequency of light photons matches the natural frequency of surface electrons

oscillating against the restoring force of positive nuclei (Figure 1). The optical response of metal spherical nanoparticles can be calculated theoretically through the Mie theory. [5,6]

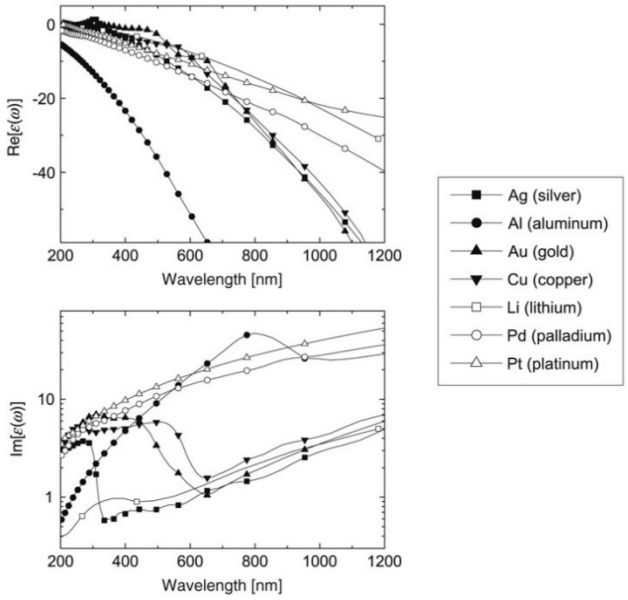

*Figure 2: Overview of the optical properties of a selection of metals in the (extended) visible range. The real (top) and imaginary (bottom) parts of ε are plotted against wavelength (from **Ref 7**)*

A simply way for measuring the LSPR energy is considering the extinction spectrum, that is, the composition of the absorbed and elastic light scattered by the particle, and that can be calculated with the following relation: [5-7]

$$E(\lambda) = \frac{24\pi^2 N a^3 \varepsilon_M^{3/2}}{\lambda \ln(10)} \left[\frac{Re(\varepsilon(\lambda))}{\left(Re(\varepsilon(\lambda)) + \kappa\varepsilon_M\right)^2 + (Im(\varepsilon(\lambda)))^2} \right] \qquad (5)$$

Here, the particle of radius a is represented as a number N of finite polarizable elements, characterized by a dielectric function $\varepsilon(\lambda) = Re(\varepsilon(\lambda)) + i\, Im(\varepsilon(\lambda))$ and immersed in a medium of dielectric function ε_M. The geometrical factor κ takes in account the different possible geometries. It takes a value of 2 for spherical particles, but can increase for particles with higher aspect ratio.[8]

Therefore, a similar effect to the LSPR for spherical particles exist for other geometries but with different denominators for relations (4) and (5) and as consequence, different resonance conditions:

optical resonance for small metallic particles are strongly linked to the geometry and not only an intrinsic property of materials.

Resuming, the good conditions to obtain plasmonic effect by a metal nanostructure are $Re(\varepsilon)$ negative ($-20 \leq Re(\varepsilon) \leq -1$) and small $Im(\varepsilon)$ in the range of wavelength of interest (typically the visible and near infrared). These conditions are satisfied by several metals in the visible region (see Figure 2). Some practical considerations can be added to the theoretical ones, taking into account the availability, the ease of fabrication and manipulation, the toxicity, etc., of the materials used.

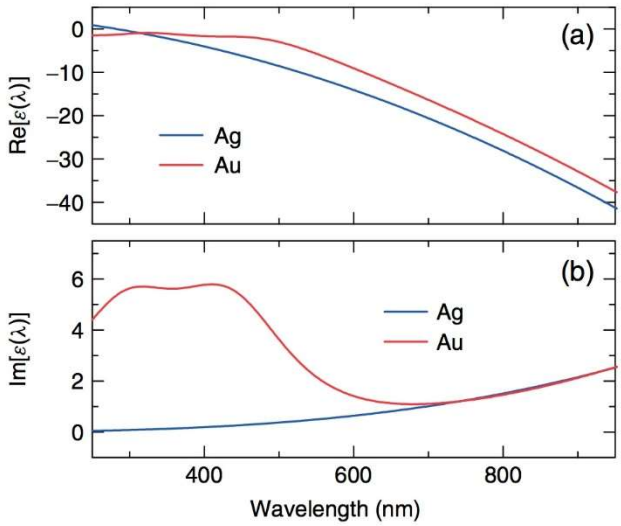

*Figure 3: The real (a) and the imaginary (b) part of the dielectric function ε(λ) for gold and silver in the visible range, from 300 to 900 nm (reported by ref. **[9]**).*

Under this point of view, gold and silver represent the best solutions and they are the most useful metals for SERS applications. Both Au and Ag, in fact, have a very similar electronic density, since the real parts of their dielectric functions are not too far from each other in the visible range (Figure 3). The imaginary part of the dielectric function of Au, instead, feels the additional contribute from the electronic transitions in its electronic band structure in addiction to that from the free electrons. This contribution gives rise to a higher absorption of gold with respect to the silver for $\lambda \leq 600$ nm. The "double hump" structure visible in the imaginary part in figure 3b, peaked at 400 nm comes from the so-called inter-band electronic transitions.[10]

In Figure 3, also is possible to note that for $\lambda \geq 600$ nm, the imaginary part of $\varepsilon(\lambda)$ for both Ag and Au become completely comparable.

3. Local Field Enhancement

Metal nanoparticles can enhance the local electromagnetic field by orders of magnitude. For spherical nanoparticles the superposition of the induced dipole and the external field give rise to a larger local field in characteristic points on the surface called *hotspots* that are found along the diameters and are oriented in the direction of the external field. If the incident wavelength satisfies the resonance

condition, a molecule in the hotspot will experience an intensity boosted by a local field intensity enhancement factor (LFIEF). The order of magnitude of the LFIEF is related to the size and shape of the nanostructure that influence the plasma oscillation properties. For a spherical nanostructure, increasing the size the LSPR position will shift to a higher resonance wavelength (the so-called *redshift*); at the same time, an increased size will cause a stronger damping that result as an increased radiation losses, a broadening of the resonance, associated therefore to a decrease of the LFIEF. [10] Another effect of the increase of the size is a shift from the condition of small size limit in which the quasi-static approximation is valid (the condition $a/\lambda < 0.1$ mentioned earlier) and the appearance of "new" resonance related to the activation of multipolar (or higher order) resonances that usually couple the light with less efficiency with respect to the dipolar ones, but that can be important in some cases. [10-17]

As the size, also the shape of the nanostructures can influence the plasmon resonance. Unlike what happens for high symmetric shapes as spheres or cylinders, the break of the symmetry can provide more than one resonance and a complicated distribution of the enhanced fields. Finally, resonances depend not only on the shape but also on the orientation with respect to the field, highlighting the dependence of the LFIEF on the polarization direction.

4. Surface Enhanced Raman Scattering

Raman spectroscopy and electromagnetic and chemical enhancement effects represent the main ingredients for a description of the fundamentals of the surface-enhanced Raman scattering effect.

The Raman effect (standard or surface-enhanced) is a two-photon scattering process in which the interaction between the light and matter provides information on the vibrational transitions. When an incident light is scattered by a molecule, most photons are diffused with the same energy of the incident ones (elastic scattering). However, a small fraction of light (approximately 1 in 10^7 photons) is scattered at energies different from, and usually lower than, the incident light energy. The energy shift between incident and scattered light, reported in frequency, is typically called as *Raman shift* and provide information on the vibrational properties of matter, allowing for the identification of unknown species using visible light, non invasively and using small amounts of sample. Unfortunately, Raman spectroscopy has limitations related to very low probability of inelastic scattering (Raman cross-section) with respect other optical effect (such as absorption or fluorescence), giving rise to low detectable signals.

Surface-enhanced Raman scattering represents a way to solve the problem of weak Raman signals, exploiting the optical properties of noble metal nanoparticles. It exploits the high localized field enhancement typical of the metal nanostructures under the resonant condition, for enhancing the Raman signal scattered by the molecules adsorbed or in proximity of the metal structures. The gain of intensity obtained thanks to the SERS with respect to the standard Raman signal is typically called Enhancement Factor (EF).

As for standard Raman spectroscopy, where the re-radiated intensity is proportional to the laser power density incident on the sample and to the Raman cross-section of the molecule, in SERS the intensity of a given vibrational mode of the sample is proportional to laser incident light and the normal Raman cross-section, increased by the enhancement factor. This EF should be quantified practically, under appropriate conditions, as the ratio between the signal in presence of SERS enhancement and the light scattered intensities acquired under non-SERS condition for the same sample (eq. 6).

$EF \approx I_{SERS}/I_{Raman}$ (6)

The origin of the EF in literature is associated to two main multiplicative terms that contribute in a different way to the total value [13-24]. The smallest is the chemical enhancement factor. It is responsible of one or two order of magnitude of enhancement and is related to charge-transfer mechanisms between the analyte and the metal. [25-34] The chemical enhancement is not object of this thesis, then we will focus the attention mainly on the Electromagnetic enhancement (EM). It is the major contribute to the EF and is estimated between 8 and 10 order of magnitude. [22-25,34-37] The EM enhancement is related to the coupling between the incident field and the Raman scattered field with the localized surface plasmon resonance of the SERS substrate. The electromagnetic contribution of the SERS can be separated in two gain factors, one for the incident radiation (e.g. enhance of the local excitation field) and one for the re-emitted Raman radiation (e.g. amplification of the scattering). Being correlated to the high localized field enhancement from the LSPR, both these factors decrease drastically increasing the distance from the surface, so the best results are obtained for molecules in close proximity (within ≈ 20 nm) or directly adsorbed on the surface. [35,38-47]

The SERS process is related to the Raman emission by an analyte adsorbed on the nanostructures and the realization of the resonant conditions for the metal nanostructure. These issues strongly characterize the list of parameters that can influence the SERS EF. Best enhancement performances will be obtained, then, with an accurate selection of:

- the excitation source, especially for wavelength and incident polarization direction;
- the detection configuration, pay attention to the scattering geometry and to the polarized or un-polarized detection;
- the SERS-active substrates, in particular for geometry (size and shape) and the resulting optical properties (LSPR), with respect to the incident beam direction and polarization;
- the properties of the analytes, considering their Raman polarizability and intrinsic Raman cross-section. Equally attention needs the concentration of the analyte and how it links to the SERS substrate (surface coverage, distance and orientation).

Since many of these aspects can affect the enhancement (or, sometimes, are unknown), usually the EF is calculated, where it's possible, comparing the SERS intensities with the signals obtained in the identical configuration but in a SERS inactive condition, as reported early in eq 6.

5. The $|E|^4$ approximation to SERS Enhancement Factor

As mentioned earlier, the electromagnetic enhancement factor is the main contribution to the final SERS signal intensity. It can be described using the simply model composed by the molecules of analyte, Raman actives, located in proximity (or adsorbed) to noble metal nanostructures. The incoming laser beam, characterized by an electric field $E_0(\omega_L)$ and a frequency ω_L tuned to the plasmon resonance frequency, will excite the plasmons of the nanostructures, giving rise in the *hot spot* region to a local field $E_{loc}(\omega_L)$ enhanced of a factor $\Gamma_{exc}(\omega_L)\ E_0$:

$$E_{loc}(\omega_L) = \Gamma_{exc}(\omega_L)\ E_0 \quad (7)$$

The increased local field will act as a higher incident laser power and will excite the emission of Raman radiation $E_{Raman}(\omega_R)$ by the analyte. But these molecules are place in proximity of the hot spots, so also the Raman emission will be amplified of a factor $\Gamma_{rad}(\omega_R)$. Then, the final SERS emission should be written as:

$$E_{SERS}(\omega_R) = \Gamma_{rad}(\omega_R)\, E_{Raman} \qquad (8)$$

Hence, the Raman process benefits from both excitation and emission enhancement that leads to a total EF of the form:

$$EF = \Gamma^2_{exc}(\omega_L) \times \Gamma^2_{rad}(\omega_R) \qquad (9)$$

Deducing both the gain terms of relation, the Enhancement Factor EF of eq (6) can be considered as the ratio between the intensities of the SERS and the normal Raman signals:

$$EF \sim \frac{I_{SERS}}{I_{Raman}} = \left|\frac{E_{loc}(\omega_L)}{E_0(\omega_L)}\right|^2 \left|\frac{E_{SERS}(\omega_R)}{E_{Raman}(\omega_R)}\right|^2 \sim \left|\frac{E_{loc}(\omega_L)}{E_0(\omega_L)}\right|^4 \qquad (10)$$

where we consider the approximation $\Gamma(\omega_L) \approx \Gamma(\omega_R)$, since $(\omega_L) \approx (\omega_R)$, valid in the typical Raman measurements since the frequency differences between the incident and the re-emitted light are small.

The relation is the simplest way to describe the SERS EF and is usually known as $|E|^4$ approximation. Moreover, this approach includes a series of implicit approximations related to ignoring: 1) the influence of the local field polarization with respect to the incoming and the scattered fields, 2) eventually frequency dependence of the excitation or remission amplification factor, 3) the Raman contribution, that mediate the emission process. All these issues are usually known as “aspects behind the $|E|^4$ model”, and are subject of discussion in the literature [9, 11-17].

Bibliography

[1] P.M. Platzman and P.A. Wolf. *Waves and interactions in solid state plasmas* (Solid State Physics, Suppl. No 13) Accademic Press, New York, London (1973)

[2] G. C. Schatz Matthew A. Young and R. P. Van Duyne. Electromagnetic Mechanism of Surface-enhanced Spectroscopy Topics in Applied Physics, vol 103. Springer, Berlin, He Topics in Applied Physics, vol 103. Springer, Berlin, Heidelberg idelberg (2006)

[3] K. L. Kelly, E. Coronado, L. Zhao, G. C. Schatz. The optical properties of metal nanoparticles: The influence of size, shape, and dielectric environment. J. Phys. Chem. B 107: 668-77(2003)

[4] G. Mie, Ann. Phys. 25, 377-445 (1908)

[5] C.F. Bohren, D.R. Huffman, Absorption and Scattering of Light by Small Particles. Wiley. New York (1983)

[6] E.D. Palik, editor. Handbook of optical constants of solids III. Academic Press, New York, (1998)

[7] K.A. Willets, R.P. Van Duyne Annu. Rev. Phys. Chem. 58, 267-297 (2007)

[8] S. Link, M.A. El-Sayed, J. Phys. Chem. B 103, 8410–8426 (1999)

[9] G. Laurent, N. Felidj, J. Aubard et al. Phys Rev. B 71, 045430 (2005)

[10] P.G. Etchegoin and E. Le Ru, Basic Electromagnetic Theory of SERS in Surface Enhanced Raman Spectroscopy: Analytical, Biophysical and Life Science Applications. Edited by S. Schlucker Wiley, Weinheim (2011)

[11] H. Wei, A. Reyes-Coronado, P. Nordlander et al. ACS Nano 4, n 5, 2649-2654 (2010)

[12] L.A. Blanco, F. Garcia de Abaco J. Phys Rev. B 69, 205414 (2004)

[13] E.C. Le Ru, E. Blackie, M. Meyer, P.G. Etchegoin J. Phys. Chem. C 111, 13794 (2007)

[14] E.C. Le Ru et al. Current Applied Physics 8, 467-470 (2008)

[15] J. Grand, M.L. de La Chapelle, J.L. Beijeon, et al. Phys. Rev. B 72, 033407 (2005)

[16] L. Billot, M.L. de La Chapelle, A.S. Grimault, et al. Chem. Phys. Lett. 422, 303-307 (2006)

[17] J. Aizpurua, G.W. Bryant, L.J. Richter et al. Phys. Rev. B 71, 23, 235420 (2005)

[18] N. Guillot, M.L. De La Chapelle Nanoantenna Wiley Encyclopedia of Electrical and Electronics Engineering, 1–13 (2012)

[19] N. Guillot, Optical properties of metal nanoparticles and application to surface enhanced nanosensors, Thesis for the degree of Doctor in Science, University of Paris XIII (2012)

[20] A. Wokaun, J. P. Gordon, and P. F. Liao, Phys. Rev. Lett. 48, 957 (1982)

[21] P. Alonso-González, P. Albella, M. Schnell, et al. Nature Communication 3, 684 (2012)

[22] E.C. Le Ru, E.C. Etchegoin Chem. Phys. Lett. 423, 63-66 (2006)

[23] S.J. Lee, Z. Guan, H. Xu, M. Moskovits, J. Phys. Chem. C 11, 17985 (2007)

[24] W.E. Smith, Chem. Soc. Rev. 37, 955-964 (2008)

[25] M. Moskovits, *Rev. Modern Phys.* 57: 783–826 (1985)

[26] A. Otto. *Surface-enhanced Raman scattering: 'classical' and 'chemical' origins* in M. Cardona and G. Guntherodt, editors, Light Scattering in Solids IV, 4 of Top. Appl. Phys., Springer-Verlag, Berlin, (1984)

[27] A. Campion and P. Kambhampati, *Chem. Soc. Rev.* 27, 241–250 (1998)

[28] J. R. Lombardi, R. L. Birke, T. Lu, J. Xu. *J. Chem. Phys.* 84, 4174–4180 (1986)

[29] A. Otto, *J. Raman Spectrosc.* 22, 743 (1991)

[30] B.N.J. Persson, K. Zhao, Z. Zhang *Phys. Rev. Lett.* 96, 207401 (2006)

[31] S.M. Morton, E. Ewusi-Annan, L. Jensen *Phys. Chem. Chem. Phys.* 11, 7424 (2009)

[32] M. Sardo et al., *Phys. Chem. Chem. Phys.* 11, 7437 (2009)

[33] L. Yang, X. Jiang, W. Ruan, et al. *J. Phys. Chem. C* 113, 16226–16231 (2009)
[34] A. Wokaun *Solid State Phys.* 38, 223 (1984)
[35] S. Nie, S. R. Emory, *Science* 275*,* 1102 (1997)
[36] J. Kneipp, H. Kneipp, K. Kneipp *Chem. Soc. Rev*. 37, 1052–1060 (2008)
[37] K. Kneipp, Y. Wang, H. Kneipp, et al. *Phys. Rev. Lett.* 78, 1667 (1997)

[38] M. Kall, H. Xu, P. Johansson *J. Raman Spectrosc.* 36, 510-514 (2005)
[39] M. Moskovits *J. Chem. Phys.* 69, 4159 (1978)
[40] K. Kneipp, H. Kneipp, I. Itzkan et al. *Chem. Phys* 247, 155-162 (1999)
[41] V.M. Shalaev *Phys. Rep* 272, 61 (1996)
[42] M. Stockman, V.M. Shalaev, M. Moskovits et al. *Phys. Rev. B* 46, 2821 (1992)
[43] K. Kneipp, H. Kneipp, E.B. Hanlon et al. *Appl. Spectrosc*. 52, 1493 (1998)
[44] N.J. Halas, S. Lal, W.S. Chang et al. *Chem. Rev.* 111, 3913-3961 (2011)
[45] S. Gresillon, L. Aigouy, A.C. Boccara et al. *Phys. Rev. Lett.* 82, 4520 (1999)
[46] C.E. Talley, J.B. Jackson, C. Oubre et al. *Nano Lett.* 5, 1569 (2005)
[47] D. Ward, N.J. Halas, J.W. Ciszek et al. *Nano Lett.* 8, 919 (2008)

Chapter 5: Fabrication of AgNWs-based SERS substrates

1. Introduction

Plasmonic substrates for SERS require abiding by a number of key needs in order to find effective application in basic research. These primarily include enough sensitivity and high reproducibility, which nowadays have been mostly implemented in a large variety of SERS substrates as a result of the recent great advances in nanofabrication techniques.[1-3] However additional aspects shall be considered when dealing with daily life applications. These include low production costs, fabrication methods suitable for high volume manufacturing, reduced training times and skills needed for their routine usage, integration potential with portable Raman systems for on-site applications, simple reusage or disposable characteristics and quick processing of a variety of samples.[4-7]

The above considerations hold particular significance when life science and healthcare applications of SERS are concerned,[8,9] whose primary conditions are high-throughput, multisample and inexpensive analyses at reduced costs.[10,11] According to this picture, in the last decade a great deal of efforts has been exerted in the development of functional SERS substrates obtained by simple, low cost, rapid and scalable fabrication methods, such as micropipetting, screen- and ink-jet printing, and filtration of colloidal solutions of plasmonic nanoparticles.[12-16]

Concerning biomolecule detection, previous tests at the laboratory level have been mainly based on adding a biomolecule solution to a dispersion of noble metal colloidal nanoparticles. By adding aggregating agents or imparting the particle with suitable surface charge, the formation of interparticle gaps enclosing adsorbed molecules is induced.[17,18] Upon excitation with appropriate light, the Raman signal of an adsorbed species in the gaps is amplified to such an extent to provide characteristic fingerprint information. In this case, the formation of particle clusters with highly divergent size causes scarce reproducibility with large signal variability,[19-22] which remains a main obstacle of this approach. Alternative strategies have been recently aimed at obtaining more consistent and dependable SERS responses from biomolecules. Relevant examples are the SERS detection of proteins adsorbed at specific sites on the surface of nanocrystals showing highly localized electromagnetic fields[23] or by gathering molecules in spatial proximity to SERS hotspots generated at the junctions among optically-aggregated plasmonic nanoparticles.[24] Despite significant advancements, the above efforts remain of limited applicability in light of a forthcoming sustainable production and commercial exploitation. Nowadays, growing expectations are being set towards more reliable SERS substrates specifically created for practical detection of molecules of biomedical significance to be used close to or at the point-of-need settings.[25,26] Nonetheless, their effective realization remains largely underexplored.

In this chapter I'll discuss two works published during the PhD and dealing with the fabrication of two different SERS substrates based on a AgNWs network on a solid support. The two substrates (AgNWs@PTFE and AgNWs@G-paper) were fabricated using different techniques, supporting materials and AgNWs. However, the final result satisfies the criteria to have a SERS-active layer of

self-assembled AgNWs, which are randomly distributed creating a network with a considerable number of intersections, working as effective SERS hotspots.

The AgNWs@PTFE substrate was obtained filtering a AgNWs suspension through a microporous politetrafluoroetilene (PTFE) membrane (0.45 μm pore size) followed by laser patterning. This study was performed during the first year of thesis activity as a parallel activity to synthesis optimization. Here the presence of by-products, which are commonly found in a non-optimized synthesis, represented a negligible problem because during AgNWs filtration, the smallest nanoparticles (smaller than the pore size of the PTFE membrane) pass through the membrane, in such a way that almost only AgNWs are deposited on the substrate. We may note that in the optimized synthesis the minimization of by-products in the final AgNWs batch has been successfully addressed (see Chapter 3 for details), which overcomes the necessity of a post-fabrication filtration. Accordingly, in the second substrate (AgNWs@G-paper) the preparation of 2D plasmonic substrates was performed by spraying AgNWs, which were fabricated by the optimized fabrication protocol.

2. AgNWs@PTFE SERS substrate

We demonstrate the possibility to take advantage of rapid, inexpensive fabrication techniques to produce disposable SERS substrates that can be integrated with a simple spot-on analysis specifically adapted for reliable detection and characterization of molecules of biomedical interest. Precisely, by combining the self-assembly of filtered AgNWs and control over their cluster density with the laser ablation removal of predetermined areas from the SERS-active layer, ordered and spatially confined plasmonic spots accommodating a high concentration of molecules are obtained. This novel design approach, which integrates the strengths of bottom-up and top-down strategies, promotes synergic effects conferring efficiency to the system in such a way to overcome the capabilities of existing label-free SERS methods for biomolecule detection.

2.1 Results and Discussion

A primary obstacle toward setting up a SERS assay for biomolecule detection is represented by their low Raman cross-section, which is less than 10^{-30} cm^2 per molecule.[27] This value is well below that of a standard SERS probe such as rhodamine 6G, in both resonant (10^{-25} cm^2) and nonresonant (10^{-27} cm^2) conditions.[28] Moreover, biomolecules in their own biological environments are found in highly diluted (micromolar and below) concentration.[29] Thus, in order to capture enough SERS signal from the biomolecule content of a biological sample, increasing the local molecular density at SERS-sensitive sites[30,31] or using structures with sharp nanoscaled protrusions or tips featuring intense E-fields[32,33] are amongst the most convenient approaches. Here, we tried to capitalize on both these aspects aimed at assuring as well the fundamental prerequisites of SERS substrates for widespread use. AgNWs, thanks to their large surface area and possibility to easily manipulate and arrange them in 2D or 3D assemblies, adequately meet all the above requirements.[6,34,35]

We employed a revised polyol process to produce ~1.5 μm-long, 80 nm-thick PVP-capped AgNWs. These particles show characteristics LSPR bands at 349 nm and 380 nm.[36] The AgNWs were assembled on commercial filter membranes *via* a simple flow-through method (as described in Chapter 3), which appears as a convenient tool for rapid realization of SERS-active substrates by

using low-cost equipment available in a standard laboratory setting. Our choice of membrane type was aimed at favouring the molecule-metal surface interaction in order to capture the signal from the highest number of biomolecules in the sample. Thus, a disposable hydrophobic PTFE filter membrane (25 mm diameter × 80 µm thickness, 0.45 µm pore size) was selected to serve this purpose: it shows a water contact angle ≥ 90° that optimally satisfy the requirements shown by a hydrophobic surface to driving molecules toward sensitive areas overcoming the diffusion limit.[37,38] Upon passing the colloidal AgNWs solution through the membrane, a 12.5 mm-wide deposition of wires intertwined on the top of the PTFE surface is formed (Figure 1, step 1). In an attempt to optimize the SERS signal we varied the number of AgNWs loaded on the surface of the membrane by subsequent dilutions of the particle dispersion. Tests of the response at different density of the AgNWs on the PTFE surface were carried out on myoglobin (Mb, M_w = 16.7 kDa), a 3.5 nm in size common cardiac protein biomarker frequently taken as model biomolecule in Raman studies.[39] We were able to detect intense SERS signals from 5 µL single drops of a 1×10^{-6} M aqueous solution of Mb deposited on the surface of the substrate and left dry (Figure 2a).

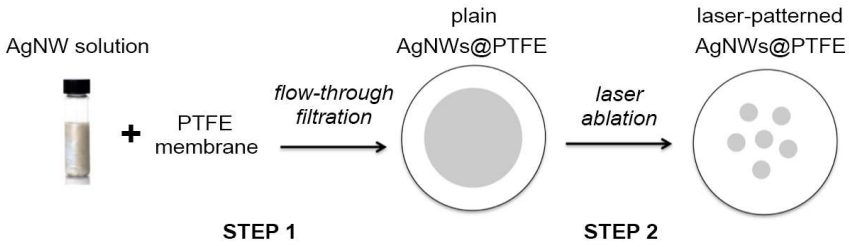

Figure 1. Scheme of the bottom-up/top-down fabrication process for preparing the SERS substrates. Initially an alcoholic solution of AgNWs is filtered through a PTFE filter membrane (STEP 1). Afterwards, laser ablation is used for patterning the substrate (STEP 2).

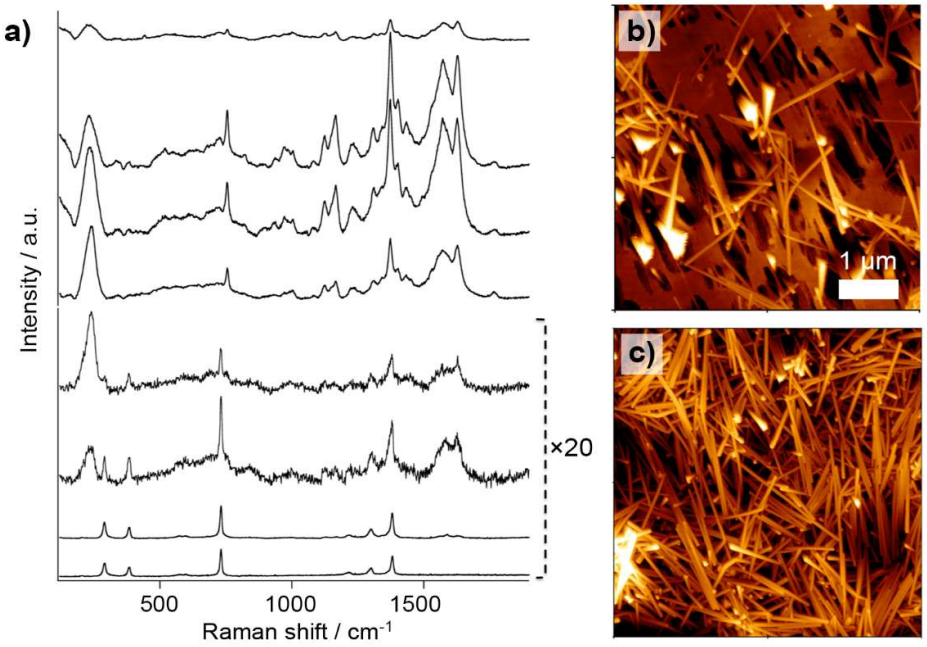

Figure 2. (a) SERS spectra (λ_{ex} = 532 nm) of Mb (1×10^{-6} M) on AgNWs@PTFE substrates at different surface density values of AgNWs: from top to bottom, 0.4, 0.2, 0.1, 0.04, 0.02, 0.01, 0.004, 0 (pure PTFE) µg/mm^2. At low AgNW density values (≤0.02 µg/mm^2) PTFE peaks at 734 cm^{-1} and 1382 cm^{-1} appear close to Mb peaks at 755 cm^{-1} and 1372 cm^{-1}. AFM images of AgNWs@PTFE substrates at 0.1 µg/mm^2 (b) and 0.4 µg/mm^2 (c) AgNW density.

An abrupt increase of protein signals was observed by halving twice the initial AgNW surface density, *i.e.* 0.4 μg/mm^2, down to final 0.1 μg/mm^2. Conversely, after further dilution of deposited AgNWs, the protein signals progressively lose intensity before completely disappearing at values below 0.01 μg/mm^2, where PTFE signals start prevailing. On increasing the number of nanowires, increased SERS intensity values are expected due to a larger number of hotspots in the focal volume mainly originated from wire extremities and contact points.[40] The above statement holds true from 0.004 μg/mm^2 until the optimal 0.1 μg/mm^2 of AgNWs, the latter corresponding to isolated or randomly clustered nanowires over the membrane (Figure 2b) with an estimated particle density of about 25×10^6 AgNWs/mm^2.

Beyond this optimal value, the SERS signal intensity decreases, reaching minimal values at 0.4 μg/mm^2. In the case of a high surface density of wires, two main causes influence the drop in Raman signal. First, a 3D arrangement of nanowires becomes apparent (Figure 2c) and the substrate experiences a change in its wettability abandoning the typical hydrophobic behaviour of PTFE. As a consequence, while a higher hotspot density per unit volume should produce higher SERS signals, protein molecules spread over a larger Ag surface, causing a lowered SERS response. Additionally, internal hotspots are shielded by more exposed nanostructures and might not contribute to the final SERS signal.[2]

Further insight into the SERS response of the AgNWs@PTFE substrate was obtained by a theoretical simulation of the E-field distribution. The largest E-field value was found at the junctions between AgNWs and quantified as $|E|/|E_0|$ ~5.3 within a volume at the interface between two crossed AgNWs (Figures 3a,b). By careful inspection of AFM topographies, we may note that this configuration is experienced by at least 80% of the wires. Other less common configurations include isolated and bundled AgNWs laying on the PTFE surface. We estimated an $|E|/|E_0|$ ~3.5 in a volume in-between a single wire and the PTFE surface, which is justified by a LSPR coupling with the dielectric substrate (Figure 3c),[41] being optimal at the extremities of the wire (Figure 3d). When bundled AgNWs on PTFE are considered (**Figure 3**e), the hotspot generated along the intersection prevails (Figure 3f), resulting in $|E|/|E_0|$ ~4.5 In summary, the SERS intensity follows the order:

$I_{crossed} > I_{bundle@PTFE} > I_{isolated@PTFE} > I_{tip.}$

This result reveals a localization of the strongest fields at interstitials between AgNWs. These have been previously indicated as mainly responsible of the SERS activity of AgNW assemblies showing a SERS enhancement surpassing that of the isolated counterpart due to a strong plasmon coupling effect.[42] At the same time, the influence of the supporting material in altering the E-field distribution is brought to light, resulting in asymmetric localized plasmons confined at nanoparticle/dielectric gap.[43] Although the larger space available for molecular adsorption and detection provided by the hotspots within bundled AgNWs and at the AgNWs/PTFE junctions with respect to those inside crossed AgNWs, the prevalence of the latter in the AgNW assemblies suggests that it will largely govern the Raman enhancement. In spite of the large E-field confinement as observed on a nanometer scale, this doesn't affect the reproducibility in the SERS signals of the AgNWs@PTFE substrates as a consequence of averaging the different hotspot responses within each acquisition laser spot.

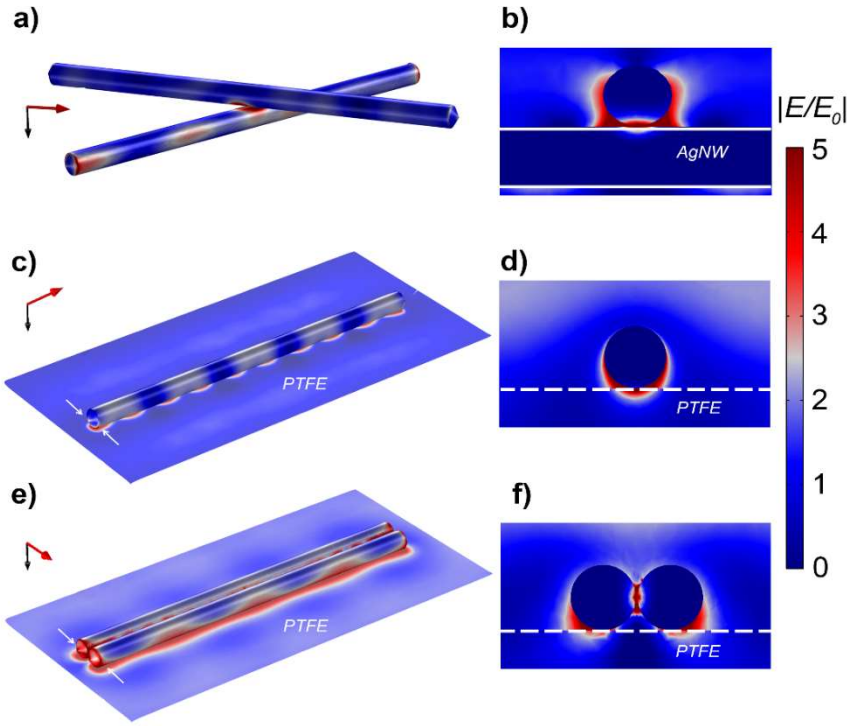

Figure 3. FEM simulations of the E-field intensity in-between two crossed AgNWs in air (a); in the proximity of an AgNW laying on a PTFE surface (c); within two bundled AgNWs laying on a PTFE surface (e). The configurations providing maximum E-field intensities are visualized. 2D sections of (a), (c) and (e) calculated at the junction between nanowires (b) or nearby the ends of the nanowires (arrows in (c,e)) are also reported.

As a second step toward the realization of SERS substrates for practical and rapid analytical testing, we devoted our further efforts in tailoring the SERS substrates in the form of spot arrays. The use of spots at constant surface area confining a sample drop there accommodated is primarily attracting because of the possibility to standardize the sample deposition and to perfect the reproducibility. Our choice of using laser ablation to pattern the AgNWs@PTFE substrate was mainly motivated by: 1) a rapid and accurate texturing procedure and 2) the absence of additives needed as occurs in screen- or in ink jet-printing of nanomaterials. The latter require suitable organic media and stabilizing agents in adjusted amounts to sustain enough viscosity for uniform printing and to prevent edge-leakage or nozzles blockage, respectively.[13,44] Instead laser patterning promises a contaminant-free procedure that discards anomalous peaks from interfering in SERS spectra. Laser ablation is already being implemented in many industrial applications requiring engraving, cutting or cleaning such as microstructuring and drilling of electronic components, 3D-writing on glass, plastic and ceramic, removal of surface coating, etc..[45-47] Spots of a predefined diameter with in the 1 ÷ 2 mm range were initially obtained (Figure 1, step 2; Figure 4) and their attitude towards influencing the evaporation behaviour of drying water drops was evaluated (Figure 5). Different deposition and evaporation profiles were observed upon dropping a 5 µL water amount on the top of plain and patterned AgNWs@PTFE substrates tuned at the optimal AgNW density (*i.e.* 0.1 µg/mm^2). By adjusting the AgNW spot size to approach the diameter of the drop contact area on plain AgNWs@PTFE substrates (*i.e.* 2 mm in the case of 5 µL water drop), an increase of the contact angle from 100° to 118° of the as-deposited drop was observed (Figure 5a) and explained by a confinement of the drop within the surrounding PTFE hydrophobic barrier with consequent suppression of drop spreading. In this case the drop keeps an almost constant contact area even after complete evaporation to the opposite of

what occurs in the case of pure PTFE and plain AgNWs@PTFE (Figure 5b). Concurrently the contact angle of the drying drop on the spot decreases regularly while occasional pinning with an irregular drop collapse characterizes plain AgNWs@PTFE substrates (Figure 5a)

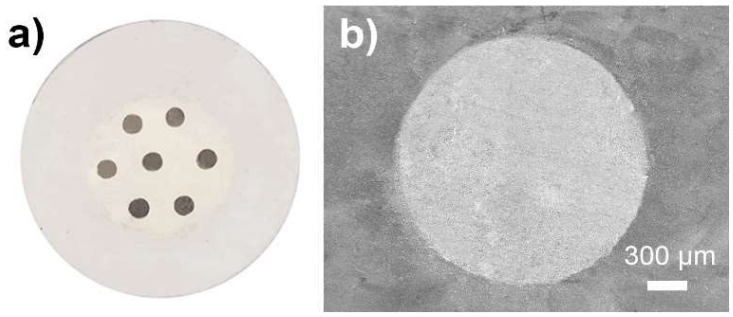

Figure 4. (a) Optical image of a laser-patterned AgNWs@PTFE substrate. (b) SEM image of a laser-patterned AgNWs@PTFE substrate centred on a single spot.

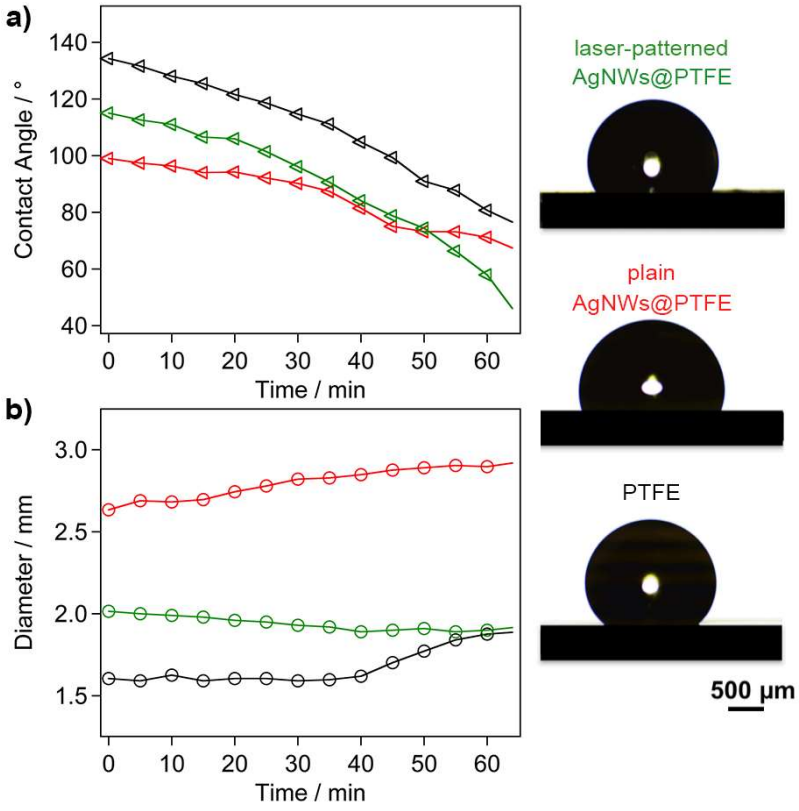

.

Figure 5. Contact angle (a) and diameter (b) values of a 5-µl water drop placed on pure PTFE (black line), plain AgNWs@PTFE substrate (red line) or a single spot of laser-patterned AgNWs@PTFE substrate (green line) at different times during drop drying at room temperature. Corresponding contact angle images of 5 µL water drops soon after deposition on pure PTFE, and on plain and spotted AgNWs@PTFE substrates are reported on the right. The AgNW density of the AgNWs@PTFE substrates was fixed at 0.1 µg/mm^2.

Importantly different evaporation pathways are responsible for determining different distributions of the drop content, once evaporated. Specifically smaller contact angle values usually lead to larger deposition areas with lower and uneven molecular densities usually affected by "coffee-ring" deposits.[48] Conversely, when the liquid sample forms a high contact angle, the molecules are forced to gather within small areas upon evaporation and the deposition becomes more homogeneous.[49] Thus, starting contact angles as much as possible approaching the high-end values of pure PTFE as occurring in the case of the laser-patterned AgNWs@PTFE appear preferred to achieve reliable SERS measurements. The attempt to reduce the spot diameter below 2 mm at unvaried sample volume failed to further improve the SERS signal (not shown). In fact in this case the liquid overflows the spot edges and molecular deposits form in the peripheral PTFE area around the spot.

To investigate the benefits of confining sample drops within well-defined spots, we compared a SERS map of a protein deposition from a single plasmonic spot of the laser-patterned substrate with that obtained from the area occupied by a protein deposition in the case of a plain AgNWs@PTFE substrate (at the same 0.1 μg/mm^2 AgNW density). Compared to the latter where a coffee-ring distribution of deposited protein is apparent, in the laser-patterned substrate the molecules appear homogeneously covering the AgNWs spot area, with minimal fluctuations and maximal relative standard deviation (RSD) values not exceeding 10% (Figures 6a,b). We note that this scenario is lost when a twofold AgNW density spot is considered suffering from uneven signal distribution, which confirms again our initial observations (Figure 2) on the nanoparticle density of choice. A uniform molecular distribution is also beneficial to maximizing molecule/hotspot interactions leading to SERS spectra showing higher intensity values on average than in the case of the plain substrate (Figure 6c) and with enough signal down to submicromolar concentration values of protein.

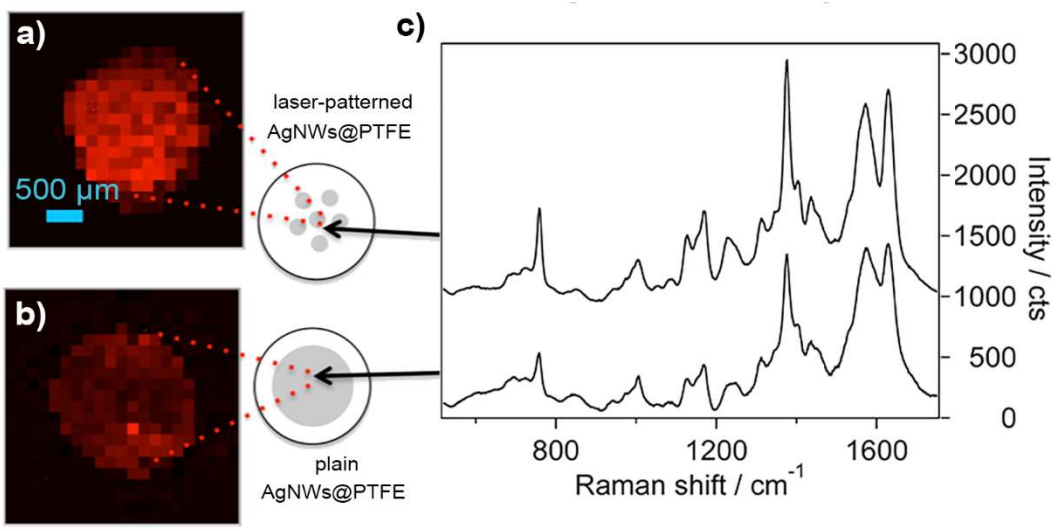

Figure 6. SERS maps (λ_{ex} = 532 nm, 450 points, 150 μm step size) over a 5-μl drop deposition of Mb (1×10^{-6} M) on a single spot of a laser-patterned (a) or on a plain (b) AgNWs@PTFE substrate and resulting average spectra (c). The 1372 cm^{-1} (ν_4) band of Mb was considered for mapping. The RSD values referred to this peak are ≤10% and ≥15% for the laser-patterned AgNWs@PTFE and the plain AgNWs@PTFE substrates, respectively. The AgNW density of AgNWs@PTFE substrates was fixed at 0.1 μg/mm^2.

A quantitative estimate of the signal amplification provided by the laser-patterned AgNWs@PTFE substrates at the optimal Ag density was obtained by calculating the SERS enhancement factor EF. By considering the 1086 cm^{-1} peak from the SERS spectrum of 4-methylbenzenethiol (MBT), a common SERS probe forming self-assembled monolayers (SAM) on silver, and the 1372 cm^{-1} peak from the SERS spectrum of Mb, EF values of 1×10^6 (MBT) and 6×10^5 (Mb), and 3×10^6 (MBT) and 9×10^5 (Mb), were obtained at λ_{ex} = 532 and λ_{ex} = 785 nm, respectively, which overcomes the enhancement capabilities of recently proposed SERS methods for biomolecule detection.[23,24,30]

Once clarified fundamental aspects regarding nanowire density and geometry to improve the signal gain of AgNWs@PTFE substrates, we tested them for practical and rapid analysis of biomolecules. The possibility to vary the excitation conditions throughout the visible-NIR range is of particular significance for both structural investigations and detection of biomolecules. For example, the heme group of Mb will mainly govern the SERS spectrum when operating in resonance conditions at 532 nm (Figures 2,6) while signals belonging to the peptide backbone and amino acid side chains are revealed when a 785 nm is used (Figure 7a). In general, longer excitation wavelengths are usually preferred for Raman-based diagnostics to avoid the superposition of heme bands as well as background fluorescence usually affecting many biological samples when operating at excitation wavelengths below 700 nm.[50]

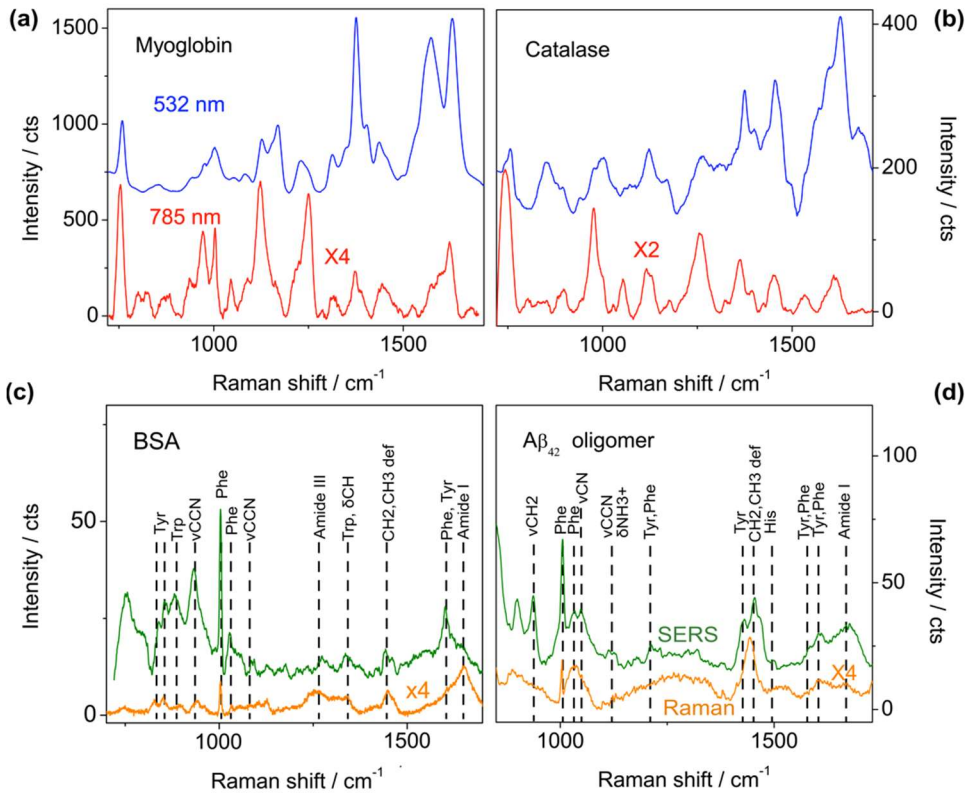

Figure 7. SERS spectra of Mb (a) and catalase (b) at 1×10^{-6} M under λ_{ex} = 532 nm (blue) and λ_{ex} = 785 nm (red) deposited on laser-patterned AgNWs@PTFE. SERS spectra (green) of BSA (c) and $A\beta_{42}$oligomer (d) at 1×10^{-6} M under λ_{ex} = 785 nm deposited on laser-patterned AgNWs@PTFE. Raman spectra (orange) of 1×10^{-3} M BSA and Aβ42 oligomer are also shown as reference.

The flexibility of the spotted AgNWs@PTFE substrate is here further demonstrated by SERS detection of larger proteins, specifically the hemoprotein catalase (M_w = 250 kDa) and bovine serum albumin (BSA, M_w = 68 kDa), whose SERS identification previously proved not trivial at low concentration values,[51-53] mainly because of their large molecular size leading to a variable nano-bio interface.[54-56] Sharp bands were obtained for both proteins. The SERS spectrum of catalase (Figures 7b) under out-of-resonance conditions (at λ_{ex} = 785 nm) is less affected by the high cross-section bands of the heme group as similarly noted for Mb, revealing modes ascribed to aminoacid residues. In the case of BSA (Figure 7c), characteristic vibrations of aromatic aminoacids at 838/855 cm^{-1} (Tyr), 880 cm^{-1} (Trp), 1003/1027 cm^{-1} (Phe) and 1601 cm^{-1} (Phe, Tyr) as well as to the peptide backbone and aliphatic residues at 1270 cm^{-1} (Amide III), 1445 cm^{-1} (CH_2, CH_3 deformations) and 1651 cm^{-1} (Amide I) are visible in the Raman spectrum and accordingly identified in the SERS spectrum. We finally performed a SERS characterization on amyloid aggregates, which show a marked heterogeneity and metastability complicating their structural analysis by standard structural biology techniques,[57] as well as by spectroscopic methods, including plasmon-enhanced spectroscopies.[58-62] Figure 7d shows the on-spot SERS spectrum obtained by drop deposition on a AgNWs@PTFE substrate of β-amyloid peptide $A\beta_{42}$ oligomers, which are associated with Alzheimer's disease (AD) and a well recognised biomarker of the cerebrospinal fluid of AD patients. Here, strong peaks emerge in the SERS spectrum: 940 cm^{-1} (ν_{CH2}), 1003 and 1030 cm^{-1} (Phe), 1049 cm^{-1} (ν_{CN}), 1454 cm^{-1} ($\delta_{CH2,CH3}$) and 1605 cm^{-1} (Tyr, Phe) while less intense spectral features are observed at 1115 and 1126 cm^{-1} (ν_{CCN}, δ_{NH3+}), 1430 cm^{-1} (Tyr), 1498 cm^{-1} (His) and 1582 cm^{-1} (Tyr, Phe). Considerations on relative peak intensities and comparison between Raman and SERS spectral features may also prove useful to gaining insights into surface structuring of the biomolecule. For example, matching Raman and SERS bands of BSA may suggest that the protein structure is negligibly affected by the interaction with the AgNWs, even if prevailing peaks at 1003 cm^{-1} and 1601 cm^{-1} represent an indication of Phe and Tyr residues spatially near the hotspots. Analogously, the anomalous intensities associated with aromatic, aliphatic and N-containing groups of $A\beta_{42}$ oligomers with respect to their counterpart in the reference Raman spectrum let entail that both electrostatic (by amino groups) and hydrophobic (by aliphatic and aromatic residues) interactions are established with the silver and/or that both charged and hydrophobic aminoacid residues are in direct proximity with the metal, and thus exposed on the amyloid surface.

2.2. Conclusions

A novel strategy of SERS assay for rapid and effective detection as well as for simple structural characterization of biomolecules is presented. In our scheme, by implementing a mixed bottom-up/top-down approach, dot arrays of AgNWs clustered on hydrophobic supports are obtained and proven as efficient sensing SERS substrates for catching the analyte content from a minute amount of liquid sample and its rapid SERS inspection. By a simple flow-through method, AgNWs assemblies stuffed with interstitial hotspots are rapidly realized. Afterwards, laser ablation is exploited to operate a substrate patterning in the form of regular SERS-active spots producing intense local E-fields. The system overcomes the issues typically encountered with aggregating metal colloids, which suffer from scarce standardization perspectives. Overall, our attempts may represent a concrete chance for progressing SERS toward widespread commercially viable sensing applications including diagnostics at the point-of-need settings and on-site analyses.

2.3 Experimental Section

2.3.1 Materials

Ethylene glycol (EG, 99%) was obtained from Scharlab. Polyvinyl pyrrolidone (PVP, M_w 40000), $AgNO_3$, AgCl, isopropanol (99.5%) and ethanol (≥99.8%) were purchased from Sigma-Aldrich. Hydrophobic (25 mm diameter × 80 μm thickness) PTFE filter membranes of 0.45 μm pore size by Sartorius were used. Mb from human heart, BSA and catalase from bovine liver were obtained from Sigma-Aldrich and used as received. $A\beta_{42}$ oligomers were prepared as previously described.[63]

2.3.2 AgNWs synthesis

AgNWs (1.5 ± 0.9 μm in length, 78 ± 16 nm in diameter) were synthesized by the chemical reduction method of silver nitrate in EG and PVP, according to Hu et al.[64] with minor changes. Briefly, in one liter round bottom flask, 3.0 g of PVP were added and dissolved in 180 ml of EG in few hours. After the complete dissolution, the solution was heated up at 170 °C. To this flask, 225 mg of AgCl were added and after 3 min a solution of $AgNO_3$ (990 mg of $AgNO_3$ in 20 ml of EG) was also dropped inside during a 10 min time (2 ml/min). The reaction proceeded for additional 30 min at 170 °C. After 30 min, the light-grey suspension was cooled down in ice water bath. The suspension was 3 times washed with acetone and the AgNWs were precipitated by centrifugation (3000 rpm, 15 min). The purified nanowires were finally suspended in isopropanol and characterized by SEM (Zeiss, EVO MA 10) and UV-Vis spectroscopy (PerkinElmer Lambda 35 UV/Vis).

2.3.3 Arrays fabrication

The initial suspension of AgNWs (Ag 0.017 wt%) was diluted in different ratios in ethanol. An amount of 2 mL of solution was then passed through the PTFE membrane by using an Amicon Stirred cell Model 8003, 3 ml (Millipore) cell. Specifically the membrane was initially wetted by dipping it in ethanol and then placed into the filter holder. Then the AgNW solution was filtered by adjusting the pressure at an optimized value of 350 mbar. The substrate was then extensively washed in anhydrous ethanol and there stored until further use. Part of the as-fabricated substrates was finally patterned in the form of dot arrays by using a laser ablation procedure. Briefly, as the AgNWs have a considerable absorption coefficient (of the order of 10^5 cm^{-1}) in the blue-green spectral region, the substrates were processed by using the second harmonic (532 nm) of a Q-Switch Nd:YAG laser (10 ns pulse duration). The fiber-coupled laser output was lens-imaged to form a spot of 2.5 mm diameter on the sample plane. The beam radii ω_0 was precisely determined by applying the spot regression method for Gaussian laser beam profiles. A custom designed mask, composed of round metal rods (within the 1÷2 mm diameter range), was positioned onto the AgNWs layer to shield incoming laser light and create dot arrays. To minimize undesired thermal effects of PTFE membrane, array fabrication was performed by full immersion in a glass cell containing ethanol. Then, laser patterning was performed by scanning in orthogonal directions at fluence values slightly above the AgNWs single-pulse ablation threshold fluence. The optimal removal window for surface densities between 0.1 and 0.4 μg/mm^2 was found to be in the 160-250 mJ cm^{-2} range. Thus, 160-180 mJ cm^{-2}, 2 Hz pulse repetition frequency and full immersion in ethanol were selected as the best parameters to pattern the AgNWs@PTFE substrates used in the SERS experiments of this study. The morphology of the laser-patterned AgNWs@PTFE substrates was inspected by tapping mode AFM by using a JPK NanoWizard III Sense scanning probe microscope at 250÷300 kHz drive frequency and 0.5 Hz scan rate and equipped with single beam uncoated silicon cantilevers (μMash HQ:NSC15 Cr-Au BS).

Contact angle measurements were conducted under a home made set up by placing a 5-μL aqueous droplet onto the AgNWs@PTFE substrate and following the drop evolution during its evaporation.

2.3.4 SERS measurements

SERS measurements were carried out using a microRaman spectrometer (Xplora, Horiba) working at 532 nm or 785 nm laser wavelengths with a 1200 grooves/mm grating. The backscattered light was collected by a 10×objective with 0.25 NA, which generates a 7-μm large laser beam waist and provides an average SERS response, minimizing possible signal variability. Laser power values at the sample of 115 μW at 532 nm and 598 μW at 785 nm and an integration time of 10 s with two accumulations were used. SERS data are baseline corrected and represent an average of a minimum of 10 spectra collected by mapping experiments over 12 mm^2 areas with a step size of 50 ÷ 150 μm, unless specified otherwise.

2.3.5 FEM simulation

Our calculation uses a commercial FEM package, the wave optical module of COMSOL multiphysics (v 5.1), to find the electric field distribution in the near proximity of the AgNWs. We chose to depict the AgNW as a cylinder with smoothed pointy ends, with radius 40 nm and total length 1.5 μm. Figure 3 shows the COMSOL simulation domain, with the interface between air and PTFE at $z = 0$ and the surroundings of the wire having refractive index $n1 = 1$ for $z > 0$, and $n2 = 1.3$ for $z < 0$. AgNWs are illuminated by a 532 nm plane wave from above and linear polarization at different angles. In general, incident light polarizes the ends and gives rise to a standing surface charge wave propagating along the wire.

3. AgNWs@G-paper substrate

We introduce a highly responsive SERS substrate specifically designed for biodetection of small sample drops and aimed at overcoming some limitations of the previous system as a result of the use of a simplified fabrication procedure and the introduction of a graphene underlayer to improve the SERS response. On the one hand, the fabrication setup was implemented with a common nebulizer for aerosol therapy, assuring a facile deposition of AgNWs without the need for expensive, time-consuming, or highly specialized procedures. Several studies proposed the direct deposition of sprayed colloids on sample surfaces to probe the surface composition of atmospheric particles [64], inks, and colorants in historic documents [65] or pesticides in fruits [66,67]. On the other hand, the preparation of 2D plasmonic substrates by sprayed or nebulized nanoparticles and their use within SERS assays for the determination of trace substances remains an underexplored field, so far [68-72]. Another feature of the proposed substrate deals with the use of graphene paper to host the nanoparticle deposits, offering a flat background and imparting superior reproducibility. The use of graphene as a support for plasmonic nanostructures to improve SERS signal detection has become a popular choice within the SERS community in recent years. Several excellent groundworks have been published in this field, demonstrating remarkable benefits offered by the introduction of a graphene sublayer once the resulting hybrid systems are tested against small model and organic analytes [73-77]. However, the demonstration of a real efficacy of these systems in the analysis of molecular species of biological/biomedical interests still represents a challenging gap to overcome before accepting them as effective tools in everyday life applications.

3.1 Results and Discussion

Underlying our work was our established effort to create a substrate specifically designed to increase the local molecular density at plasmonic hotspots produced from a AgNWs network to maximize SERS signals from molecules typically showing a low Raman cross-section [83-85]. Briefly, we first adopted a standard wet chemistry procedure based on the polyol process to produce 5 ± 1 μm in length, 48 ± 10 nm in diameter AgNWs. Two-dimensional plasmonic substrates were then rapidly obtained by a nebulizing jet of a proper amount of AgNWs colloidal solution toward a 2 × 2 cm^2 piece of thin graphene paper (G-paper) (Figure 8). The system included the possibility to impart a custom spacing of the graphene target to tune the covered airbrushed area, which was optimally set at 1 cm.

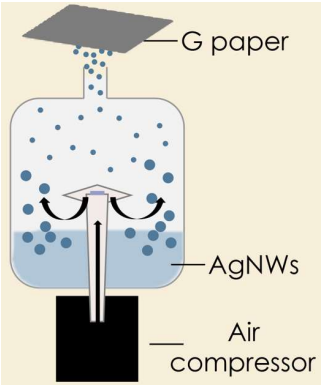

Figure 8. Scheme of aerosol deposition of AgNWs on G-paper.

In an attempt to create homogeneous AgNWs films, we varied the deposition time of the original AgNWs batch. A complete and homogeneous coating of the graphene support was obtained after 10 min of aerosol deposition (longer times did not further improve AgNWs coverage of the underlying graphene layer), while lower time values resulted in an uneven distribution (Figure 9a–c). Once we fixed the deposition time to 10 min, we varied the density of deposited AgNWs by sequential dilutions of the particle dispersion. In this case, a 10 mm-wide array of 1.5 mm in size silver spots was obtained by introducing a patterned mask consisting of a thin PET layer placed on the top of the G-paper once wetted with ethanol before nebulization, which ensured a temporary and a tight adhesion at the graphene/PET interface, in turn, avoiding possible edge-leakages of the nanoparticle solution. The mask was exactly centered with the graphene support (see the circled area in Figure 9a) to produce array spots at a comparable surface density of AgNWs. After deposition and mask removal, a pattern of regular and homogeneous AgNWs spots appeared well imprinted on the air-dried graphene (Figure 9d). Array spots obtained by 1:2 dilution of the AgNWs batch corresponding to a 0.5 mg/L density resulted to greatly enhance the Raman signal of 1 × 10^{-6} M hemoglobin (Hb) once excited at 532 nm (Figure 9e). We were able to detect the characteristic signals of Hb mainly ascribed to the heme group[87,88] down to 0.2-mg/L AgNWs density. After further dilution of deposited AgNWs, the protein signals progressively lost intensity, becoming undetectable at 0.02 mg/L where the spectrum corresponded to that of the underlying graphene (inset of Figure 9e). The above-optimized fabrication parameters were thus selected to optimally produce spotted AgNWs@G-paper substrates.

We point out that the as-fabricated substrates allow to support the analysis of minimal quantities (2 μL) of biomolecule solution, which were initially dropped onto an array spot. They were then confined by a high contact angle formed with the surrounding hydrophobic graphene barrier and finally effectively inspected under the Raman microscope once dried (Figure 10).

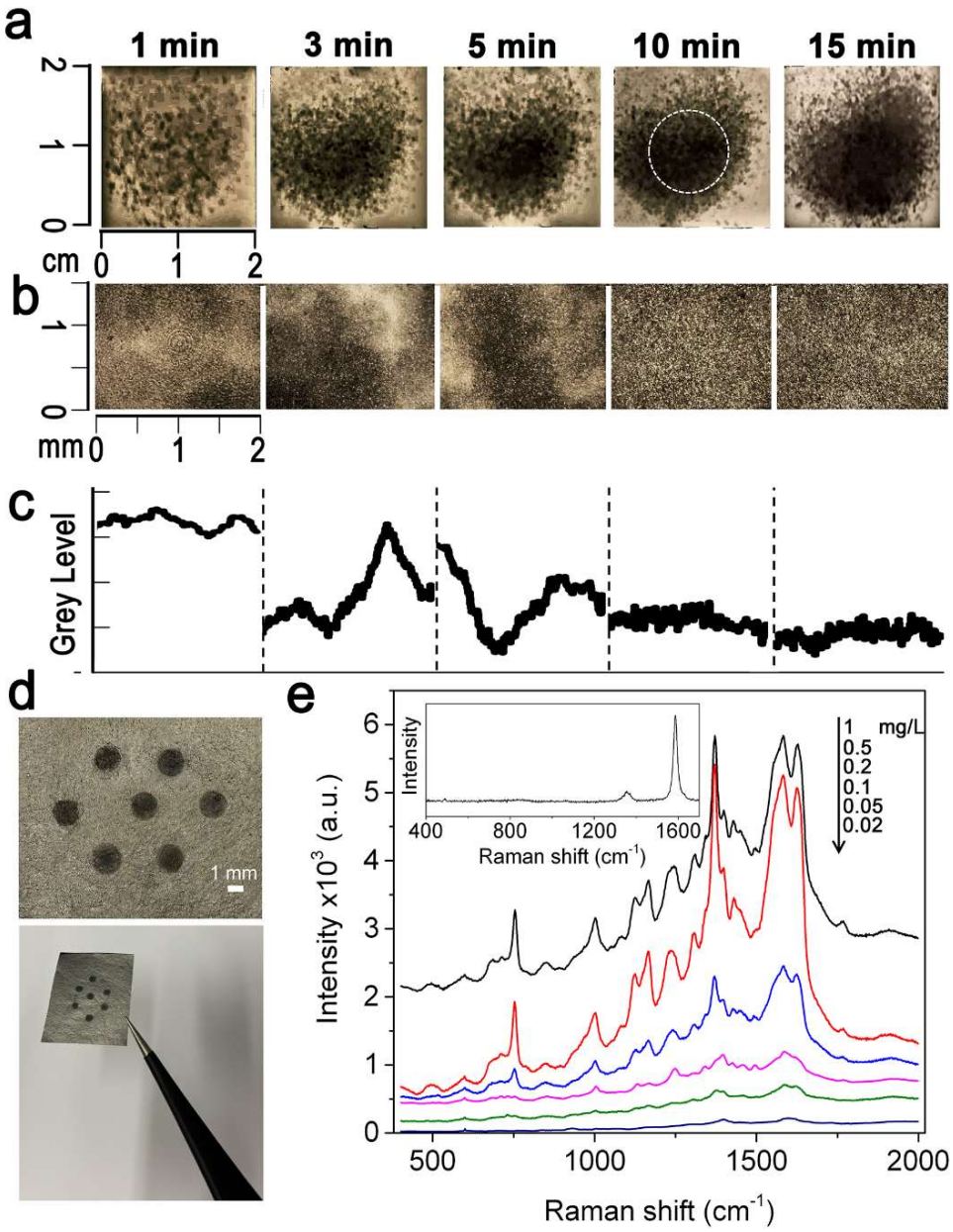

Figure 9. Fabrication of AgNWs@G-paper substrates. (a) Aerosol deposition of a 1 mg/L AgNW solution at different deposition times (varied from 1 min to 15 min) on a 2 × 2 cm² piece of G-paper. The central 1 × 1 cm² area of a AgNWs deposition showing a homogeneous density of deposited AgNWs (as highlighted by a dashed circle superposed on the sample at 10 min deposition) was considered for the following fabrication of patterned substrates (as in (d)); (b) Optical micrographs showing a 2 × 2 mm² magnification of the central part of the substrates prepared in (a); (c) Grey level profiles showing the distribution of AgNWs within the areas considered in (b). A flat profile (as obtained after 10 min of AgNWs deposition) corresponds to a homogeneous AgNWs coating of G-paper; (d) Appearance of a AgNWs@G-paper substrate and a magnification of the AgNWs spot array as obtained by interposing a PET patterned mask between the nebulizing jet and the G-paper; (e) SERS spectra of Hb (1 × 10⁻⁶ M) on different AgNWs@G-paper substrates obtained by decreasing the density of nebulized AgNWs within the 1 ÷ 0.02 mg/L range once set the deposition time to 10 min (black, 1 mg/L; red, 0.5 mg/L; blue, 0.2 mg/L; purple, 0.1 mg/L; green, 0.05 mg/L; blue 0.02 mg/L). The 0.5 mg/L density provides the most intense Hb signals and was thus selected for further production of AgNWs@G-paper substrates. Spectra represent the average of over 20 acquisitions. Inset: Raman spectrum of G-paper.

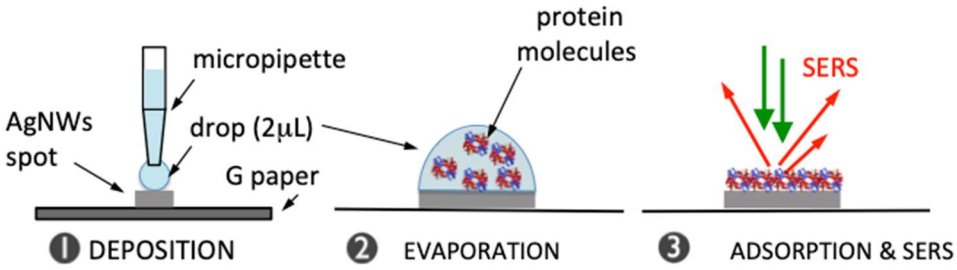

Figure 10. Working scheme of AgNWs@G-paper substrates: a small (2 µL) drop of protein solution is deposited on a AgNWs spot and confined due to the surrounding graphene hydrophobic barrier. After drop drying (~15 min at room temperature), the drop content is physically adsorbed on the surface of AgNWs and exposed to an effective E-field generating intense SERS signals.

Our initial aim in choosing graphene as a low-cost support for nanoparticles was dictated by three main considerations: (1) superior hydrophobicity behavior with respect to other popular supports for disposable substrates as cellulose paper, thus enabling analyte confinement and concentration enrichment, as discussed above; (2) low Raman signals in the fingerprint region as compared to other candidate hydrophobic substrates as polytetrafluoroethylene (PTFE) and polydimethylsiloxane (PDMS) and limited to D (1354 cm^{-1}) and G (1584 cm^{-1}) band signals (Figure 9e inset); (3) additional features as quenching of autofluorescence signals frequently encountered in biomolecules [89] and better integration with biological entities, such as cells [90], for advanced biological analyses. With particular reference to the G-paper, further advantages were represented by easy-handling and easy-resizing, low-cost (0.2 €/cm^2), and flexibility (with potential in the analysis of unflatten surfaces), which makes it even more attractive.

In the following, we showed that the choice of a graphene paper proved also advantageous in improving signal stability as well as in providing an ultra-flat background in comparison with other popular disposable supports for simple and rapid SERS analyses. The AFM investigation of AgNWs@G-paper revealed a homogeneous distribution of AgNWs on the micron scale (Figure 11a). The latter hypothesized a regular distribution of SERS hotspots, which was further demonstrated by inspecting the point-to-point signal of Hb over large areas (Figure 11b). A maximum relative standard deviation (RSD) <10% for the main Raman peaks of Hb was observed in this case. Conversely, when replacing G-paper with PTFE, AFM highlighted the presence of clustered wires unevenly covering the support surface (Figure 11c) and causing a larger point-to-point SERS signal variability (Figure 11d), which could be explained by a heterogeneous amplification of protein molecules [91]. G-paper played the role of catching interface [92] against sprayed wires, immobilizing them into a uniform surface distribution, which was not the case with plastic supports as PTFE. Furthermore, the high thermal and electrical conductivity of graphene [93] could contribute to buffering the laser radiation impact, generating well-resolved SERS spectra.

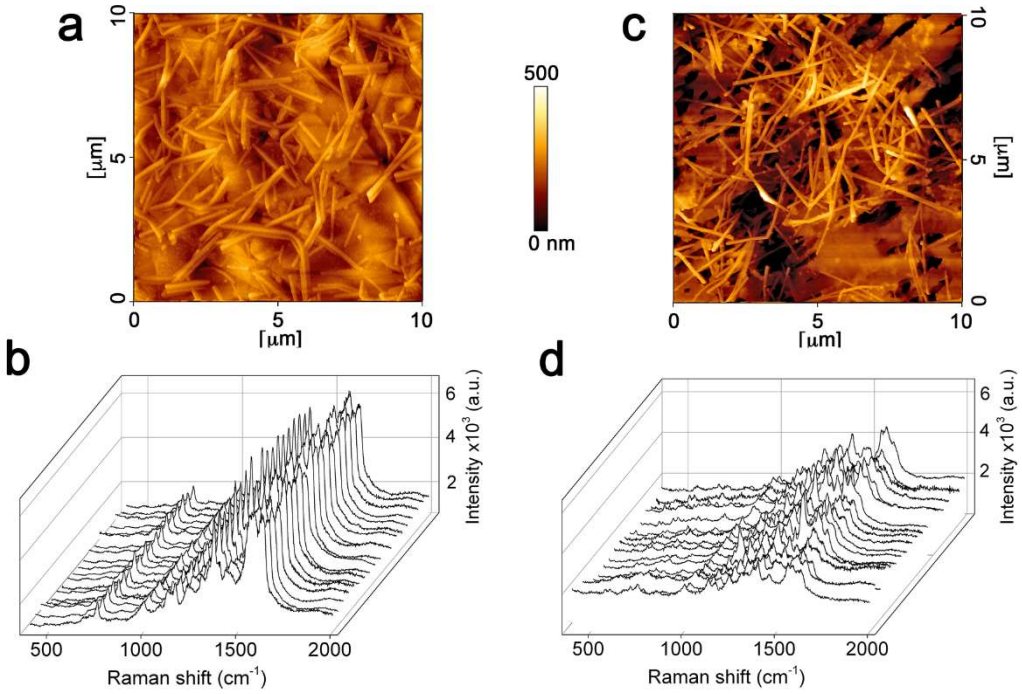

*Figure 11. AFM topography of sprayed AgNWs on G-paper (**a**) and on a PTFE support (**c**). Random SERS spectra of Hb (1 × 10^{-6} M) as obtained by point-to-point mapping over 12 mm^2 areas with a step size of 100 µm from sprayed AgNWs on G-paper (**b**) and on a PTFE support (**d**).*

The amplification provided by the as-fabricated AgNWs@G-paper was evaluated by calculating the SERS enhancement factor (EF). EF is defined as the ratio between I_{Raman} and I_{SERS} normalized to the average number of molecules dispersed in solution N_{Raman}, for the Raman measurement, and adsorbed onto the AgNWs hotspots N_{SERS}, for the SERS measurement, respectively, which were present in the scattering volume

$$EF = \frac{I_{SERS}/N_{SERS}}{I_{Raman}/N_{Raman}}$$

An *EF* value of 4 × 10^6 was calculated, proving an enhancement ability of the same order of magnitude or higher than that from recently proposed low-cost disposable SERS substrates including those based on AgNWs assemblies[14, 87-90]. We tried to gain further insights into the high-quality SERS profiles of AgNWs@G-paper by theoretical simulation of the electromagnetic field distribution. We may further note by AFM and optical analysis (Figures 11) that the main part of AgNWs laid almost planar and in contact with graphene or forming single or few junctions with other AgNWs, suggesting the latter as the most representative configurations of the SERS enhancing capacity of AgNWs@G-paper substrates (Figures 12a,b). Nonetheless, the highest E-field values were found at the interfaces between AgNWs and graphene (Figure 12a). This is mostly not the case with planar SERS systems previously considered composed of AgNWs assemblies due to a higher wire density used, producing a large number of effective hotspots at crossed junctions [83, 91,92]. The presence of graphene was instead supposed to favor AgNW/graphene with respect to AgNW/AgNW interactions, as discussed above (Figure 11a,b), leading to elongated (Figure 12a) hotspots providing a large space available for analyte accommodation and its detection. The higher average E-field value estimated at the graphene/AgNW interface hotspots, as compared to those formed at AgNWs

interstitials ($(|E|/|E_0|)_{graphene/AgNW}/(|E|/|E_0|)_{AgNW/AgNW}$ = 1.2), could be explained by taking into account the higher refractive index of graphene in comparison to other popular supports, which boosts the near field within the gap between metal and graphene, as shown in Figure 12c. The near field value calculated at a graphene/AgNW interface under λ_{ex} = 532 nm appears ~2-fold larger ($|E|/|E_0|$ = 44) than that at a PTFE/AgNW ($|E|/|E_0|$ = 24) or cellulose/AgNWs ($|E|/|E_0|$ = 19) interfaces. As SERS enhancement is proportional to the fourth power of the E-field, an average $EF = 3.7 \times 10^6$ is obtained in the former case. A large matching between simulated and calculated *EF* let us hypothesize that the electromagnetic mechanism (EM) largely prevailed in AgNWs@G-paper substrates over a chemical mechanism (CM), as previously reported, as a possible additional effect in the SERS response of graphene-based substrates [93].

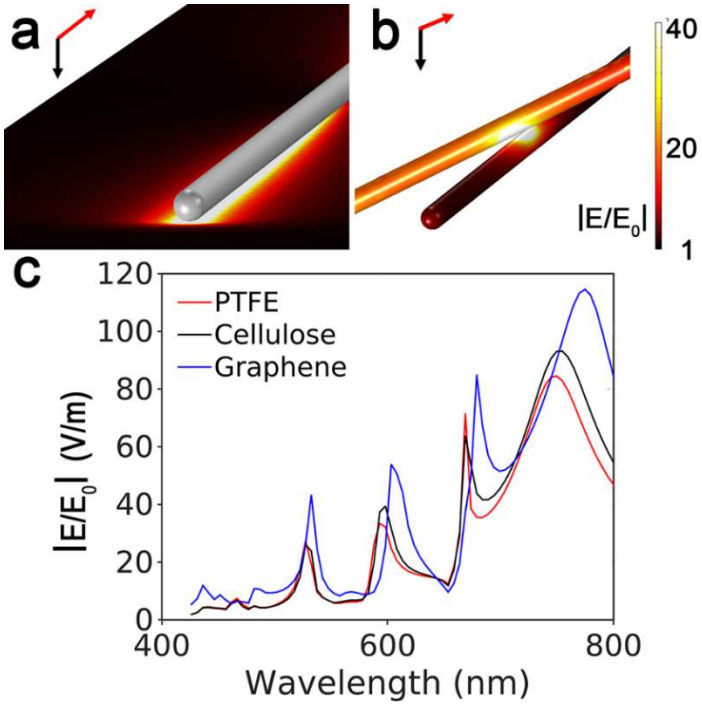

*Figure 12. **(a)** FEM simulations of the E-field intensity in the proximity of a AgNW laying on a graphene surface. The E-field intensity is visualized for the plane corresponding to the G-paper surface while the wire is pictured as uniform grey color for better clarity. **(b)** The E-field intensity is visualized for two crossed AgNWs in the air. In this case, the E-field intensity on the wire surface is visualized. **(c)** Maximum E-field variation within the visible spectral range as simulated at the interfaces between a AgNW and graphene (blue), PTFE (red) and cellulose (black).*

Another significant aspect in the choice of a SERS substrate resides in its background contribution to the overall SERS signal and generated at the interface between plasmonic layer and underlying support, which becomes critical especially in the detection of species with reduced SERS response, such as biomolecules. In Figure 13, a comparison between the background SERS signals of AgNWs on G-paper and that on popular substrates for disposable SERS substrates as nitrocellulose and PTFE is displayed. The background signal generated in the presence of G-paper remains the lowest

regardless of the laser power employed and limited to the superposition between Raman modes of graphene and intrinsic signals pertaining to the AgNWs. On the opposite side, a fluorescence background governs the nitrocellulose and PTFE profiles (Figure 13a), accompanied by the remarkable appearance of intense and broad amorphous carbon signals at 1350/1580 cm^{-1} [94] by the nitrocellulose-based substrate at high irradiation values (Figure 13b), which affects partially or does not affect the signals of PTFE and G-paper, respectively (the latter linearly scaling with power). These results 1) depict graphene as a null fluorescence emitter due to its zero optical bandgap [95], generating an ultra-flat SERS background and 2) confirm the stability of graphene under more extreme power conditions and ascribed to its high thermal conductivity as pointed out.

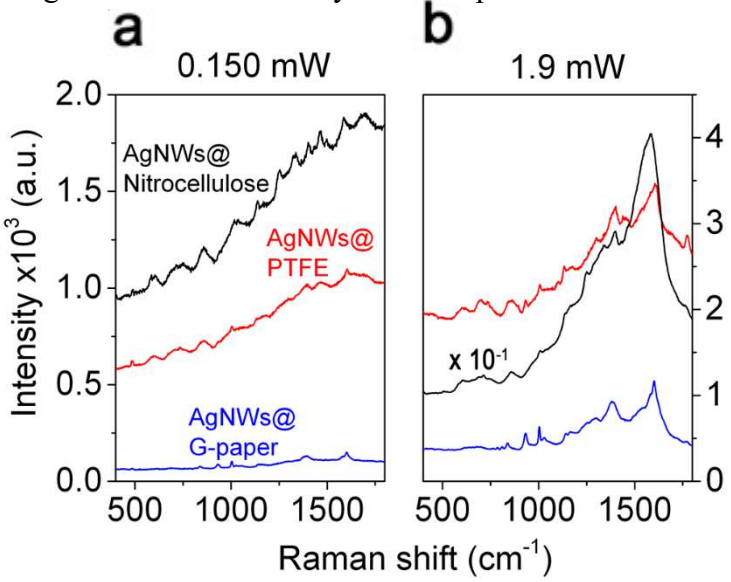

Figure 13. Background SERS profiles of AgNWs sprayed on nitrocellulose, PTFE and G-paper at (**a**) 0.150 mW and (**b**) 1.9 mW laser power at 532 nm. Spectra represent the average of over 20 acquisitions.

We finally evaluated the detection sensitivity of the AgNWs@G-paper substrate by decreasing Hb concentration from 1×10^{-5} M to 1×10^{-9} M (1.3 µg to 0.3 ng) (Figure 14a). A sigmoid correlation ($r^2 > 0.99$) between the band area of the 1378 cm^{-1} mode and the amount of protein was observed (Figure 14b), which can be commented on the one hand as a tendency to reach saturation on the available space of the hotspots at high-end values. On the other hand, a detection limit of 1×10^{-8} M was found, which corresponded to about 1 ng of protein in the analyzed sample volume (2 µL), suggesting a high sensitivity of AgNWs@G-paper that overcomes previous detection systems based on unsupported colloidal particles for protein detection including hemoglobin[96,97] .

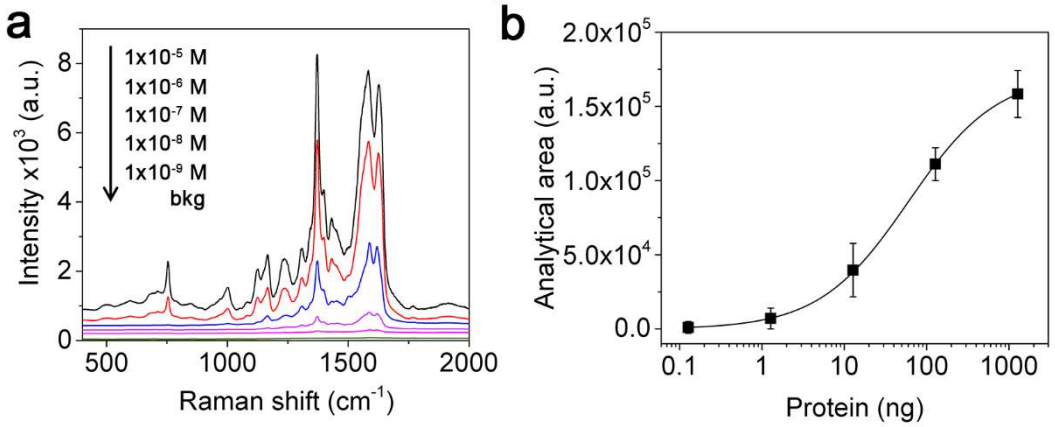

*Figure 14. Detection sensitivity of the AgNWs@G-paper substrate. (**a**) SERS spectra of Hb ranging from 1 × 10^{-5} M to 1 × 10^{-9} M (black, 1 × 10^{-5} M; red, 1 × 10^{-6} M; blue, 1 × 10^{-7} M; violet, 1 × 10^{-8} M; purple, 1 × 10^{-9} M; green, background AgNWs@G-paper signal) corresponding to 1.3 μg to 0.3 ng of protein contained within 2 μL of analyzed sample volume. The background signal produced by the naked substrate is also displayed. (**b**) Correlation between the 1378 cm^{-1} band area of Hb and protein amounts (error bars represent the SD). Spectra and data points represent the average from 20 acquisitions.*

3.2 Conclusions

SERS substrates proposed so far are often unsuitable for the practical detection of biomolecules due to the lack of simultaneous presence of preferred characteristics, such as low manufacturing costs, disposable characteristics, and simplicity for routine use in turn limiting their use at or near point-of-need settings. In this study, we introduced a highly responsive SERS substrate relying on a simple aerosol deposition of AgNWs on graphene paper. The substrate was specifically designed for biodetection of small sample drops at submicromolar concentration. The proposed fabrication procedure relied on low-cost and facile steps that overcome a number of weak points frequently encountered in substrate preparation and patterning. These included the use of contaminating stabilizers to impart sufficient viscosity to nanoparticle inks as usually required in screen or ink-jet printing, as well as the need for dedicated instrumentation for top-down nanoparticle fabrication. Additionally, the presence of graphene improved the SERS response, conferring superior signal stability, low SERS background, and photostability. Overall, the proposed substrate exhibited high SERS efficiency, reliability, and sensitivity, as well as easy handling and usage aspects, meeting many of the requirements for effective and successful SERS detection of biomolecules. Future experiments on AgNWs@G-paper substrates will be aimed at exploring the SERS sensing of larger biological entities as cells for rapid and tag-free screening of tumor diseases (e.g., malignant cells) or to monitor light treatments (e.g., laser-exposed cells) for therapeutic applications.

3.3 Experimental Section

3.3.1 Chemicals

Polyvinylpirrolidone (PVP, M_w 40000), isopropanol (99.5%), myoglobin from horse skeletal muscle (Mb), and hemoglobin (Hb) were purchased from Sigma-Aldrich (St. Louis, MO). Ethylene glycol (EG, 99%) was purchased from Carlo Erba (Milan, Italy). Silver nitrate ($AgNO_3$) and silver chloride (AgCl) were obtained from Cabro S.p.A. (Arezzo, Italy).

3.3.2 AgNWs Synthesis

AgNWs were synthesized by the polyol method. Briefly, 80 mL of EG was heated and thermally stabilized at 170 °C in a flask. Once the temperature had been stabilized, 112.5 mg of AgCl was added to the flask. Meanwhile, 495 mg of $AgNO_3$ and 3 g of PVP were dissolved in 10 mL of EG each. The PVP and $AgNO_3$ solutions were poured into two 10 mL syringes, which were placed in a syringe pump. Three minutes after the addition of AgCl, the slow injection of the two reagents was started with an injection rate of 0.5 mL/min. The reaction proceeded until the injection was finished. Afterward, the flask was cooled in an ice bath. The suspension was poured in 600 mL of acetone to leave AgNWs to spontaneously settle down overnight. Supernatant was removed and AgNWs were

re-dispersed in isopropyl alcohol. AgNWs were characterized by SEM (Zeiss, EVO MA 10, Jena, Germany) and UV-Vis spectroscopy (PerkinElmer Lambda 35 UV/Vis, Norwalk, CT). The concentration of the as-obtained AgNWs suspension was finally determined as 1 mg/L by gravimetric determination.

3.3.3 Fabrication of SERS Substrates

SERS substrates were fabricated by aerosol deposition of AgNWs on 50-μm thick graphene-based paper (G2Nan Sheet 50, Nanesa S.r.l.) as achieved by mechanical compression of small stacks of graphene, which in turn was obtained by exfoliation of expanded graphite. Different AgNWs dispersions, as obtained by sequential dilutions in isopropyl alcohol of the original solution, were aerosolized on varying the exposition time within the 1 – 15 min range by using a common compressor nebulizer emitting micron-sized AgNWs drops for aerosol therapy (Master-Aid Dynamic Aerosol, Pietrasanta Pharma S.p.A., Capannori, Italy). A fixed spacing between the nebulizer output and the graphene paper was maintained by using a third-hand support clip. Before deposition, the graphene was wetted in ethanol and then adhered to a PET mask (Melinex® 454 polyester film, thickness 125 μm, DuPont, Wilmington, DW) patterned with 1.5-mm in size round holes, obtained by mechanical punching.
The overall distribution of deposited AgNWs on graphene paper was investigated by optical microscopy (OM) (Olympus, BX41, Tokyo, Japan). The morphology of AgNWs on graphene paper at the nanoscale was analyzed by tapping mode AFM by using a JPK NanoWizard III Sense (Berlin, Germany) scanning probe microscope at a 250 – 300 kHz drive frequency and a 0.5 Hz scan rate and equipped with single-beam uncoated silicon cantilevers (μMash HQ:NSC15 Cr-Au BS).

3.3.4 SERS Measurements

The as-fabricated substrates were analyzed using a micro-Raman spectrometer (XPlora, Horiba, Kyoto, Japan) working at 532 nm with 1200 grooves/mm grating, an integration time of 5 s, and laser power at the sample of 150 μW, unless otherwise specified. A 10× objective with 0.25 NA (7 μm waist) was used.

3.3.5 FEM Simulation

The electric field distribution in the near proximity of the AgNWs had been evaluated using a commercial FEM package, the wave optical module of COMSOL multiphysics (Stockholm, Sweden, v 5.1), and the MNPBEM MATLAB (Natick, MA) toolbox for the simulation of metallic nanoparticles, using a boundary element method approach [78].
We chose to depict the AgNW as a cylinder with hemispherical ends, a radius of 25 nm, a total length 5 μm, and a refractive index for silver taken from Rakić et al.[79]. An evaluation of the different arrangements established by the nanowires on the substrate was done based on AFM analysis, revealing that the nanowires laid down in contact with the substrate surface and most of them experienced a cross intersection with other wires. That is, we estimated, on average, a number of intersections that were at least 80% of the total number of wires deposited. This is why for our simulation we considered two configurations. In the first one, a AgNW was lying on a substrate with the index of refraction of graphene from Zhu et al. [80]. In the second one, a AgNW was in air,

verifying the proximity of a second crossing wire. In both cases, AgNWs were illuminated by a 532 nm plane wave from above and the calculation of the electric field $|E|/|E_0|$ values were averaged over 5 different polarization angles of the incident light. In general, incident light polarized the ends and gave rise to a standing surface charge wave propagating along the wire[81].

Bibliography

[1] P. L. Stiles, J. A. Dieringer, N. C. Shah, R. P. Van Duyne, *Annu Rev Anal Chem (Palo Alto Calif)* **2008**, *1*, 601.
[2] H. Liu, L. Yang, J. Liu, *TRAC-Trend Anal. Chem.* **2016**, *80*, 364.
[3] R. A. Alvarez-Puebla, L. M. Liz-Marzan, *Chem Soc Rev* **2012**, *41*, 43.
[4] J. F. Betz, W. W. Yu, Y. Cheng, I. M. White, G. W. Rubloff, *Phys Chem Chem Phys* **2014**, *16*, 2224.
[5] Y. Wang, Y. Jin, X. Xiao, T. Zhang, H. Yang, Y. Zhao, J. Wang, K. Jiang, S. Fan, Q. Li, *Nanoscale* **2018**, *10*, 15195.
[6] J. W. Liu, J. L. Wang, W. R. Huang, L. Yu, X. F. Ren, W. C. Wen, S. H. Yu, *Sci Rep* **2012**, *2*, 987.
[7] X. Li, H. K. Lee, I. Y. Phang, C. K. Lee, X. Y. Ling, *Anal Chem* **2014**, *86*, 10437.
[8] J. Kneipp, H. Kneipp, K. Kneipp, *Chem Soc Rev* **2008**, *37*, 1052.
[9] M. Prochazka, Surface-Enhanced Raman Spectroscopy: Bioanalytical, Biomolecular and Medical Applications. In *Surface-Enhanced Raman Spectroscopy: Bioanalytical, Biomolecular and Medical Applications*, 2016; pp 1-221.
[10] S. Abalde-Cela, P. Aldeanueva-Potel, C. Mateo-Mateo, L. Rodriguez-Lorenzo, R. A. Alvarez-Puebla, L. M. Liz-Marzan, *J R Soc Interface* **2010**, *7 Suppl 4*, S435.
[11] W. R. Premasiri, Y. Chen, J. Fore, A. Brodeur, L. D. Ziegler, Chapter 10 - SERS biomedical applications: diagnostics, forensics, and metabolomics. In *Frontiers and advances in molecular spectroscopy*, J. Laane, Ed. Elsevier: 2018; pp 327-367.
[12] W. W. Yu, I. M. White, *Anal Chem* **2010**, *82*, 9626.
[13] L. L. Qu, D. W. Li, J. Q. Xue, W. L. Zhai, J. S. Fossey, Y. T. Long, *Lab Chip* **2012**, *12*, 876.
[14] M. J. Oliveira, P. Quaresma, M. Peixoto de Almeida, A. Araujo, E. Pereira, E. Fortunato, R. Martins, R. Franco, H. Aguas, *Sci Rep* **2017**, *7*, 2480.
[15] W. Wu, L. Liu, Z. Dai, J. Liu, S. Yang, L. Zhou, X. Xiao, C. Jiang, V. A. Roy, *Sci Rep* **2015**, *5*, 10208.
[16] L. Polavarapu, A. L. Porta, S. M. Novikov, M. Coronado-Puchau, L. M. Liz-Marzan, *Small* **2014**, *10*, 3065.
[17] I. Bruzas, W. Lum, Z. Gorunmez, L. Sagle, *Analyst* **2018**, *143*, 3990.
[18] D. Cialla-May, X. S. Zheng, K. Weber, J. Popp, *Chem Soc Rev* **2017**, *46*, 3945.
[19] D. Kurouski, M. Sorci, T. Postiglione, G. Belfort, I. K. Lednev, *Biotechnol Prog* **2014**, *30*, 488.
[20] I. D. G. Macdonald, W. E. Smith, *Langmuir* **1996**, *12*, 706.
[21] X. Dou, Y. M. Jung, Z.-Q. Cao, Y. Ozak, *Appl. Spectrosc.* **1999**, *53*, 1440.
[22] M. I. Stockman, *Phys. Today* **2011**, *64*, 39.
[23] P. Matteini, M. Cottat, F. Tavanti, E. Panfilova, M. Scuderi, G. Nicotra, M. C. Menziani, N. Khlebtsov, M. de Angelis, R. Pini, *Acs Nano* **2017**, *11*, 918.
[24] B. Fazio, C. D'Andrea, A. Foti, E. Messina, A. Irrera, M. G. Donato, V. Villari, N. Micali, O. M. Marago, P. G. Gucciardi, *Sci. Rep.* **2016**, *6*.
[25] J. H. Granger, N. E. Schlotter, A. C. Crawford, M. D. Porter, *Chem Soc Rev* **2016**, *45*, 3865.
[26] H. Marks, M. Schechinger, J. Garza, A. Locke, G. Coté, *Nanophotonics* **2017**, *6*, 681.

[27] K. Kneipp, A. S. Haka, H. Kneipp, K. Badizadegan, N. Yoshizawa, C. Boone, K. E. Shafer-Peltier, J. T. Motz, R. R. Dasari, M. S. Feld, *Appl. Spectrosc.* **2002**, *56*, 150.
[28] S. A. Meyer, E. C. Le Ru, P. G. Etchegoin, *Journal of Physical Chemistry A* **2010**, *114*, 5515.
[29] N. Feliu, M. Hassan, E. G. Rico, D. X. Cui, W. Parak, R. Alvarez-Puebla, *Langmuir* **2017**, *33*, 9711.
[30] M. Banchelli, M. de Angelis, C. D'Andrea, R. Pini, P. Matteini, *Sci. Rep.* **2018**, *8*, 1033.
[31] S. Yang, X. Dai, B. B. Stogin, T. S. Wong, *Proc Natl Acad Sci U S A* **2016**, *113*, 268.
[32] P. Matteini, M. de Angelis, L. Ulivi, S. Centi, R. Pini, *Nanoscale* **2015**, *7*, 3474.
[33] F. De Angelis, F. Gentile, F. Mecarini, G. Das, M. Moretti, P. Candeloro, M. L. Coluccio, G. Cojoc, A. Accardo, C. Liberale, R. P. Zaccaria, G. Perozziello, L. Tirinato, A. Toma, G. Cuda, R. Cingolani, E. Di Fabrizio, *Nat. Photonics* **2011**, *5*, 682.
[34] W. Z. Li, W. wie, J. Y. Chen, J. X. He, S. N. Xue, J. Zhang, X. Liu, X. Li, Y. Fu, Y. H. Jiao, K. Zhang, F. Liu, E. H. Han, *Nanotechnology* **2013**, *24*, 105302.
[35] M. Chen, I. Y. Phang, M. R. Lee, J. K. Yang, X. Y. Ling, *Langmuir* **2013**, *29*, 7061.
[36] M. N'Gom, J. Ringnalda, J. F. Mansfield, A. Agarwal, N. Kotov, N. J. Zaluzec, T. B. Norris, *Nano Lett* **2008**, *8*, 3200.
[37] P. van der Wal, U. Steiner, *Soft Matt.* **2007**, *3*, 426.
[38] L.-Q. Lu, Y. Zheng, W.-G. Qu, H.-Q. Yu, A.-W. Xu, *J. Mater. Chem.* **2012**, *22*, 20986.
[39] S. Hu, K. M. Smith, T. G. Spiro, *J. Am. Chem. Soc.* **1996**, *118*, 12638.
[40] D. A. Clayton, T. E. McPherson, S. Pan, M. Chen, D. A. Dixon, D. Hu, *Phys Chem Chem Phys* **2013**, *15*, 850.
[41] S. R. Panikkanvalappil, N. Hooshmand, M. A. El-Sayed, *Bioconjug Chem* **2017**, *28*, 2452.
[42] A. R. Tao, P. Yang, *J Phys Chem B* **2005**, *109*, 15687.
[43] T. Hutter, S. R. Elliott, S. Mahajan, *Nanotechnology* **2013**, *24*, 035201.
[44] D. J. Finn, M. Lotya, J. N. Coleman, *ACS Appl Mater Interfaces* **2015**, *7*, 9254.
[45] S. Mishra, V. Yadava, *Opt. Laser Eng.* **2015**, *73*, 89.
[46] M. Malinauskas, A. Zukauskas, S. Hasegawa, Y. Hayasaki, V. Mizeikis, R. Buividas, S. Juodkazis, *Light Sci Appl* **2016**, *5*, e16133.
[47] S. Siano, R. Salimbeni, *Acc Chem Res* **2010**, *43*, 739.
[48] R. D. Deegan, O. Bakajin, T. F. Dupont, G. Huber, S. R. Nagel, T. A. Witten, *Nature* **1997**, *389*, 827.
[49] R. G. Larson, *AlChE J.* **2014**, *60*, 1538.
[50] S. Yang, B. Li, M. N. Slipchenko, A. Akkus, N. G. Singer, Y. N. Yeni, O. Akkus, *J Raman Spectrosc* **2013**, *44*, 1089.
[51] K. Wongravee, H. Gatemala, C. Thammacharoen, S. Ekgasit, S. Vantasin, I. Tanabe, Y. Ozaki, *RSC Adv.* **2015**, *5*, 1391.
[52] L. Zhang, C. Guan, Y. Wang, J. Liao, *Nanoscale* **2016**, *8*, 5928.
[53] W. Huttner, K. Christou, A. Gohmann, V. Beushausen, H. Wackerbarth, *Microfluid. Nanofluid.* **2011**, *12*, 521.
[54] X. X. Han, H. Y. Jia, Y. F. Wang, Z. C. Lu, C. X. Wang, W. Q. Xu, B. Zhao, Y. Ozaki, *Anal Chem* **2008**, *80*, 2799.
[55] E. S. Grabbe, R. P. Buck, *J. Am. Chem. Soc.* **1989**, *111*, 8362.
[56] X. Gu, Y. Yan, G. Jiang, J. Adkins, J. Shi, G. Jiang, S. Tian, *Anal. Bioanal. Chem.* **2014**, *406*, 1885.
[57] F. Chiti, C. M. Dobson, *Annu Rev Biochem* **2017**, *86*, 27.

[58] R. Buividas, N. Dzingelevicius, R. Kubiliute, P. R. Stoddart, T. Vi Khanh, E. P. Ivanova, S. Juodkazis, *Journal of Biophotonics* **2015**, *8*, 567.
[59] V. Voiciuk, G. Valincius, R. Budvytyte, A. Matijoska, I. Matulaitiene, G. Niaura, *Spectrochim Acta A Mol Biomol Spectrosc* **2012**, *95*, 526.
[60] D. Bhowmik, K. R. Mote, C. M. MacLaughlin, N. Biswas, B. Chandra, J. K. Basu, G. C. Walker, P. K. Madhu, S. Maiti, *Acs Nano* **2015**, *9*, 9070.
[61] Y. Kim, J. H. Park, H. Lee, J. M. Nam, *Sci Rep* **2016**, *6*, 19548.
[62] C. D'Andrea, A. Foti, M. Cottat, M. Banchelli, C. Capitini, F. Barreca, C. Canale, M. de Angelis, A. Relini, O. M. Marago, R. Pini, F. Chiti, P. G. Gucciardi, P. Matteini, *Small* **2018**, *14*, e1800890.
[63] A. R. A. Ladiwala, J. Litt, R. S. Kane, D. S. Aucoin, S. O. Smith, S. Ranjan, J. Davis, W. E. Van Nostrand, P. M. Tessier, *J. Biol. Chem.* **2012**, *287*, 24765.
[64] Gen, M.S.; Chan, C.K. Electrospray surface-enhanced Raman spectroscopy (ES-SERS) for probing surface chemical compositions of atmospherically relevant particles. *Atmos. Chem. Phys.* **2017**, *17*, 14025–14037, doi:10.5194/acp-17-14025-2017.
[65] Benedetti, D.P.; Zhang, J.; Tague, T.J.; Lombardi, J.R.; Leona, M. In situ microanalysis of organic colorants by inkjet colloid deposition surface-enhanced Raman scattering. *J. Raman Spectrosc.* **2014**, *45*, 123–127, doi:10.1002/jrs.4424.
[66] Fang, H.; Zhang, X.; Zhang, S.J.; Liu, L.; Zhao, Y.M.; Xu, H.J. Ultrasensitive and quantitative detection of paraquat on fruits skins via surface-enhanced Raman spectroscopy. *Sens. Actuators B—Chem.* **2015**, *213*, 452–456, doi:10.1016/j.snb.2015.02.121.
[67] Han, D.L.; Li, B.X.; Chen, Y.; Wu, T.; Kou, Y.C.; Xue, X.J.; Chen, L.; Liu, Y.; Duan, Q. Facile synthesis of Fe3O4@Au core-shell nanocomposite as a recyclable magnetic surface enhanced Raman scattering substrate for thiram detection. *Nanotechnology* **2019**, *30*, 465703, doi:10.1088/1361-6528/ab3a84.
[68] Brayner, R.; Iglesias, R.; Truong, S.; Beji, Z.; Felidj, N.; Fievet, F.; Aubard, J. Surface-enhanced raman scattering on silver nanostructured films prepared by spray-deposition. *Langmuir* **2010**, *26*, 17465–17469, doi:10.1021/la102722v.
[69] Li, B.W.; Zhang, W.; Chen, L.X.; Lin, B.C. A fast and low-cost spray method for prototyping and depositing surface-enhanced Raman scattering arrays on microfluidic paper based device. *Electrophoresis* **2013**, *34*, 2162–2168, doi:10.1002/elps.201300138.
[70] Demirta, O.; Doganay, D.; Ozturk, I.M.; Unalan, H.E.; Bek, A. Facile preparation of nanoparticle based SERS substrates for trace molecule detection. *Phys. Chem. Chem. Phys.* **2020**, *22*, 21139–21146, doi:10.1039/d0cp01866j.
[71] Yang, G.H.; Fang, X.J.; Jia, Q.; Gu, H.X.; Li, Y.P.; Han, C.Q.; Qu, L.L. Fabrication of paper-based SERS substrates by spraying silver and gold nanoparticles for SERS determination of malachite green, methylene blue, and crystal violet in fish. *Microchim. Acta* **2020**, *187*, 1–10, doi:10.1007/s00604-020-04262-2.
[72] Jang, W.; Byun, H.; Kim, J.H. Rapid preparation of paper-based plasmonic platforms for SERS applications. *Mater. Chem. Phys.* **2020**, *240*, 122124, doi:10.1016/j.matchemphys.2019.122124.
[73] Zhou, Y.Z.; Cheng, X.N.; Du, D.; Yang, J.; Zhao, N.; Ma, S.B.; Zhong, T.; Lin, Y.H. Graphene-silver nanohybrids for ultrasensitive surface enhanced Raman spectroscopy: Size dependence of silver nanoparticles. *J. Mater. Chem. C* **2014**, *2*, 6850–6858, doi:10.1039/c4tc00658e.

[74] Zhou, Y.Z.; Cheng, X.N.; Yang, J.; Zhao, N.; Ma, S.B.; Li, D.; Zhong, T. Fast and green synthesis of flexible free-standing silver nanoparticles-graphene substrates and their surface-enhanced Raman scattering activity. *RSC Adv.* **2013**, *3*, 23236–23241, doi:10.1039/c3ra43400a.
[75] Liu, J.; Liu, L.B.; Wu, X.W.; Zhang, X.K.; Li, T.D. Environmentally friendly synthesis of graphene-silver composites with surface-enhanced Raman scattering and antibacterial activity via reduction with L-ascorbic acid/water vapor. *N. J. Chem.* **2015**, *39*, 5272–5281, doi:10.1039/c5nj00414d.
[76] Li, Y.T.; Qu, L.L.; Li, D.W.; Song, Q.X.; Fathi, F.; Long, Y.T. Rapid and sensitive in-situ detection of polar antibiotics in water using a disposable Ag-graphene sensor based on electrophoretic preconcentration and surface-enhanced Raman spectroscopy. *Biosens. Bioelectron.* **2013**, *43*, 94–100, doi:10.1016/j.bios.2012.12.005.
[77] Liu, M.M.; Chen, W. Graphene nanosheets-supported Ag nanoparticles for ultrasensitive detection of TNT by surface-enhanced Raman spectroscopy. *Biosens. Bioelectron.* **2013**, *46*, 68–73, doi:10.1016/j.bios.2013.01.073.
[78] Waxenegger, J.; Trugler, A.; Hohenester, U. Plasmonics simulations with the MNPBEM toolbox: Consideration of substrates and layer structures. *Comput. Phys. Commun.* **2015**, *193*, 138–150, doi:10.1016/j.cpc.2015.03.023.
[79] Rakic, A.D.; Djurisic, A.B.; Elazar, J.M.; Majewski, M.L. Optical properties of metallic films for vertical-cavity optoelectronic devices. *Appl. Opt.* **1998**, *37*, 5271–5283, doi:10.1364/ao.37.005271.
[80] Zhu, Y.W.; Murali, S.; Cai, W.W.; Li, X.S.; Suk, J.W.; Potts, J.R.; Ruoff, R.S. Graphene and graphene oxide: Synthesis, properties, and applications. *Adv. Mater.* **2010**, *22*, 3906–3924, doi:10.1002/adma.201001068.
[81] Novotny, L. Effective wavelength scaling for optical antennas. *Phys. Rev. Lett.* **2007**, *98*, 266802, doi:10.1103/PhysRevLett.98.266802.
[82] Rossouw, D.; Botton, G.A. Plasmonic response of bent silver nanowires for nanophotonic subwavelength waveguiding. *Phys. Rev. Lett.* **2013**, *110*, 066801, doi:10.1103/PhysRevLett.110.066801.
[83] Banchelli, M.; Amicucci, C.; Ruggiero, E.; D'Andrea, C.; Cottat, M.; Ciofini, D.; Osticioli, I.; Ghini, G.; Siano, S.; Pini, R.; et al. Spot-on SERS detection of biomolecules with laser-patterned dot arrays of assembled silver nanowires. ChemNanoMat 2019, 5, 1036–1043, doi:10.1002/cnma.201900035.
[84] Barucci, A.; D'Andrea, C.; Farnesi, E.; Banchelli, M.; Amicucci, C.; De Angelis, M.; Hwang, B.; Matteini, P. Label-free SERS detection of proteins based on machine learning classification of chemo-structural determinants. Analyst 2021, 146, 674–682, doi:10.1039/d0an02137g.
[85] Banchelli, M.; Cascella, R.; D'Andrea, C.; Cabaj, L.; Osticioli, I.; Ciofini, D.; Li, M.S.; Skupien, K.; De Angelis, M.; Siano, S.; et al. Nanoscopic insights into the surface conformation of neurotoxic amyloid beta oligomers. RSC Adv. 2020, 10, 21907–21913, doi:10.1039/d0ra03799k.
[86] Kwon, J.; Suh, Y.D.; Lee, J.; Lee, P.; Han, S.; Hong, S.; Yeo, J.; Lee, H.; Ko, S.H. Recent progress in silver nanowire based flexible/wearable optoelectronics. J. Mater. Chem. C 2018, 6, 7445–7461, doi:10.1039/c8tc01024b.
[87] Wu, W.; Liu, L.; Dai, Z.G.; Liu, J.H.; Yang, S.L.; Zhou, L.; Xiao, X.H.; Jiang, C.Z.; Roy, V.A.L. Low-cost, disposable, flexible and highly reproducible screen printed sers substrates for the detection of various chemicals. Sci. Rep. 2015, 5, doi:10.1038/srep10208.

[88] Yu, W.W.; White, I.M. A simple filter-based approach to surface enhanced Raman spectroscopy for trace chemical detection. Analyst 2012, 137, 1168–1173, doi:10.1039/c2an15947c.
[89] Shi, Y.E.; Li, L.M.; Yang, M.; Jiang, X.H.; Zhao, Q.Q.; Zhan, J.H. A disordered silver nanowires membrane for extraction and surface-enhanced Raman spectroscopy detection. Analyst 2014, 139, 2525–2530, doi:10.1039/c4an00163j.
[90] Wang, Q.; Zhao, X.C.; Yu, Z.N.; Tan, R.Q.; Lan, J. Large scale preparation of surface enhanced Raman spectroscopy substrates based on silver nanowires for trace chemical detection. Anal. Methods 2015, 7, 10359–10363, doi:10.1039/c5ay02790j.
[91] Tao, A.R.; Yang, P.D. Polarized surface-enhanced Raman spectroscopy on coupled metallic nanowires. J. Phys. Chem. B 2005, 109, 15687–15690, doi:10.1021/jp053353z.
[92] Jang, S.; Lee, J.; Nam, S.; Ko, H.; Chang, S.T. Large-area, highly sensitive SERS substrates with silver nanowire thin films coated by microliter-scale solution process. Nanoscale Res. Lett. 2017, 12, 581.
[93] Lai, H.S.; Xu, F.G.; Zhang, Y.; Wang, L. Recent progress on graphene-based substrates for surface-enhanced Raman scattering applications. J. Mater. Chem. B 2018, 6, 4008–4028, doi:10.1039/c8tb00902c.
[94] Heck, C.; Kanehira, Y.; Kneipp, J.; Bald, I. Amorphous carbon generation as a photocatalytic reaction on DNA-assembled gold and silver nanostructures. Molecules 2019, 24, 2324, doi:10.3390/molecules24122324.
[95] Zheng, P.; Wu, N.Q. Fluorescence and sensing applications of graphene oxide and graphene quantum dots: A review. Chem. -Asian J. 2017, 12, 2343–2353, doi:10.1002/asia.201700814.
[96] Xu, L.J.; Zong, C.; Zheng, X.S.; Hu, P.; Feng, J.M.; Ren, B. Label-free detection of native proteins by surface-enhanced Raman spectroscopy using iodide-modified nanoparticles. Anal. Chem. 2014, 86, 2238–2245, doi:10.1021/ac403974n.
[97] Kahraman, M.; Balz, B.N.; Wachsmann-Hogiu, S. Hydrophobicity-driven self-assembly of protein and silver nanoparticles for protein detection using surface-enhanced Raman scattering. Analyst 2013, 138, 2906–2913, doi:10.1039/c3an00025g.

Chapter 6: SERS detection of flavonoids in plant extracts

1. Introduction

Flavonoids are natural compounds widely present in the plant world, representing a large class of phenolic compounds comprising more than 6,000 different species. They are able to exert various biological activities that are very useful for the human body, which justifies the importance they have assumed for human health currently attributed to these compounds. Among the properties attributed to flavonoids that arouse greater interest, should be mentioned the antioxidant [1] and the anti-inflammatory actions.[2] In the field of medical-pharmaceutical research, the interest is focused on the potential anticancer properties[3] and the preventive / beneficial role that these compounds are able to exert in the presence of different diseases such as Alzheimer's disease, atherosclerosis, etc.[1,4-5] They are also known to be powerful inhibitors of several enzymes, such as xanthine oxidase inhibitors, which are important for the therapeutic treatment of gout; cyclo-oxygenase inhibitors, which are used to treat pain after surgery, have been found to be effective in suppressing inflammatory neurodegenerative pathways in mental illness and have been shown to reduce the occurrence of cancers and pre-cancerous growths; and phosphoinositide 3-kinase, which is used in cancer treatment.[6-8] In Figure 1 a general representation of the roles provided by flavonoids in various bioactivities, human health and agriculture fields is reported.

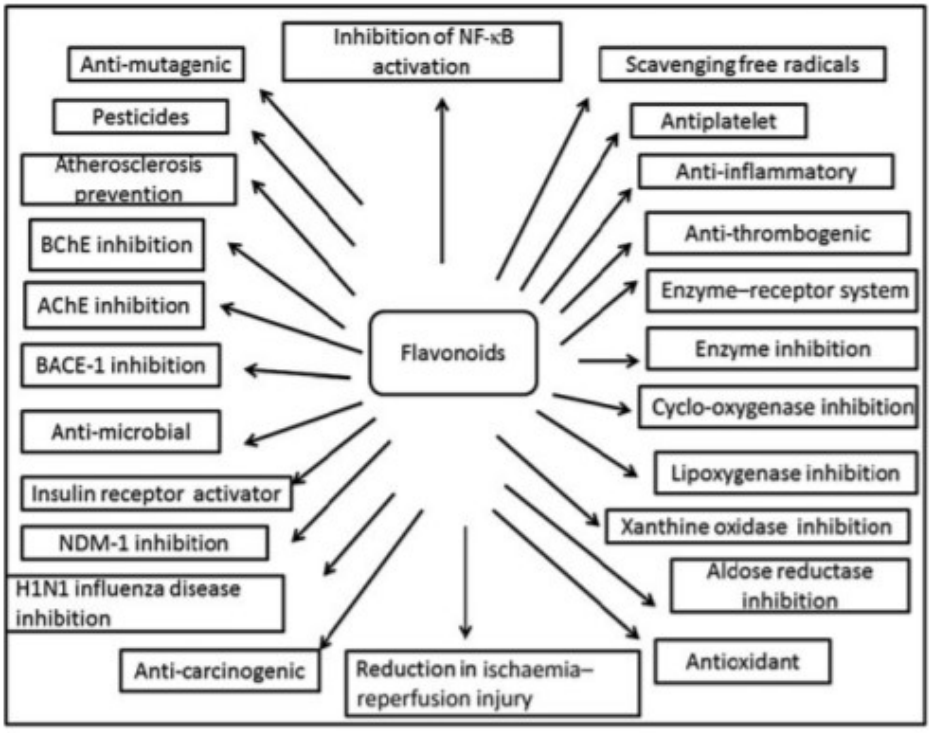

Figure 1. Cumulative representation of roles of flavonoids in various bioactivities, human health and agriculture. (BChE, butyrylcholinesterase; AChE, acetylcholinesterase; BACE-1, β active site cleavage enzyme-1; NDM-1, New Delhi metallo-β-lactamase-1; H1N1, haemagglutinin 1 neuraminidase 1). ***[9]***

Flavonoids can be subdivided into different subgroups depending on their chemical structure: flavones, flavonols, chalcones, anthocyanins, flavones and isoflavonoids (see Figure 2).

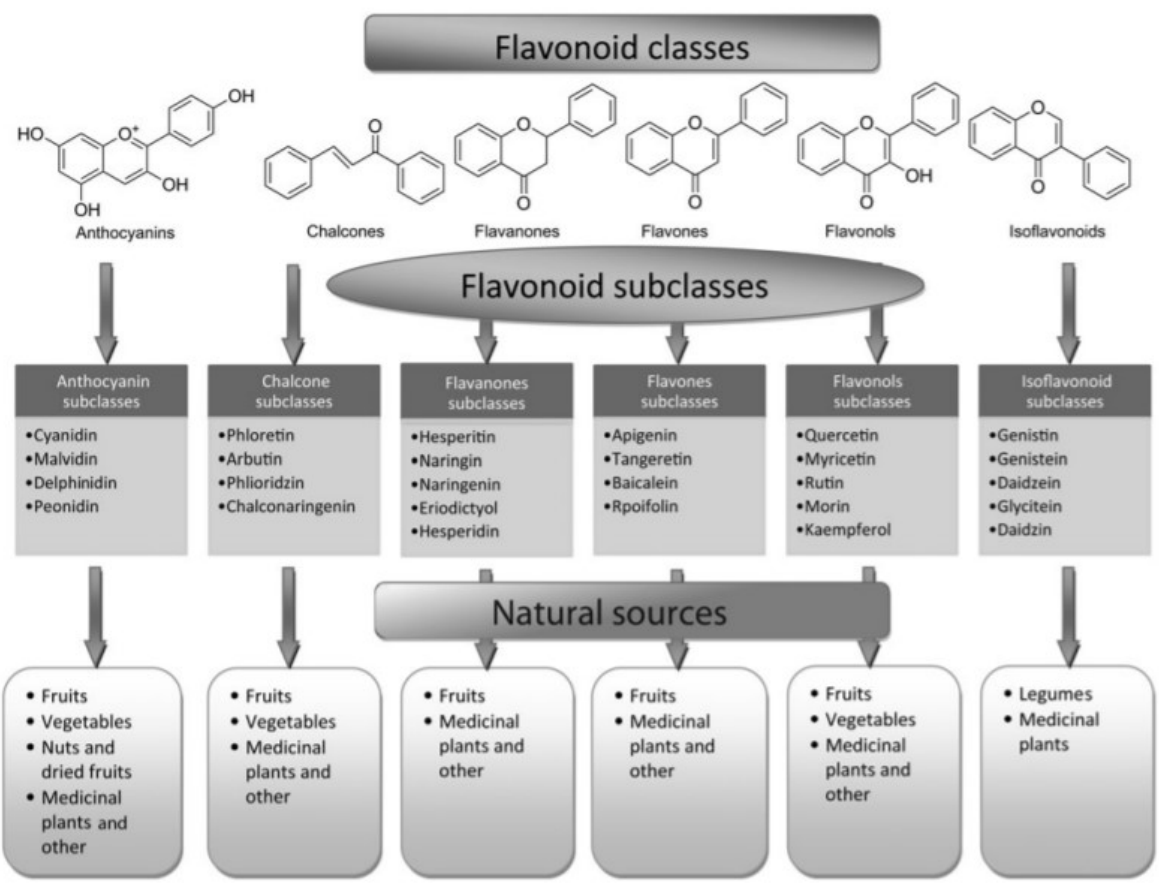

*Figure 2. Flavonoid classes, subclasses and natural sources.**[9]***

Parallel to the importance that flavonoids acquire in the pharmaceutical, nutraceutical industry, etc., exploring new analytical techniques for their determination is gaining progressive interest. Different traditional methods like UV/Visible absorption spectroscopy and separation techniques like thin-layer chromatography (TLC), paper electrophoresis and polyamide chromatography were used in the past for flavonoid separation. Overall, TLC is a preferred method for flavonoid analysis, because of its simplicity, rapidity and versatility. The majority of recently published work is instead mainly focused on qualitative and quantitative determination of flavonoids by high-performance liquid chromatography (HPLC), liquid chromatography-mass spectrometry (LC-MS), liquid chromatography-nuclear magnetic resonance (LC-NMR) and capillary electrophoresis (CE). The separation, identification and quantification of flavonoids can be performed in a single step by pairing HPLC to UV/Vis, MS or NMR detectors, especially if the study aims at determining specific flavonoids. These factors have contributed to make HPLC analysis of flavonoids a commonly used technique nowadays. On the other hand, few Raman and SERS studies were devoted to the detection of flavonoids so far. [10-13]

Jurasekova et al. reported for the first time the SERS spectra of a subgroup of flavonoids.[12]

On the basis of previous findings, [12-15] in this Chapter is presented the work we carried out to explore the possibility to use SERS for rapid determination of the flavonoid content in plant extracts. Specifically, by taking advantage of the SERS substrates already developed (cf. Chapter 5), we were aimed at determining the presence of apigenin, luteolin, kaempferol and quercetin in chamomile extracts.

2. Results and Discussion

The aim of this work was carried out a SERS analysis of flavonoid species slightly differing in structure and establish a correlation between their structural properties and spectral response. This may prove propaedeutic in view of future studies based on the SERS analysis of different flavonoids in plant samples. The possibility to identify specific peaks for each species is fundamental to develop an effective method for flavonoid determination in biological extracts, which can exploit the high sensitivity, non-destructiveness, low cost and rapidity of SERS. The flavonoids selected for this study were: apigenin (APG), luteolin (LUT), kaempferol (KMP) and quercetin (QUC) and their structure are displayed in Figure 3 along with the indication of the aromatic rings displayed in Figure 4.

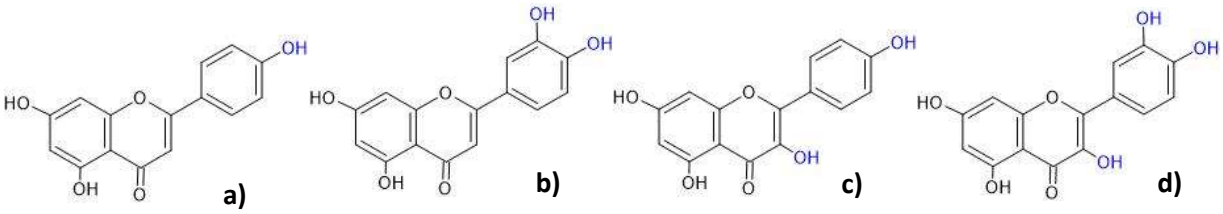

Figure 3. Structures of: a) apigenin; b) luteolin; c) kaempferol; d) quercetin.

UV-Vis, Raman and SERS spectra of the flavonoids were initially collected as reported below.

2.1 UV-Vis Characterization

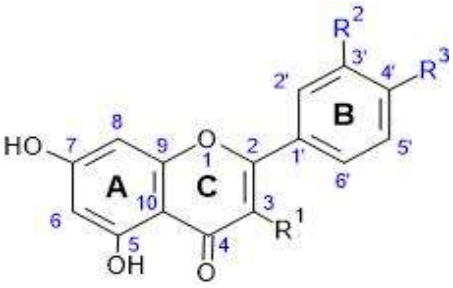

APG: R^1=H; R^2=H; R^3=OH
QUC: R^1=OH; R^2=OH; R^3=OH
LUT: R^1=H; R^2=OH; R^3=OH
KMP: R^1=OH; R^2=H; R^3=OH

Figure 4. Schematic representation of the flavonoids considered in this study with indication of A-, B- and C-rings.

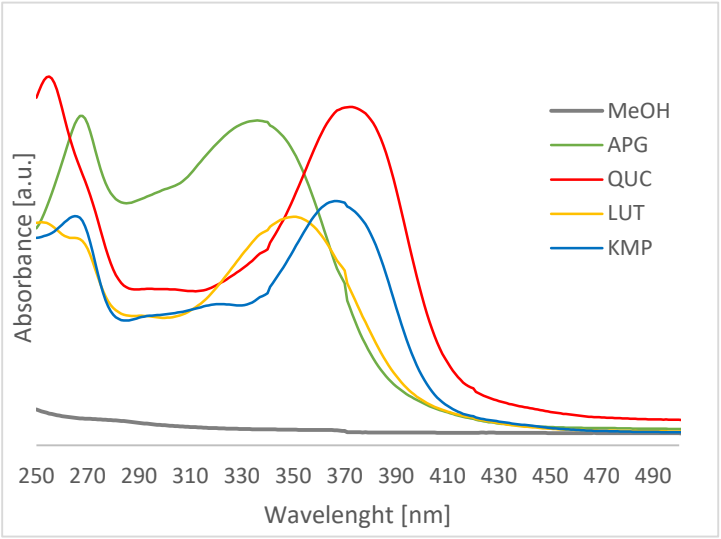

Figure 5. UV-Vis spectra of apigenin, luteolin, kaempferol and quercetin solutions in methanol (MeOH). The spectrum of MeOH is also reported as control.

The UV-Vis spectra (Figure 5) show two main absorption bands: 300-400 nm (Band I) ascribed to the **B**-ring absorption, and 250-285 nm (Band II) relative to the **A**-ring absorption. By comparing the different flavonoid structures we can deduce which OH position has the higher influence on Band I. APG shows an unshifted peak, according to the most simple structure (only one OH in C(4')), LUT is characterized by a little red shift ascribed to the additional hydroxyl group in position C(3'), KMP shows a higher red shift ascribed to the hydroxyl group in position C(3), while an additional OH in C(3') seems to induce minor changes in the UV-vis spectrum.

2.2 Raman Characterization

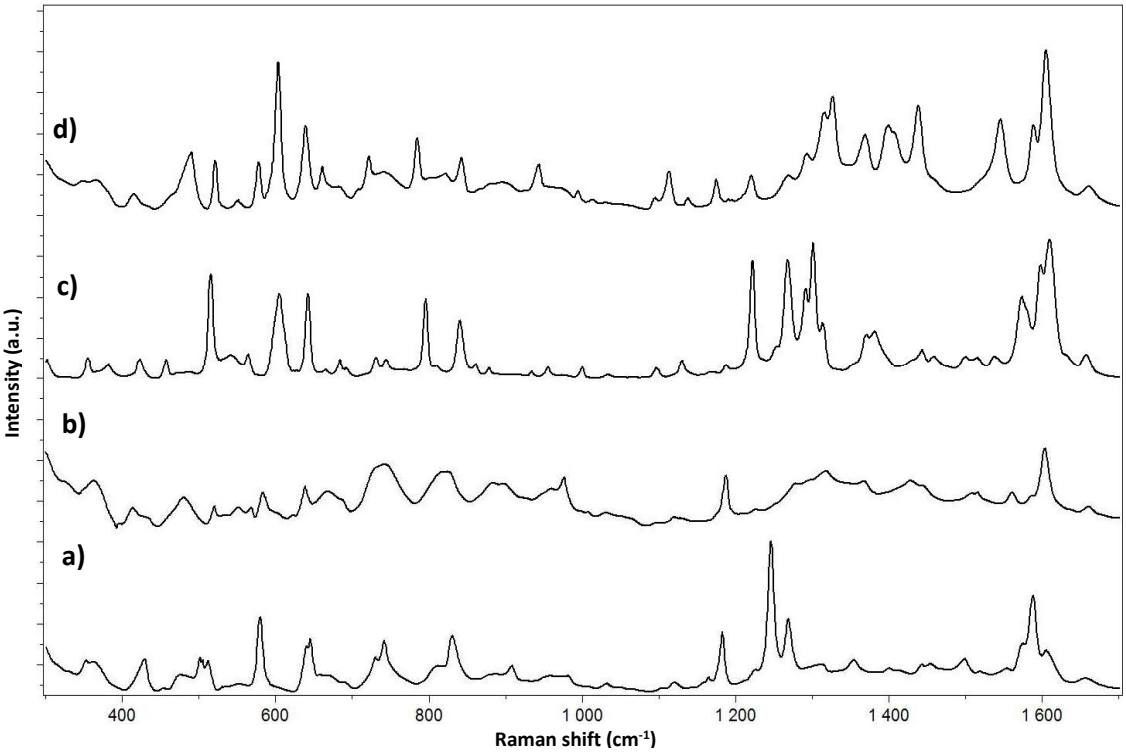

Figure 6: Raman spectra of powder samples of a) apigenin; b) kaempferol; c) luteolin and d) quercetin.

Raman analysis were directly performed on powdered flavonoids (Figure 6). The Raman spectra show some bands that are common to all the studied flavonoids: ~1187 cm^{-1}, ~1270 cm^{-1}, ~1315 cm^{-1}, ~1605 cm^{-1}, 1657 cm^{-1}.[15] In the 1000-1400 cm^{-1} spectral region we can observe the main differences among the flavonoid species as a function of the number and position of their OH groups. For example in the APG spectrum there are fewer bands in this region in accordance with a structure containing the least number of OH groups, and specifically at 1352 cm^{-1}, 1314 cm^{-1}, 1270 cm^{-1}, 1247 cm^{-1}, 1185 cm^{-1}. The Raman peaks of LUT are: 1380 cm^{-1}, 1369 cm^{-1}, 1354 cm^{-1}, 1314 cm^{-1}, 1300 cm^{-1}, 1292 cm^{-1}, 1268 cm^{-1}, 1250 cm^{-1}, 1222 cm^{-1}, 1187 cm^{-1}. In this case we can observe little band shifts and change in intensity of the same peaks, as already observed in the APG Raman spectrum, as well as the presence of some additional peaks (1369 cm^{-1}, 1292 cm^{-1}), which we can ascribe to the hydroxyl group in C(3') position. The Raman bands of QUC are: 1397 cm^{-1}, 1368 cm^{-1}, 1326 cm^{-1}, 1314 cm^{-1}, 1292 cm^{-1}, 1269 cm^{-1}, 1220 cm^{-1} , 1190 cm^{-1}, 1174 cm^{-1}, 1136 cm^{-1}, 1114 cm^{-1}, 1094 cm^{-1}. The QUC spectrum is characterized by some shifted peaks already found in the spectra of LUT and APG, along with some new peaks (1326 cm^{-1}, 1114 cm^{-1}), which we ascribe to the hydroxyl group in position C(3) as supported by their identification at same or slightly shifted frequencies in the Raman profile of KMP (1326 cm^{-1}, 1318 cm^{-1}, 1273 cm^{-1}, 1223 cm^{-1}, 1187 cm^{-1}, 1117 cm^{-1}).

2.3 SERS characterization

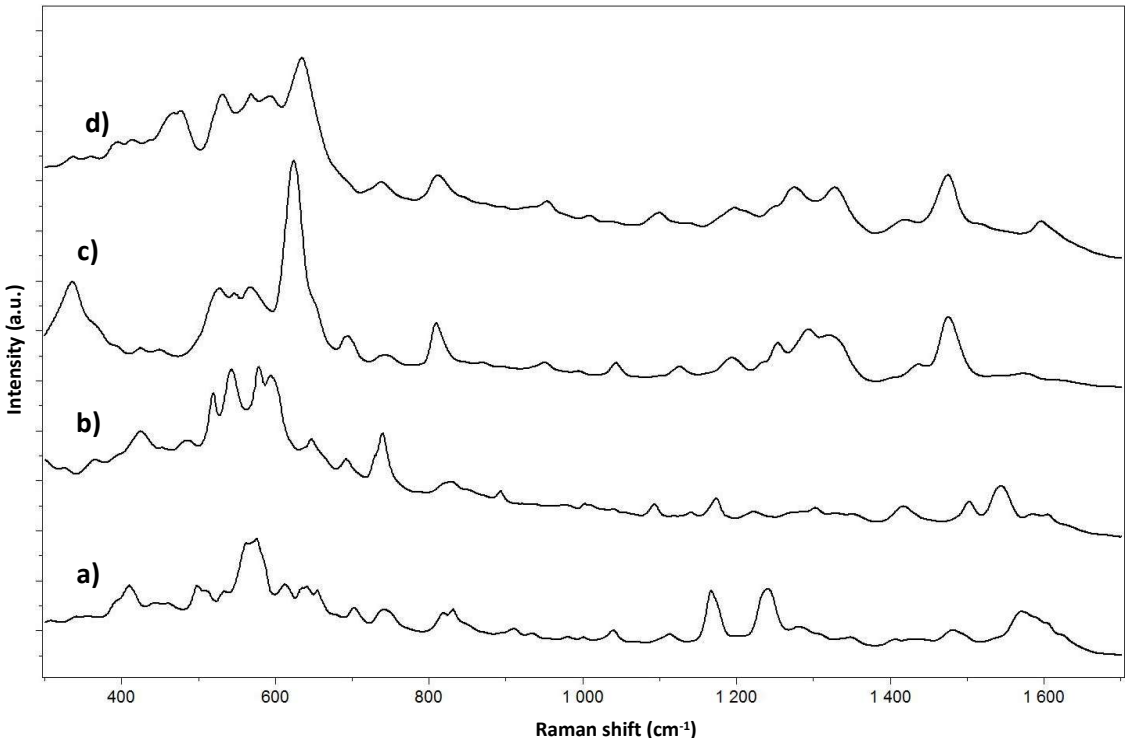

Figure 7. SERS spectra of water solutions (10^{-5} M) of: a) apigenin; b) kaempferol; c) luteolin and d) quercetin.

SERS spectra (Figure 7) show large differences both in intensities and Raman shift among the flavonoid species considered, and just one common band that is present in all the spectra (at ~740 cm^{-1}), which can be ascribed to ring C-C in-plane deformations.[14] Characteristic SERS peaks for each flavonoid can be identified as follows: APG (931 cm^{-1}, 1166 cm^{-1}, 1241 cm^{-1}), LUT (623 cm^{-1}, 808 cm^{-1}, 1191 cm^{-1}), KMP (422 cm^{-1}, 892 cm^{-1}), QUC (633 cm^{-1}, 811 cm^{-1}, 1274 cm^{-1}, 1329 cm^{-1}). These SERS bands can be used to unequivocally identify each flavonoid species. Concerning the region around 630 cm^{-1}, we can observe a very strong band for LUT (623 cm^{-1}) and QUC (633 cm^{-1}), which could suggest us a preferential orientation of these species on the Ag surface through the catechol moiety (Figure 8). On the other hand, we observe a common band in the region ~1170 cm^{-1} in both KMP and APG spectra: KMP (1174 cm^{-1}); APG (1166 cm^{-1}), which suggests a possible similar orientation of these species, which could interact with Ag through the OH group in C(4') (Figure 8).

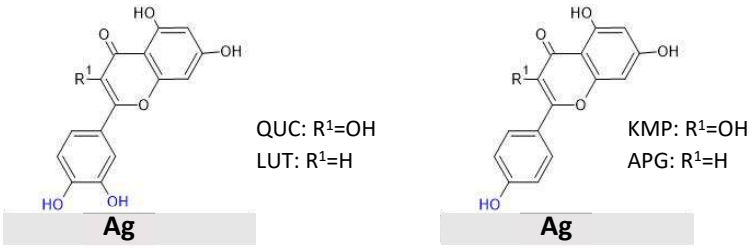

Figure 8. Schematic representation of possible interactions between flavonoids and SERS substrate.

2.4 SERS analysis of chamomile

Chamomile (*Matricaria recutita L.)* is a medicinal plant often used for its analgesic, anti-allergic, anti-spasmodic, antibacterial, anti-inflammatory and sedative properties. Its essential oil containing volatile compounds including terpenoids such as azulene, chamazulene and -bisabolol is the most commonly used.[17] Recently, much attention has been paid to the non-volatile fraction of chamomile extracts, containing phenolic compounds exerting spasmolytic and antiphlogistic activity [18] as well as antioxidant activity. The main responsible of the antioxidant activity are the flavonoid species considered above (APG, LUT, KMP, QUC). The phenolic fraction of Chamomile might further contain phenolic acids (chlorogenic acid, caffeic acid) and coumarins (umbelliferone). Chamomile flowers were obtained from the herbalist shop and a five-day methanolic extraction was performed according to the protocol of Nováková et al..[16] SERS spectra were then collected from the methanolic extract (once diluted 1:100 with water). Through a comparison of the SERS spectrum of chamomile *vs* those of isolated flavonoids, we can identify some characteristic bands of APG, LUT, KMP and QUC, which can confirm their presence in the extracts. Specifically these are 1166 cm^{-1} for apigenin; 808 cm^{-1} for luteolin; 422 cm^{-1} for kaempferol and 633 cm^{-1}, 1274 cm^{-1}; 1329 cm^{-1} for quercetin.

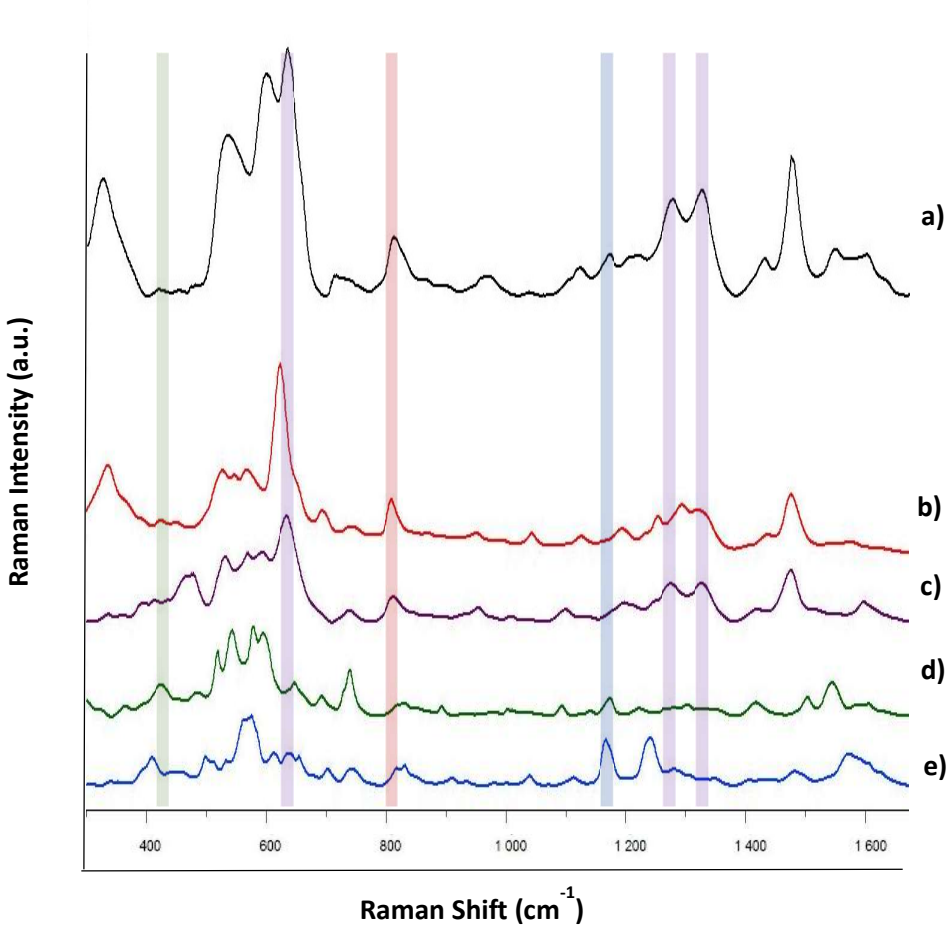

Figure 9. SERS spectra of: a) chamomile extract. Spectra of b) luteolin; c) quercetin; d) kaempferol; e) apigenin are also reported as references.

3. Conclusions

In this study we were aimed at identifying different flavonoid species in plant extracts by SERS analysis. To achieve this goal, we exploited a previously developed SERS substrate to collect reference SERS spectra of four commonly found flavonoids: apigenin, luteolin, kaempferol, and quercetin. Finally, we were able to obtain an intense SERS profile from chamomile extract and successfully inspected it for the presence of these flavonoids. Nowadays HPLC represents the main analytical strategy for qualitative and quantitative determination of flavonoids in plant extracts. Nonetheless SERS can become an alternative or complementary technique, overcoming some limits of HPLC, which is time-consuming and expensive. We are now focusing on quantitative aspects aimed at finding the linear concentration range for each flavonoid standard. The method can be proposed for quasi real-time analysis of plant extracts by the use of portable or benchtop spectrometers, making it easier to monitor flavonoids in plants for the nutraceutical industry.

4. Experimental Section

4.1 Materials and extraction procedure

Apigenin, luteolin, quercetin and kaempferol were purchased from Extrasynthèse. Methanol was obtained from Sigma-Aldrich (ACS reagent, ≥99.8%). Chamomile flowers were purchased from Erboristeria Secciani (Florence). The methanolic extracts were obtained by following the protocol of Nováková et al..[16]

4.2 UV-Vis measurements

UV-Vis characterization was performed by a UV-Vis spectrophotometer (PerkinElmer Lambda 35 UV/ Vis). The spectra were obtained by dilution of initial stock solutions in MeOH in order to obtain Absorbance values included in a range between 0.4 and 0.8.

4.3 Raman and SERS measurements

Raman analysis was performed under a micro-Raman spectrometer (XPlora, Horiba) directly on the flavonoid powder, working at 785 nm excitation line with a 1200 grooves/mm grating, a 10x objective, 15 mW laser power and 5s integration time. SERS spectra were obtained by pouring 5µL of each flavonoid (at 10^{-5} M) onto single spots of AgNWs@PTFE substrates as developed in Chapter 5 and let to dry. SERS analysis was performed as for Raman measurements. In this case a laser power of 598 µW and an integration time of 2 s were employed. Raman and SERS data were baseline corrected and represent an average of 20 spectra collected by mapping experiments over 12 mm^2 areas within the sample (powder for Raman or Ag spot for SERS).

Raman				SERS			
APG	LUT	KMP	QUC	APG	LUT	KMP	QUC
427 *w*	514 vs	415 vs	415 w	408 vs	423 w	478 vs	413 w
501 *w*	604 vs	519 vs	488 vs	442 s	525 vs	490 vs	531 vs
578 s	641 vs	532 s	520 s	533 vs	543 vs	518 vs	569 vs
644 m	683 w	549 vs	549 vw	574 vs	565 vs	541 vs	592 vs
740 m	730 w	582 vs	578 s	611 vs	623 vs	578 vs	633 vs
829 m	744 w	621 w	602 vs	641 vs	692 m	595 vs	737 w
908 w	766 vw	637 vs	638 vs	654 vs	741 w	646 vs	811 w
1120 vw	795 vs	669 s	660 m	702 s	776 w	691 m	1100 w
1185 m	809 w	743 vs	684 w	739 s	808 m	739 vs	1197 w
1247 vs	839 vw	820 vs	721 s	816 s	948 w	827 m	1274 s
1270 s	859 w	884 vs	741 m	830 s	1043 w	892 m	1329 s
1314**w**	877 vw	901 vs	784 vs	873 s	1191 w	1091 m	1416 w
1352 w	955 vw	928 s	823 m	910 s	1254 m	1174 m	1475 vs
1498 w	1000 vw	960 vs	841 s	931 s	1292 m	1302 m	1514 w
1588 s	1032 vw	1005 m	941 s	957 s	1317 m	1416 m	1597 w
1605 **m**	1096 vw	1031 m	994 w	979 s	1474 s	1503 s	
1655 vw	1130 w	1083 vw	1013 vw	998 s		1544 s	
	1164 vw	1084 vw	1094 vw	1037 s		1585 m	
	1187 w	1118 w	1113 m	1114 s		1602 m	
	1222 vs	1187 vs	1136 vw	1166 vs			
	1250	1223 vw	1174 m	1241 vs			
	1268 vs	1276 s	1190 vw	1276 s			
	1300 vs	1318 vs	1220 m	1347 s			
	1380 s	1442 m	1292 s				
	1442 m	1559 m	1314 vs				
	1513 w	1602 vs	1326 vs				
	1572 vs	1659 w	1368 vs				
	1609 vs		1397 vs				
	1656 w		1437 vs				
	1572 vs		1554 vs				
	1609 vs		1588 vs				
	1656 w		1604 vs				
			1660 w				

Table 1. Main Raman and SERS signals (cm^{-1}) of apigenin (APG), luteolin (LUT), quercetin (QUC) and kampferol (KMP). Peaks were marked with *vw* (very weak: 5-10 %), *w* (weak: 10-20%), *m* (medium: 20-30%), *s* (strong: 30-40%), *vs* (very strong > 40%) as a function of their relative intensity.

Bibliography

[1] Burak M, Imen Y; Flavonoids and their antioxidant properties. Turkiye Klin Tip Bil Derg 19, 296–304 (1999)

[2] Comalada M, Camuesco D, Sierra S, et al. (2005) In vivo quercitrin anti-inflammatory effect involves release of quercetin, which inhibits inflammation through down-regulation of the NF-κB pathway. Eur J Immunol 35, 584–592

[3] Kim SH & Choi KC (2013) Anti-cancer effect and underlying mechanism(s) of kaempferol, a phytoestrogen, on the regulation of apoptosis in diverse cancer cell models. Toxicol Res 29, 229–234.

[4] Lee Y, Yuk D, Lee J, et al. (2009) Epigallocatechin-3-gallate prevents lipopolysaccharide-induced elevation of β-amyloid generation and memory deficiency. Brain Res 1250, 164–174

[5] Ovando C, Hernandez D, Hernandez E, et al. (2009) Chemical studies of anthocyanins: a review. Food Chem 113, 859–871.

[6] Metodiewa D, Kochman A & Karolczak S (1997) Evidence for antiradical and antioxidant properties of four biologically active N, N, diethylaminoethyl ethers of flavanone oximes: a comparison with natural polyphenolic flavonoid (rutin) action. Biochem Mol Biol Int 41, 1067–1075.

[7] Hayashi T, Sawa K, Kawasaki M, et al. (1988) Inhibition of cow's milk xanthine oxidase by flavonoids. J Nat Prod 51, 345–348.

[8] Walker E, Pacold M, Perisic O, et al. (2000) Structural determinations of phosphoinositide 3-kinase inhibition by wortmannin, LY294002, quercetin, myricetin, and staurosporine. Mol Cell 6, 909–919.

[9] Panche, A. N., Diwan, A. D., & Chandra, S. R. (2016). Flavonoids: an overview. Journal of Nutritional Science, 5.

[10] Torreggiani A, Trinchero A, Tamba M, Taddei P. Raman and pulse radiolysis studies of the antioxidant properties of quercetin: Cu(II) chelation and oxidizing radical scavenging. J. Raman Spectrosc. 2005; 36: 380.

[11] Cornard JP, Merlin JC. Spectroscopic and structural study of complexes of quercetin with Al(III) J. Inorg. Biochem. 2002; 92: 19

[12] Z. Jurasekova, J. V. Garcia-Ramos, C. Domingo and S. Sanchez-Cortes; Surface-enhanced Raman scattering of flavonoids J. Raman Spectrosc.2006;37: 1239 – 1241

[13] Y. Lia, C. Zhaoa , C. Lua , S. Zhou; Simultaneous determination of 14 bioactive citrus flavonoids using thinlayer chromatography combined with surface enhanced Raman spectroscopy. Food Chemistry 338 (2021) 128115

[14] C. Corredor T. Teslova Raman and surface enhanced Raman spectra of chrysin, apigenin and luteolin. J.vibspec 2009 49: 190-195

[15] Z. Jurasekova, J. V. Garcia-Ramos, C. Domingo and S. Sanchez-Cortes. In situ detection of flavonoids in weld-dyed wool and silk textiles by surface-enhanced Raman scattering. J.Raman Spectrosc. 2008; 39: 1309–1312

[16] Nováková, L. (2010). Development and application of UHPLC-MS/MS method for the determination of phenolic compounds in Chamomile flowers and Chamomile tea extracts. Talanta, 82, 1271-1280.

[17] M. Adams, C. Berset, M. Kessler, M. Hamburger, J. Ethnopharmacol. 121 (2009) 343–359.

[18] R. Franke, H. Schilcher, Chamomile Industrial Profiles, CRC Press, USA, 2005.

Chapter 7: Development of a wearable SERS chip for detection of lactic acid and urea in sweat

1. Introduction

Since the arrival of smartphones, wearable sensors have received much attention thanks to their ability to provide useful information about metabolism and health of individuals. [1–6] Early efforts in this area focused on physical sensors that monitored mobility and vital signs, such as steps, calories burned or heart rate. The face of wearable devices has changed rapidly in recent years, with researchers branching out from tracking physical exercise activity to focus on tackling major challenges in healthcare applications, such as the management of diabetes or remote monitoring of the elderly. To accomplish these goals, researchers have devoted substantial efforts to the development of wearable biosensors, which are defined as sensing devices that incorporate a biological recognition element into the sensor operation (for example, enzyme, antibody, cell receptor or organelle). The potential utility of wearable biosensors is evident from the rapidly increasing rate of newly reported proof-of-concept studies.

The analysis of biological samples, such as sweat, saliva, tears, interstitial fluid (ISF) and breath, provides diagnostic parameters of human health regarding diseases and physiological status.[7-10] A typical biosensor contains two basic functional units: a 'bioreceptor' (for example, enzyme, antibody or DNA) responsible for selective recognition of the target analyte and a physico-chemical transducer (for example, electrochemical, optical or mechanical) that translates this biorecognition event into a useful signal (Figure 1a). Such devices were initially developed for in vitro measurements in controlled (laboratory or point-of-care) settings or for single-use home testing (for example, blood glucose test strips). A brief history of biosensing technologies preceding current wearable is provided in Figure 1b. These past advances have paved the way to modern wearable biosensors for noninvasive biomonitoring applications as an alternative to blood monitoring biomedical devices in connection to a wide range of healthcare applications.

As the epidermis covers most of our body, skin-worn conformal devices have received the greatest recent attention among the various types of wearable biosensors. Epidermal biosensors can facilitate real-time analysis of biomarkers in epidermal biofluids such as sweat and, with some systems exhibiting continuous monitoring capabilities toward a variety of biomedical and fitness applications. These devices rely on sweat or ISF sampling at the skin surface, along with transport of these biofluids over the biosensor surface. Such skin-worn biosensors commonly rely on different transduction modes (for example, optical, electrochemical and mechanical) in combination with biocatalytic and ion-recognition receptors. Further integration with data processing and transmission components are necessary for a fully wearable platform. The majority of recent reports, however, have focused on electrochemical and colorimetric transduction methodologies. Major progress has been made toward a variety of skin-worn platforms offering the capability to readily sample epidermal biofluids with

wearer comfort [12-23]. Such devices have been realized through direct transfer of sensors onto the skin (using E-skin or printed temporary tattoos), by sensor incorporation into wristbands and patches, or by embedding sensors directly into textiles to ensure tight contact with the skin while allowing the sensors to endure the mechanical stresses encountered during body movements.

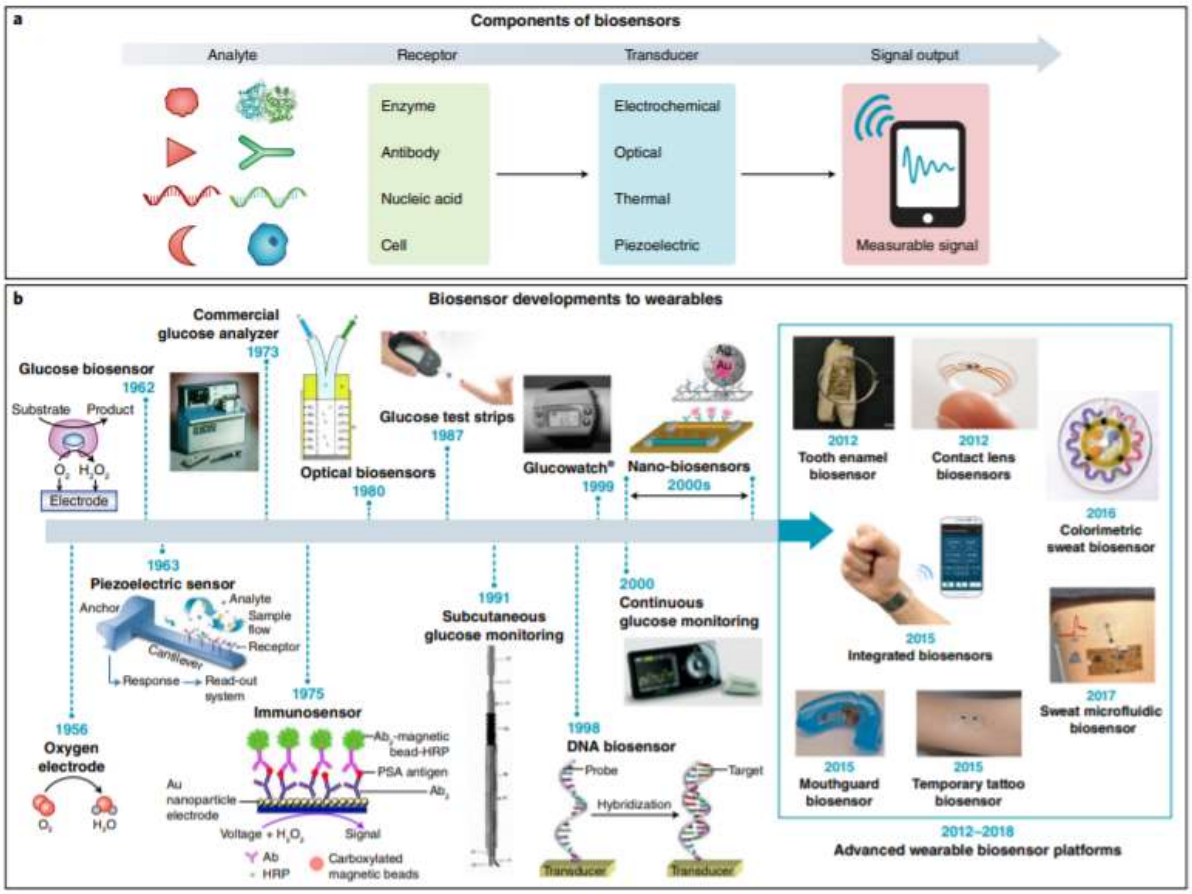

Figure 1. Biosensor components and development path for wearable biosensors. a) Schematic representation of biosensor operation principles; b) biosensor evolution from 1956 to 2018. [11]

The goal of this Chapter is to develop a wearable SERS chip for label-free detection of lactic acid and urea in sweat. Sweat is the most readily obtainable biofluid for chemical sensing applications since sweat glands are distributed across the entire body, with more than 100 glands/cm^2 of skin.[11] This physiology provides the most viable sampling sites and surface area outside the body. However, sweat must be excreted to the outer skin surface to be analysed. Such sweat generation can be accomplished through exercise activity, thermal heating, stress or iontophoretic stimulation. Generally, sweat contains metabolites (for example, lactate, glucose, urea, ethanol or cortisol) along with electrolytes (for example, sodium, potassium, chloride or ammonium), trace elements (for example, zinc or copper) and small amounts of large molecules (for example, proteins, nucleic acids, neuropeptides or cytokines).[24] These biomarkers make in situ sweat analysis of considerable interest for non-invasive monitoring of physiological health status (for example, hydration or physical stress) and for disease diagnosis and management (for example, in such conditions as cystic fibrosis or diabetes). Non-invasive monitoring at the epidermis eliminates issues related to blood sampling maintaining the skin intact. Yet additional research is needed for determining and validating the clinical value of sweat as a diagnostic biofluid. Target sweat analytes are each transported to the sweat from surrounding capillaries with unique partitioning profiles, making reliable correlation to

concurrent blood concentrations difficult. Deeper understandings of sweat chemistry and transport, along with advances in sweat sampling and detection technologies, should accelerate sweat-based diagnostic opportunities.

Jia et al. [25] published the first demonstration, to our knowledge, of continuous monitoring of sweat lactate levels via epidermal electrochemical biosensors, providing a real-time profile of lactate sweat dynamics during exercise. Sweat lactate is a by-product of local sweat gland metabolism, and intense physical activity induces higher generation rates. Although sweat lactate does not directly reflect the concurrent blood levels, it indicates the level of physical exertion experienced during prolonged exercise and can be used as a marker for athletic efficiency without invasive blood sampling. In this study [25], the human subject was asked to wear the printed temporary tattoo biosensor, modified with lactate oxidase for measuring sweat lactate during exercise. Sweat lactate indeed increased with higher exercise intensity.

On the other hand, Sudha et al.[26] proposed a non-invasive procedure for monitoring diabetes using sweat urea as a biomarker. In fact, diabetes is a disorder that affects not only carbohydrate metabolism but also other metabolisms, including protein metabolism. The increased protein catabolism increases the production of toxic ammonia from the amino acid, the breakdown product of proteins. In the liver, this toxic ammonia is converted into non toxic urea *via* the urea cycle. This leads to an increase in blood urea and consequently the serum urea level in sweat; moreover, the hyperuremia has a strong correlation with insulin resistance. [27] Other studies dealing with urea as biotarget for sweat wearable sensor have recently appeared. [28-30]

2. Results and Discussion

The integration of optically active plasmonic materials on a flexible substrate can achieve a direct and sensitive method to analyse sweat by means of a wearable sensor, which can serve as powerful tool for non-invasive sweat monitoring. In particular, here we explore the possibility to integrate the previously developed AgNWs@PTFE substrate within a flexible and wearable chip to conduct a direct SERS detection of urea and lactic acid in sweat, which are the most concentrated organic components in this biological fluid. The as-obtained chip absorbs and filtrates molecules in solution and enables label-free molecular detection. This strategy allows to overcome the complexity related to the use of specific receptors, and, on the contrary, to provide a real fingerprint of the biological fluid offering a correlation between signal peak area of different biological targets and their relative concentration.

The first step was to test a simulated sweat sample. Sweat is a biological fluid and as such its composition is complex and variable. As mentioned in the Introduction, it contains an inorganic fraction composed of different salts and an organic fraction composed of biomolecules of different nature. Specifically, we used the following composition of simulated sweat (SS) [31]: NaCl 0.5%; K_3PO_4 0.1%; $MgSO_4$ 0.1%; 0.1% $CaCl_2$; 0.1% lactic acid; urea 0.1%. (pH = 5.4).

Reference SERS spectra of SS, urea ($0.1\%_{w/v}$) and lactic acid ($0.1\%_{w/v}$) were then collected (Figure 2) depositing 5 µL of each sample on an AgNWs@PTFE substrate as developed in Chapter 5.

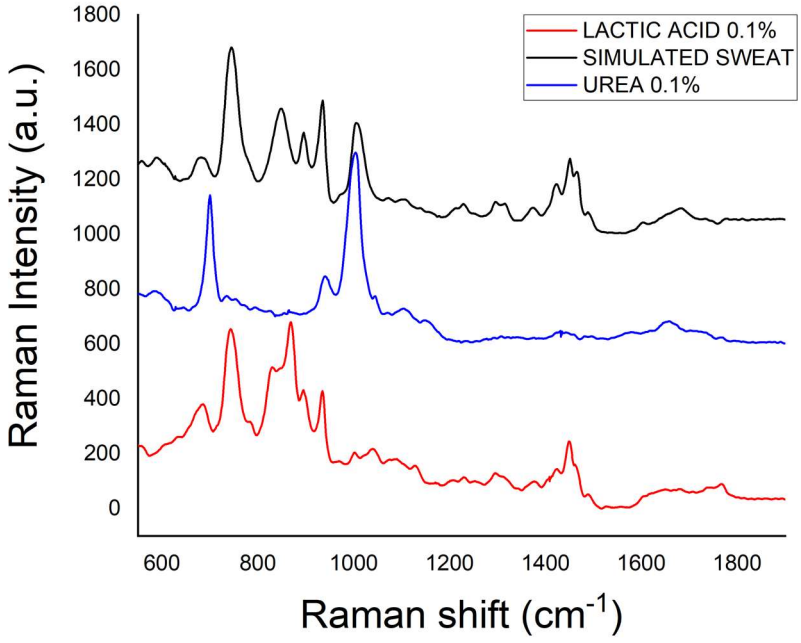

Figure 2. Reference SERS spectra of simulated sweat, lactic acid (0.1%$_{w/v}$) and urea (0.1%$_{w/v}$).

The results indicate intense SERS signals from SS and the possibility to clearly identify the main peaks of urea and lactic acid in the SS spectrum by using the SERS substrate previously developed.

The following steps involved the integration of the AgNWs substrate in a wearable SERS chip and the reproduction on a laboratory scale of the real sweating process, in order to perform a suitable calibration of the system for a reliable quantitative analysis of urea and lactic acid in sweat. For this purpose, three aspects of the sweating process can prove critical: the sweat chemistry, the sampling and the sweating flux. Urea and lactic acid are species undergoing an acid/base equilibrium in solution and that interact each other and with the ions of the solution. Concerning sweat sampling, it is important that the sweat reaches the sensitive part of the chip without being altered by substances present on the skin or in the external environment, and avoiding a direct contact between AgNWs and skin. Finally, sweating rate can vary depending on different factors both physiological (genetics, region of body) and related to external inputs (heat, training, stress).

The SERS chip consisted of three layers (Figure 3a): on the top a transpiring tape (Tegaderm), in the middle the AgNWs@PTFE substrate that was patterned with a single central spot (Ø 3 mm, as in Figure 3c), on the bottom a spacer (silicon tape) with a hole (Ø 4 mm) centered on the silver spot. This chip allows avoiding direct contact with the skin and protection from the external environment, while assures gathering of sweat metabolites on the silver spot for effective SERS detection. We then built up a simulated sweating system as schematized in Figure 3a. The system is composed of a syringe pump, which injects the sample at a constant rate of 10 µL/min [32], a transparent cell obtained by 3D printing (Clear Resin Formlabs) (Figure 3d), a microporous polyimide foil with 100 µm size pores at a density of 1 pore/mm^2 (Figure 3b) as artificial skin, and the SERS chip. The choice of using a 10 µL/min sweating flux represents an average value as found in physiological conditions.

SERS spectra of SS using the simulated sweating system were collected after 5, 10 and 15 min flux in order to identify the time required to reach the equilibrium of urea and lactic acid adsorption on

the AgNWs surface. As displayed in Figure 4, the equilibrium is reached after about 10 min. Therefore, we fixed a 10 min flux for all the following measurements.

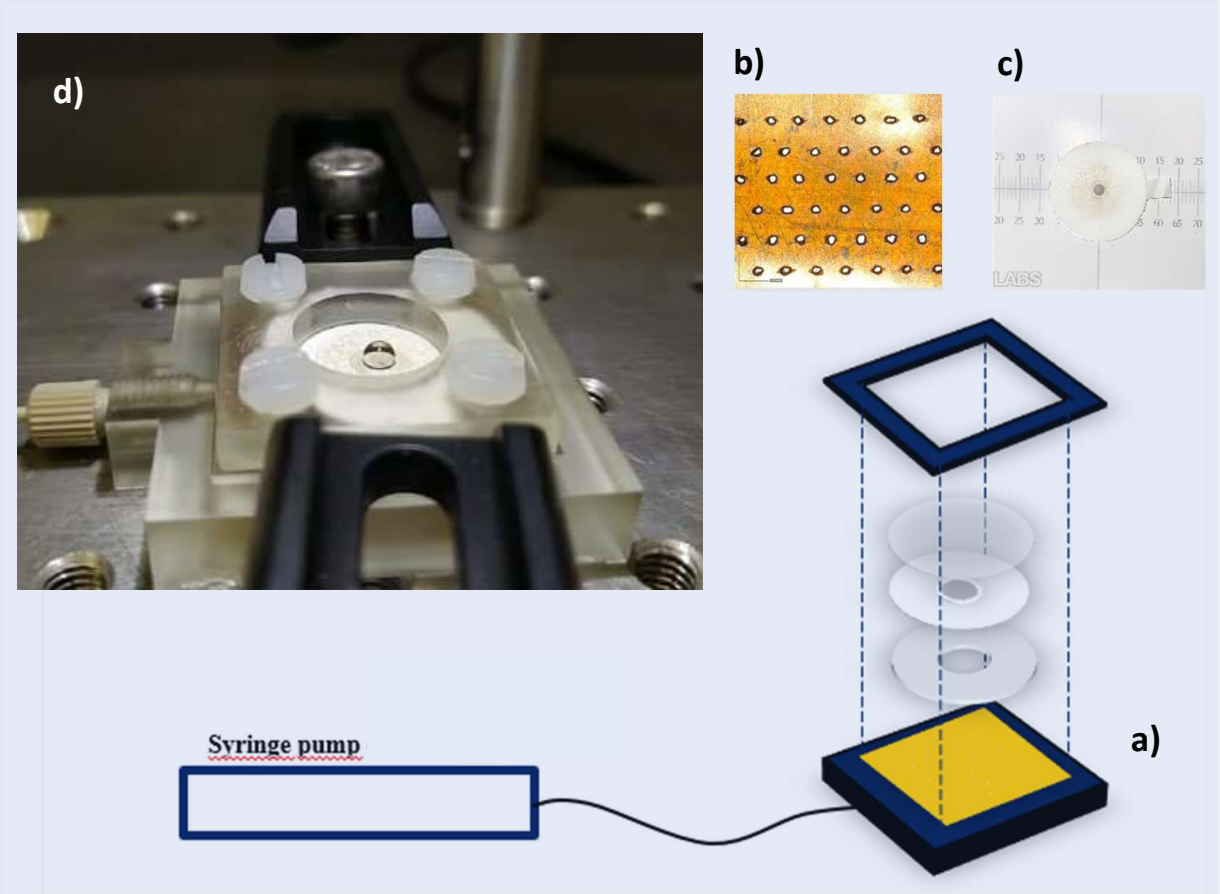

Figure 3. Simulated sweating system and SERS chip. a) Scheme of the system including the SERS chip; b) microporous polyimide; c) AgNWs@PTFE substrate used in the SERS chip and consisting of a central Ag spot of Ø 3 mm; d) cell for simulated sweating.

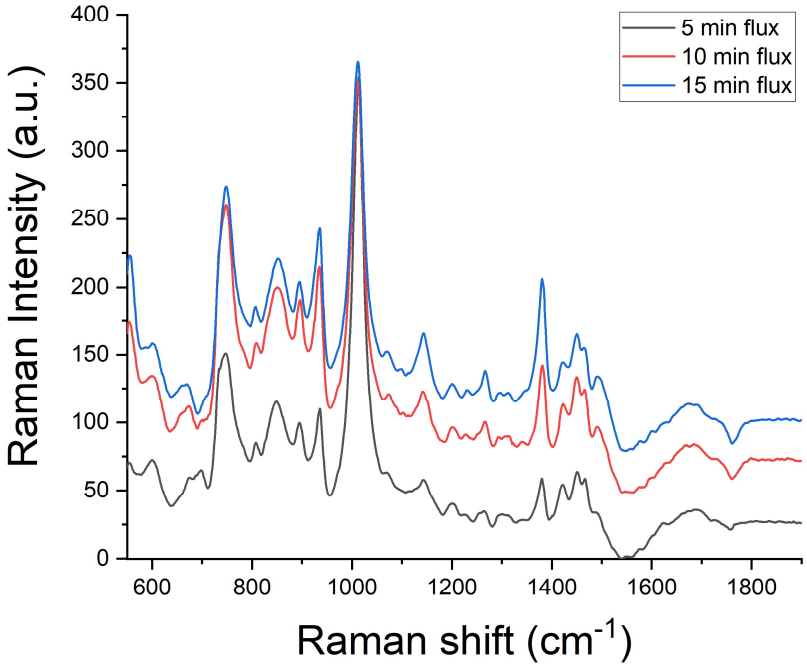

Figure 4. SERS spectra obtained by using the simulated sweating system and the SERS chip after 5,10,15 min of sweat flux.

Afterwards, the SERS spectra of SS with increasing concentration of urea (Figures 5-7) and lactic acid (Figures 8-10) were collected to establish a relationship between SERS peak area (the peaks at 1003 cm^{-1} for urea and at 712 cm^{-1} for lactic acid were selected) and related biomarkers. In this case the pH was fixed at 5.4 which represents an average between the physiological values. We may note that in the SERS spectra of SS at increasing amounts of lactic acid, the reference peak of urea also changes. This may be justified by an interaction of large amounts of lactic acid with urea, altering the chemical equilibrium of the latter and thus its SERS profile. Further experiments are needed to inspect the SERS response of SS on varying the concentration of the two biomarkers and of pH.

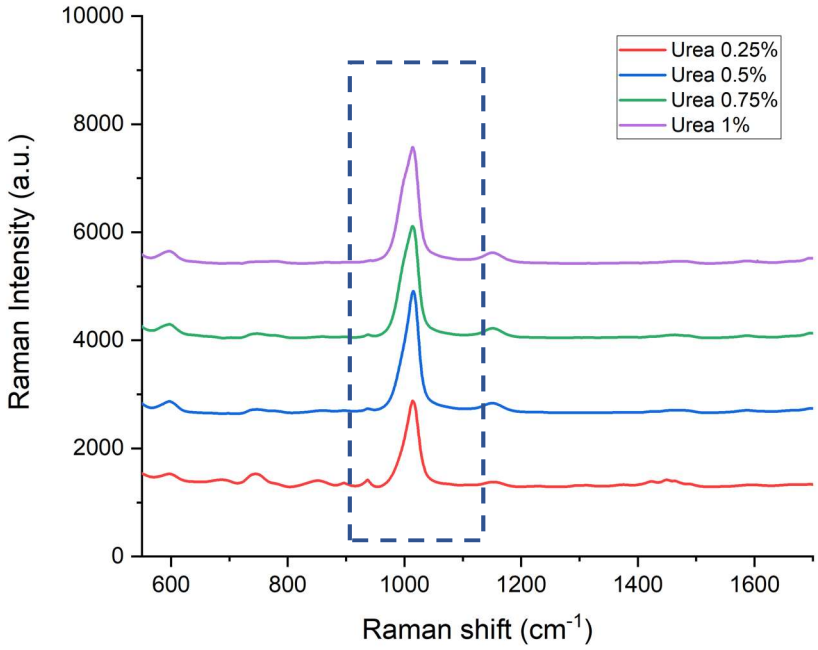

Figure 5. SERS spectra obtained by using the simulated sweating system and the SERS chip after 10 minutes of sweat flux increasing the urea concentration.

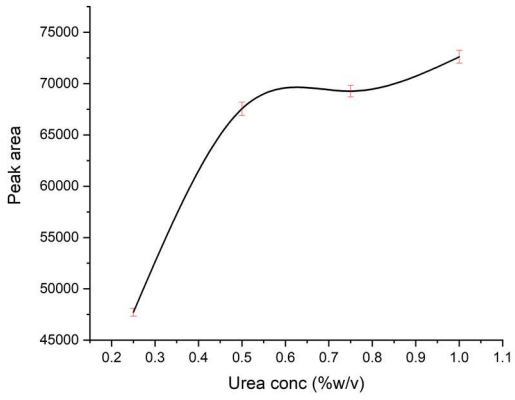

Figure 6. Calibration curve: peak area vs urea concentration.

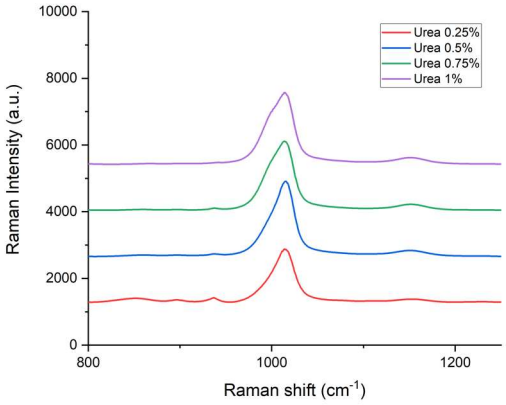

Figure 7. Magnification of SERS spectra of Figure 5.

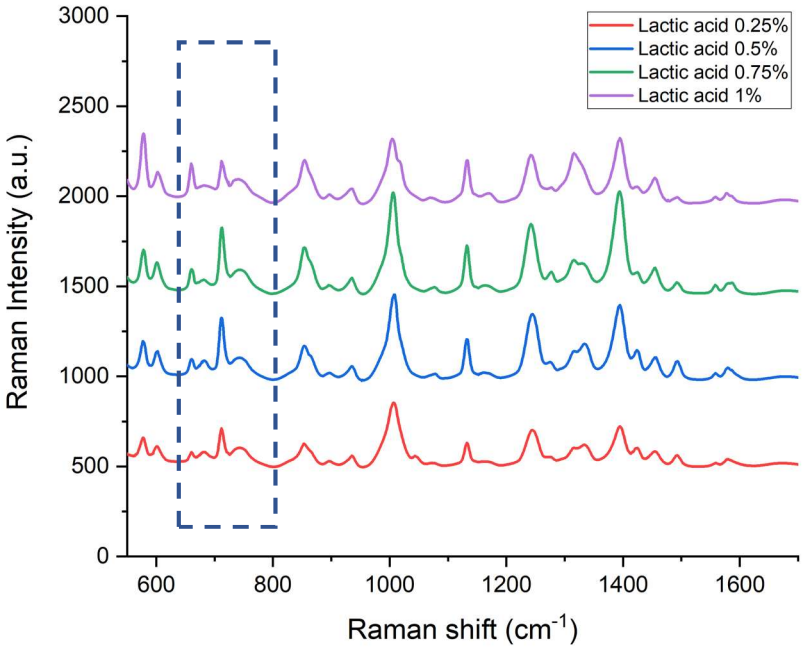

Figure 8. SERS spectra obtained by using the simulated sweating system and the SERS chip after 10 minutes of sweat flux increasing the lactic acid concentration.

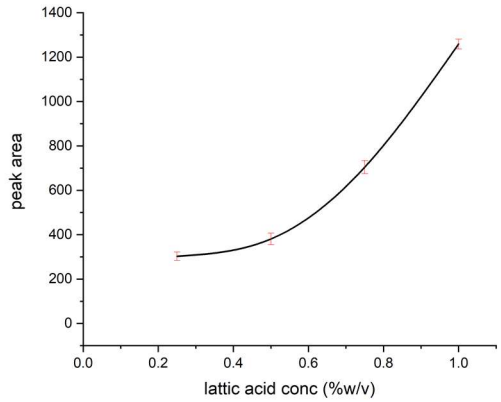

Figure 9. Calibration curve: peaks area (600-720) vs lactic acid concentration.

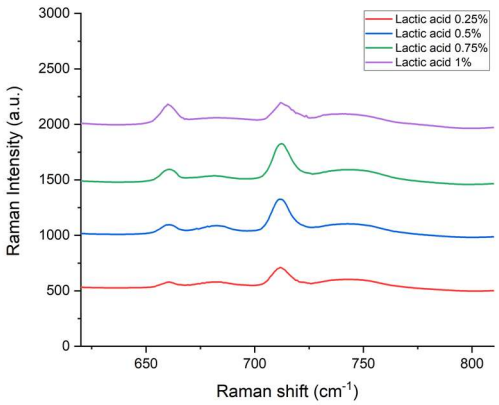

Figure 10. Magnification of SERS spectra of Figure 8.

3. Conclusions

We developed an innovative wearable AgNW@PTFE SERS chip, which was successfully tested on a simulated sweating system. We were able to obtain a calibration curve of lactic acid and urea in a range of concentrations between 0.1%$_{w/v}$ and 1%$_{w/v}$, which are of physiological interest. The whole platform can be proposed for effective monitoring of biomarkers in sweat. Further experiments will be conducted on volunteers to assess the reliability of the developed chip in an in vivo configuration.

4. Experimental Section

4.1 Materials

Urea (ChemCruz), DL Lactic acid 85% (FCC KOSHER). The inorganic salts (NaCl, K_3PO_4, $MgSO_4$, $CaCl_2$ were obtained by Sigma Aldrich.

4.2 SERS measurements

SERS spectra were obtained using AgNW@PTFE substrates containing a single silver spot (Ø 3 mm) centered on the PTFE support after 10 minutes of simulated sweating system flux at a constant injection rate of 10 μL/min. The SERS analysis was conducted on a micro-Raman spectrometer (XPlora, Horiba), working at 785 nm with 1200 grooves/mm laser power (0.598 mW), 2s integration time, and a 10x objective.

Bibliography

[1] Bandodkar, A. J., Jeerapan, I. & Wang, J. Wearable chemical sensors: present challenges and future prospects. ACS Sens. 1, 464–482 (2016).

[2] Heikenfeld, J. et al. Wearable sensors: modalities, challenges, and prospects. Lab Chip 18, 217–248 (2018).

[3] Matzeu, G., Florea, L. & Diamond, D. Advances in wearable chemical sensor design for monitoring biological fuids. Sens. Actuators B Chem. 211, 403–418 (2015).

[4]. Liu, Y., Pharr, M. & Salvatore, G. A. Lab-on-skin: a review of fexible and stretchable electronics for wearable health monitoring. ACS Nano 11, 9614–9635 (2017).

[5] Amjadi, M., Kyung, K. U., Park, I. & Sitti, M. Stretchable, skin-mountable, and wearable strain sensors and their potential applications: a review. Adv. Funct. Mater. 26, 1678–1698 (2016).

[6] Bariya, M., Nyein, H. Y. Y. & Javey, A. Wearable sweat sensors. Nat. Electron. 1, 160–171 (2018).

[7] Yang, Y.; Gao, W. Wearable and Flexible Electronics for Continuous Molecular Monitoring. Chem. Soc. Rev. 2019, 48, 1465− 1491.

[8] Jin, H.; Abu-Raya, Y. S.; Haick, H. Advanced Materials for Health Monitoring with Skin-Based Wearable Devices. Adv. Healthcare Mater. 2017, 6, 1700024.

[9] Emaminejad, S.; Gao, W.; Wu, E.; Davies, Z. A.; Nyein, H. Y. Y.; Challa, S.; Ryan, S. P.; Fahad, H. M.; Chen, K.; Shahpar, Z.; Talebi, S.; Milla, C.; Javey, A.; Davis, R. W. Autonomous Sweat Extraction and Analysis Applied to Cystic Fibrosis and Glucose Monitoring Using a Fully Integrated Wearable Platform. Proc. Natl. Acad. Sci. U. S. A. 2017, 114, 4625−4630.

[10] Zhang, L.; Pan, J.; Zhang, Z.; Wu, H.; Yao, N.; Cai, D.; Xu, Y.; Zhang, J.; Sun, G.; Wang, L.; Geng, W.; Jin, W.; Fang, W.; Di, D.; Tong, L. Ultrasensitive skin-like wearable optical sensors based on glass micro/nanofibers. Opto-Electron. Adv. 2020, 3, 190022.

[11] Kim, J.; Campbell, A. S.; de Á vila, B. E.-F.; Wang, J. Wearable Biosensors for Healthcare Monitoring. Nat. Biotechnol. 2019, 37, 389−406.

[12] Koh, A. et al. A sof, wearable microfuidic device for the capture, storage, and colorimetric sensing of sweat. Sci. Transl. Med. 8, 366ra165 (2016).

[13] Gao, W. et al. Fully integrated wearable sensor arrays for multiplexed in situ perspiration analysis. Nature 529, 509–514 (2016).

[14] Lee, H. et al. A graphene-based electrochemical device with thermoresponsive microneedles for diabetes monitoring and therapy. Nat. Nanotechnol. 11, 566–572 (2016).

[15] Jeerapan, I., Sempionatto, J. R., Pavinatto, A., You, J. M. & Wang, J. Stretchable biofuel cells as wearable textile-based self-powered sensors. J. Mater. Chem. A Mater. Energy Sustain. 4, 18342–18353 (2016).

[16] Bandodkar, A. J., Jia, W. Z. & Wang, J. Tattoo-based wearable electrochemical devices: a review. Electroanalysis 27, 562–572 (2015).

[17] Xue, X. Y. et al. Self-powered electronic-skin for detecting glucose level in body fuid basing on piezo-enzymatic-reaction coupling process. Nano Energy 26, 148–156 (2016).

[18] Han, W. et al. A self-powered wearable noninvasive electronic-skin for perspiration analysis based on piezo-biosensing unit matrix of enzyme/ZnO nanoarrays. ACS Appl. Mater. Interfaces 9, 29526–29537 (2017).

[19] Morris, D. et al. Bio-sensing textile based patch with integrated optical detection system for sweat monitoring. Sens. Actuators B Chem. 139, 231–236 (2009).

[20] Jia, W. et al. Electrochemical tattoo biosensors for real-time noninvasive lactate monitoring in human perspiration. Anal. Chem. 85, 6553–6560 (2013). 59. Gualandi, I. et al. Textile organic electrochemical transistors as a platform for wearable biosensors. Sci. Rep. 6, 33637 (2016).

[21] Caldara, M., Colleoni, C., Guido, E., Re, V. & Rosace, G. Optical monitoring of sweat pH by a textile fabric wearable sensor based on covalently bonded litmus-3-glycidoxypropyltrimethoxysilane coating. Sens. Actuators B Chem. 222, 213–220 (2016).

[22] Choi, D. H., Kim, J. S., Cutting, G. R. & Searson, P. C. Wearable potentiometric chloride sweat sensor: the critical role of the salt bridge. Anal. Chem. 88, 12241–12247 (2016).

[23] Liu, J., Liu, R. & Xu, K. Accuracy of noninvasive glucose sensing based on near-infrared spectroscopy. Appl. Spectrosc. 69, 1313–1318 (2015). 63. Ben Mohammadi, L. et al. In vivo evaluation of a chip based near infrared sensor for continuous glucose monitoring. Biosens. Bioelectron. 53, 99–104 (2014).

[24] Sonner, Z. et al. Te microfuidics of the eccrine sweat gland, including biomarker partitioning, transport, and biosensing implications. Biomicrofuidics 9, 031301 (2015).

[25] Jia, W. et al. Electrochemical tattoo biosensors for real-time noninvasive lactate monitoring in human perspiration. Anal. Chem. 85, 6553–6560 (2013).

[26] Sudha S.,Kalpana R.,Soundararajan P. Quantification of sweat urea in diabetes using electro-optical technique. Physiol. Meas. 42 (2021) 095002

[27] Whaley-Connell A. and Sowers J. R. 2017 Insulin resistance in kidney disease: is there a distinct role separate from that of diabetes or obesity? Cardiorenal Med. 8 41–9

[28] Saddam Hussain and Soo-young Park. Sweat-Based Noninvasive Skin-Patchable Urea Biosensors with Photonic Interpenetrating Polymer Network Films Integrated into PDMS Chips. ACS Sens. 2020, 5, 3988−3998

[29] Yingli W., Chen Z., Jingjing W., Xuan L., Wearable plasmonic-metasurface sensor for noninvasive and universal molecular fingerprint detection on biointerfaces. Sci. Adv. 2021; 7 eabe4553

[30] Y. Zhang, H. Guo, S. B. Kim, Y. Wu, Passive sweat collection and colorimetric analysis of biomarkers relevant to kidney disorders using a soft microfluidic system. Lab Chip, 2019, 19, 1545

[31] E. H. Koh, W. C. Lee, Y.J. Choi. A Wearable Surface-Enhanced Raman Scattering Sensor for LabelFree Molecular Detection ACS Appl. Mater. Interfaces 2021, 13, 3024−3032

[32] A. Brueck, K. Bates, T. Wood, W. House, Z. Martinez, An Artificial Sweating System for Sweat Sensor Testing Applications. Electronics 2019, 8, 606.

Conclusions

Silver nanowires (AgNWs) are among the most powerful and versatile materials in the nanotechnology area and were here selected for the development of an effective optical platform based on SERS technique. This thesis ranges from the optimization of the synthesis of AgNWs to their engineering in an ideal SERS substrate, aimed at promoting this technique for its routine use in real applications.

The optimized synthesis of AgNWs provided us well-monodispersed nanostructures with minimal amounts of by-products. Then two SERS substrates based on AgNWs were developed by cost-effective, simple and reproducible strategies. The substrates were fabricated using different techniques, supporting materials and AgNWs dimensions. Anyway, the final results satisfy the criteria of an effective SERS-active layer of assembled AgNWs, which are randomly distributed creating a dense network with a considerable number of SERS hotspots. The first substrate (AgNWs@PTFE) was obtained by a simple flow-through method consisting in filtering a suspension of AgNWs through a microporous PTFE membrane. Afterwards, laser ablation is exploited to operate a precise substrate patterning in the form of regular SERS-active spots producing intense local E-fields that are at the basis of effective SERS signals. In the second substrate (AgNWs@G-paper) the preparation of 2D plasmonic substrates was performed by spraying an AgNWs dispersion on 50-µm thick graphene-based paper as achieved by mechanical compression of small stacks of graphene and interposing a temporary mask to obtain regular SERS-active spots as above. SERS substrates proposed so far are often unsuitable for the practical detection of biomolecules due to the lack of the simultaneous presence of preferred features, such as low manufacturing costs, disposable characteristics, and simplicity for routine application in turn limiting their use at or near point-of-need settings. The SERS substrates we developed represent an attempt in progressing SERS toward commercially viable sensing solutions including diagnostics at the point-of-care and on-site analyses. According to this point of view we have then explored the possibility to use AgNWs substrates in two exemplary SERS applications. In the first study we were aimed at identifying different flavonoid species in plant extracts. Specifically, we were able to obtain an intense SERS profile from chamomile extracts and successfully inspected it for the presence of the main flavonoids. The method can be proposed for quasi real-time analysis of plant extracts by the use of portable or benchtop Raman spectrometers, making it easier to monitor beneficial flavonoids in plants for the nutraceutical industry. In the second study the AgNWs substrate was integrated into a skin-wearable SERS chip to track the amount of specific metabolites in sweat. In this case, the perspective is the realization of a wearable system that can be interrogated by a portable Raman device for monitoring of chronic diseases or altered health states.

Author's publications

1. Martina Banchelli, Chiara Amicucci, Emmanuel Ruggiero, Cristiano D'Andrea, Maximilien Cottat, Daniele Ciofini, Iacopo Osticioli, Giacomo Ghini, Salvatore Siano, Roberto Pini, Marella de Angelis, and Paolo Matteini. *Spot-on SERS Detection of Biomolecules with Laser-Patterned Dot Arrays of Assembled Silver Nanowires*. ChemNanoMat 2019, 5, 1-9.

2. Andrea Barucci, Cristiano D'Andrea, Edoardo Farnesi, Martina Banchelli, Chiara Amicucci, Marella de Angelis, Byungil Hwang and Paolo Matteini. *Label-free SERS detection of proteins based on machine learning classification of chemostructural determinants*. The Analyst 2021, 146(2)

3. Chiara Amicucci, Cristiano D'Andrea, Marella de Angelis, Martina Banchelli, Roberto Pini and Paolo Matteini. *Cost Effective Silver Nanowire-Decorated Graphene Paper for Drop-On SERS Biodetection.* Nanomaterials 2021, 11, 1495

4. Chiara Amicucci, Cristiano D'Andrea, Marella de Angelis, Martina Banchelli, Roberto Pini and Paolo Matteini. *SERS detection of flavonoids in plant extracts.* (submitted)

5. Chiara Amicucci, Cristiano D'Andrea, Marella de Angelis, Martina Banchelli, Roberto Pini and Paolo Matteini. *Development of a wearable SERS chip for detection of lactic acid and urea in sweat.* (submitted)